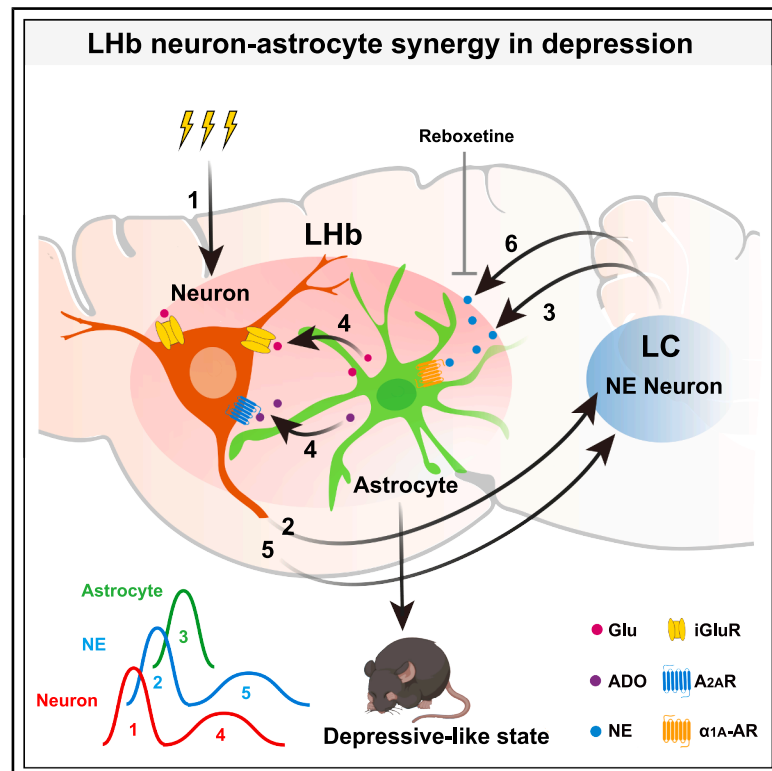


Neuron-astrocyte coupling in lateral habenula mediates depressive-like behaviors

Graphical abstract



Authors

Qianqian Xin, Junying Wang, Jinkun Zheng, ..., Xiao-Ming Li, Huan Ma, Hailan Hu (胡海岚)

Correspondence

huhailan@zju.edu.cn

In brief

Stress-induced depression-like behaviors are driven by a dynamic recurrent network involving neurons and astrocytes in the lateral habenula and norepinephrine release from neurons in the locus coeruleus in freely moving mice.

Highlights

- Stress induces rapid astrocytic calcium and biphasic neuronal response in LHb
- LHb-neuron-induced phasic NE release from LC activates LHb astrocytes
- LHb astrocyte activation drives second-phase LHb neuronal response and NE release
- NET inhibitors block phasic NE and LHb-astrocytic calcium, preventing depression

Article

Neuron-astrocyte coupling in lateral habenula mediates depressive-like behaviors

Qianqian Xin,^{1,2,5} Junying Wang,^{1,2,5} Jinkun Zheng,² Yi Tan,^{1,2,3} Xiaoning Jia,² Zheyi Ni,² Zijie Xu,² Jiesi Feng,⁴ Zhaofa Wu,⁴ Yulong Li,⁴ Xiao-Ming Li,² Huan Ma,² and Hailan Hu (胡海岚)^{1,2,3,6,*}

¹Department of Neurobiology, Affiliated Mental Health Center & Hangzhou Seventh People's Hospital, Zhejiang University School of Medicine, Hangzhou 310058, China

²Nanhu Brain-Computer Interface Institute, Liangzhu Laboratory, MOE Frontier Science Center for Brain Science and Brain-Machine Integration, State Key Laboratory of Brain-Machine Intelligence, New Cornerstone Science Laboratory, Zhejiang University, Hangzhou 311121, China

³Department of Psychiatry and International Institutes of Medicine, The Fourth Affiliated Hospital, Zhejiang University School of Medicine, Yiwu 322000, China

⁴State Key Laboratory of Membrane Biology, Peking University School of Life Sciences, Beijing 100871, China

⁵These authors contributed equally

⁶Lead contact

*Correspondence: huhailan@zju.edu.cn

<https://doi.org/10.1016/j.cell.2025.04.010>

SUMMARY

The lateral habenula (LHb) neurons and astrocytes have been strongly implicated in depression etiology, but it was not clear how the two dynamically interact during depression onset. Here, using multi-brain-region calcium photometry recording in freely moving mice, we discover that stress induces a most rapid astrocytic calcium rise and a bimodal neuronal response in the LHb. LHb astrocytic calcium requires the α_{1A} -adrenergic receptor and depends on a recurrent neural network between the LHb and locus coeruleus (LC). Through the gliotransmitter glutamate and ATP/adenosine, LHb astrocytes mediate the second-wave LHb neuronal activation and norepinephrine (NE) release. Activation or inhibition of LHb astrocytic calcium signaling facilitates or prevents stress-induced depressive-like behaviors, respectively. These results identify a stress-induced positive feedback loop in the LHb-LC axis, with astrocytes being a critical signaling relay. The identification of this prominent neuron-glia interaction may shed light on stress management and depression prevention.

INTRODUCTION

Stress is a major risk factor for depression.¹ Modern theories on the etiology of major depressive disorder (MDD) propose that stress alters molecular expression, cellular activities, and synaptic connections in specific brain regions.^{2,3} The lateral habenula (LHb), known as the brain's "anti-reward center," plays a critical role in depression pathophysiology.⁴⁻⁶ The LHb regulates essentially all neuromodulatory systems, including serotonin, dopamine, and norepinephrine (NE).⁶⁻⁸ LHb neurons are activated by stress⁹⁻¹² and exhibit hyperactivity in depressive states.¹³⁻¹⁸ Although neuronal dysfunction has long dominated depression research, emerging evidence highlights malfunctions of LHb astrocytes, such as upregulated Kir4.1 for potassium buffering¹⁹ and downregulated glutamate transporter1 (GLT1) for glutamate uptake.^{20,21} However, it has remained elusive how neurons and astrocytes in the LHb coordinate their activity in response to stress and how their dynamic interaction contributes to depression etiology.

The synergy between neurons and astrocytes is increasingly recognized as crucial in brain physiology, animal behavior, and

disease.²²⁻²⁸ Astrocytes communicate bidirectionally with neurons via chemical signaling.²⁹⁻³¹ They possess dense, fine processes and express various types of G-protein-coupled receptors (GPCRs), enabling them to sense neuronal and synaptic activities through calcium transients.³²⁻³⁶ Astrocytic calcium levels can be elevated by neuromodulators, such as acetylcholine (ACh),³⁷⁻⁴⁰ dopamine,^{33,41} serotonin,⁴² or NE.⁴³⁻⁴⁶ In turn, astrocytes can regulate neuronal functions at diverse timescales through the uptake of extracellular ions and neurotransmitters^{19,47-49} or the release of gliotransmitters.^{24,29,50-55} Gliotransmitters, including glutamate, gamma-aminobutyric acid (GABA), D-serine, and ATP/adenosine, can synchronize neuronal excitation,^{56,57} enhance firing fidelity,⁵⁸ or fine-tune synaptic transmission.^{33,41,59-63} Despite their integral roles, neuron-astrocyte signaling dynamics in stress and depression remain poorly understood.

In this study, we used fiber photometry in freely moving mice to measure calcium activity of neurons and astrocytes in response to stress in multiple brain regions. Stress triggered the fastest astrocytic calcium rise and a biphasic neuronal response in the LHb. Using cell-type-specific manipulations

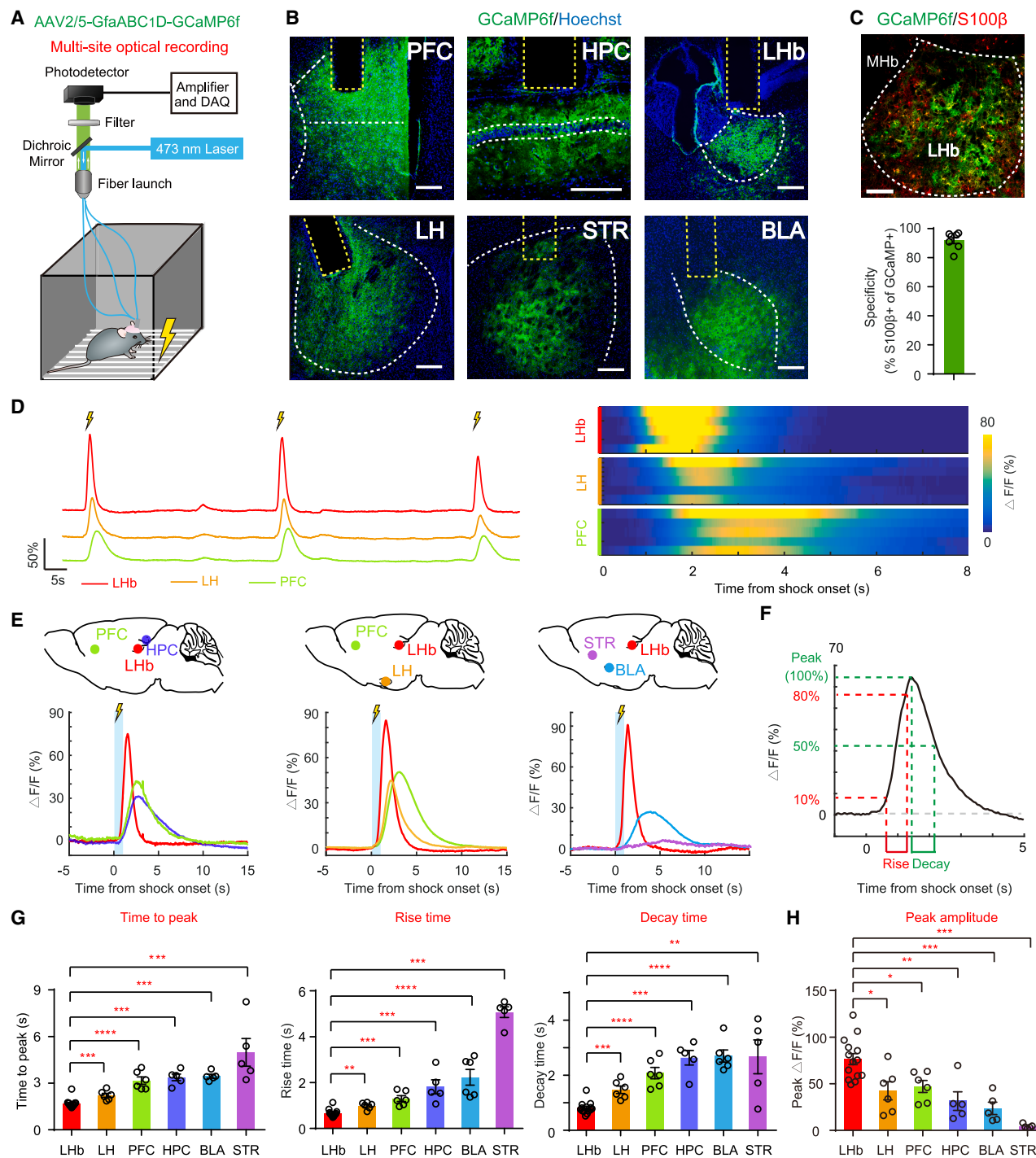


Figure 1. FS induces the fastest calcium rise in LHb astrocytes

(A) Schematic illustrating viral construct for astrocyte-specific GCaMP expression and multi-site fiber photometry setup for recording calcium activities during FS. (B) Illustration of viral expression (GFP and Hoechst staining) and optic fiber placement (yellow dotted line) in 6 central nervous system (CNS) regions (white dotted outline). Green, GCaMP6f; blue, Hoechst. Scale bar, 200 μ m.

(C) GCaMP expression is highly specific in astrocytes. Top: representative LHb image stained with GFP (GCaMP positive cells, green) and S100 β (astrocytic marker, red). Scale bar, 100 μ m. Bottom: percentage of GCaMP-positive cells co-labeled with S100 β ($n = 7$ slices, 3 mice).

(D) Representative traces (left) and heatmap (right) of delta/F ratio of simultaneously recorded astrocytic calcium signals in LHb, LH, and PFC over three continuous FSs.

(E) FS-onset-aligned calcium signal changes in multi-region astrocytes.

(legend continued on next page)

combined with fiber photometry and two-photon imaging, we identified bidirectional neuron-astrocyte interactions in the LHb-locus coeruleus (LC) circuit during stress response and pinpointed a critical role of LHb astrocytes in the onset of depression.

RESULTS

Foot-shock stress induces the fastest calcium rise in LHb astrocytes

We performed *in vivo* multi-site fiber photometry to record astrocytic calcium activities during foot-shock stress (FS; duration: 1 s; intensity: 1 mA; [Figure 1A](#)). We recorded six representative stress-responsive regions, including medial prefrontal cortex (mPFC), hippocampus (HPC), lateral habenula (LHb), lateral hypothalamus (LH), striatum (STR), and basolateral amygdala (BLA). Adeno-associated virus (AAV) 2/5 expression of the glia-specific GfaABC1D promoter,⁶⁴ driving the genetically encoded calcium indicator, GCaMP6f,⁶⁵ allowed the recording of calcium signals specifically in astrocytes ([Figure 1B](#)). Among the GCaMP6f-positive cells, 91.9% were S100 β (astrocytic marker) positive and 0.3% were NeuN (neuronal marker) positive ([Figures 1C and S1A](#)), suggesting a highly specific expression. Three brain regions were simultaneously recorded per animal, and their calcium responses were aligned to the onset of FS to allow the comparison of signals across different brain regions ([Figures 1D and 1E](#)). Although all six recorded regions showed increased astrocytic calcium activities in response to FS ([Figures 1E and S1C](#)), signals in the LHb peaked significantly earlier than those of the other five regions (mean latency to peak 1.68 ± 0.08 s in LHb, 2.22 ± 0.12 s in LH, 3.17 ± 0.24 s in PFC, 3.37 ± 0.22 s in HPC, 3.45 ± 0.13 s in BLA, 4.98 ± 0.89 s in STR; [Figures 1D–1G](#)). The peak amplitude of FS-evoked LHb astrocytic calcium signals was also larger than those of the other five regions ([Figure 1H](#)). By analyzing the kinetics of calcium signals in mice with varying levels of peak fluorescence in the LHb, we found that the time to peak did not depend on the peak amplitude ([Figure S1B](#)), suggesting that the kinetics of calcium signals is not affected by signal intensity but rather reflects intrinsic regional properties. Thus, among the multiple regions examined, the LHb astrocytes showed the most rapid calcium response to FS, suggesting that it may play an important role in processing stress-related information.

FS induces biphasic calcium activities in LHb neurons

We next expressed GCaMP6s under the CaMKII α promoter in the above six brain regions and performed calcium photometry recording in neurons ([Figures 2A and S2](#)). Consistent with previous reports that LHb neurons encode aversive signals,^{9,11} LHb neuronal calcium signals were strongly activated in response to FS stress ([Figures 2B, 2C, S3A, and S3B](#)). Interestingly, the FS-evoked calcium signals in LHb neurons first peaked at

0.9 ± 0.03 s ([Figure 2D](#)) and were followed by a second phase of activation with the inflection point at 2.54 ± 0.16 s ([Figures 2C, 2D, and S3C](#)). Although the second-phase signal had a smaller peak due to its prolonged decay time, its area under the curve (AUC) is 3.46 ± 0.78 -fold of that of the first phase ([Figures 2D, S3D, and S3E](#)), suggesting that even more calcium entered during the second phase. Such FS-evoked bimodal neuronal calcium activation was not observed in the other five brain regions examined ([Figure S2](#)).

To better understand the relationship between stress-activated neuronal and astrocytic calcium activities in the LHb, we simultaneously recorded their activities by expressing the red calcium sensor jRGECO1a⁶⁶ under the neuron-specific human synapsin (hSyn) promoter and green GCaMP6f under the GfaABC1D promoter ([Figure 2E](#)). Consistent with results from their separate recordings in [Figures 1D–1H and 2A–2D](#), dual-color fiber photometry recording revealed that FS triggered sequential activation of LHb neurons and astrocytes, with the neuronal signals peaking at 0.64 ± 0.04 s and astrocytic signals peaking at 1.64 ± 0.05 s ([Figures 2F–2H](#)). It is also of interest to note that LHb astrocytic signals peaked between the first and second phase of LHb neuronal signals ([Figures 2F–2H](#)), suggesting a possibility that LHb astrocytes may be regulated by first-phase neuronal activation and contribute to second-phase neuronal activity.

Neuron-to-astrocyte crosstalk in the LHb during FS

In order to characterize the mechanism of LHb neuron-astrocyte interaction in stress processing, we first explored the potential crosstalk from neurons to astrocytes ([Figure 3](#)). We used AAV virus to express ChrimsonR in LHb neurons and GCaMP6f in LHb astrocytes. Subsequently, we recorded calcium activities in astrocytes following photostimulation of LHb neurons both *in vivo* and *in vitro* ([Figures 3A and 3D](#)). For the *in vivo* experiments, we tracked LHb astrocytic calcium activities using fiber photometry while optogenetically activating LHb neurons in freely moving mice ([Figure 3A](#)). For the *in vitro* experiments, we monitored LHb astrocytic calcium activities using two-photon imaging while optogenetically activating the LHb neurons in brain slices ([Figure 3D](#)). Surprisingly, although activation of LHb neurons robustly activated LHb astrocytic calcium signals in a frequency-dependent manner *in vivo* ([Figures 3B and 3C](#)), it failed to do so *in vitro* ([Figures 3E and 3F](#)). Even under stimulation frequency as high as 70 Hz, still no evoked astrocytic calcium signal was detected in brain slices ([Figure 3F](#)). We also coexpressed ChrimsonR and GCaMP6s in LHb neurons and found that the same optogenetic stimulation protocol was able to strongly activate LHb neurons in brain slices ([Figures S4A–S4D](#)). These results suggest that, first, activation of LHb neurons can lead to activation of LHb astrocytes *in vivo* and, second, the lack of neuron-activated astrocytic calcium signals *in vitro* was not due to inefficient activation of LHb neurons but more likely a lack of mediator of the neuron-to-astrocyte crosstalk in the brain slice setup.

(F) Illustration of calculation of rise and decay time.

(G) Average time to peak (left), rise time (middle), and decay time (right) of FS-evoked astrocytic calcium signals in six regions. Each circle represents one mouse.

(H) Average peak amplitudes of FS-evoked astrocytic calcium signals in six regions. Each circle represents one mouse.

* $p < 0.05$; ** $p < 0.01$; *** $p < 0.001$; **** $p < 0.0001$; n.s., not significant. Data are represented as mean \pm SEM.

See also [Figure S1](#).

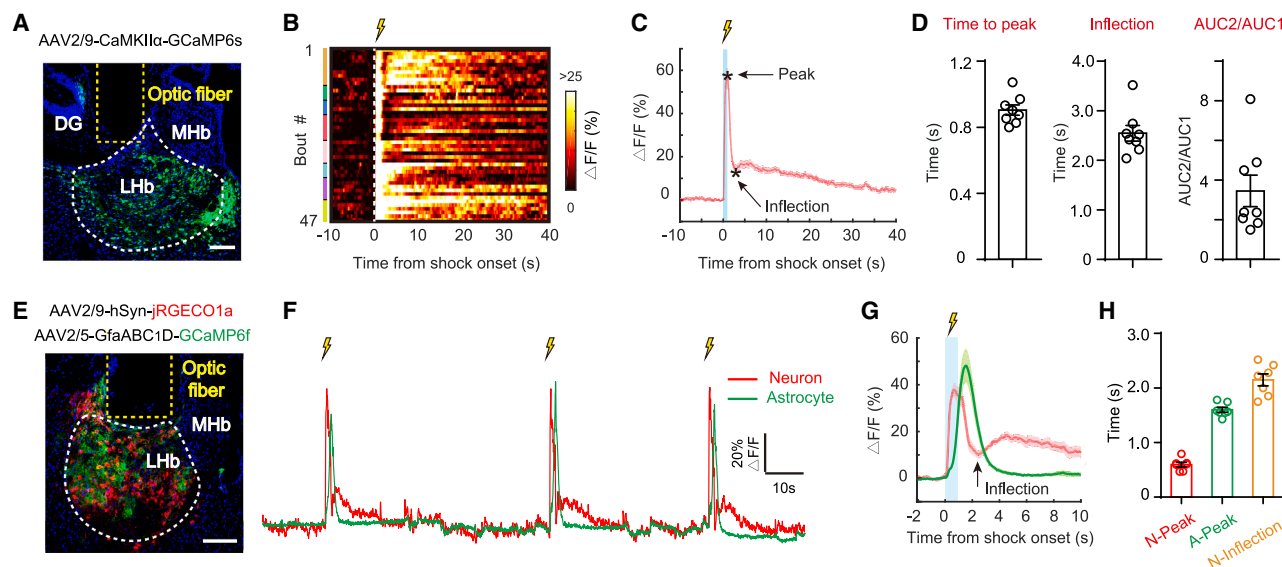


Figure 2. FS induces biphasic calcium activities in LHB neurons

(A) Illustration of viral construct for neuron-specific GCaMP expression, viral expression, and optic fiber placement (yellow dotted line) in LHB, the boundary of which is outlined by the white dotted line. Green, GCaMP6s; blue, Hoechst. Scale bar, 100 μ m.
 (B) Heatmap of deltaF/F ratio of calcium signals from LHB neurons ($n = 47$ trials, 8 mice), aligned to FS onset. Color bars on the left indicate different mice.
 (C) Average deltaF/F ratio of calcium signals from LHB neurons aligned to FS onset. Solid lines indicate mean and shaded areas indicate SEM.
 (D) Average time to peak (left), average time to inflection (middle) of LHB neuronal calcium signals from FS onset, and ratio of area under curve (AUC) of FS-evoked signals after vs. before the inflection point (right). AUC1, AUC from FS onset to inflection; AUC2, AUC from inflection to 10% peak. Each circle represents one mouse.
 (E) Illustration of dual-color expression-neuronal jRGECO1a and astrocytic GCaMP6f with optic fiber placement (yellow dotted line) in LHB. Scale bar, 100 μ m.
 (F) Representative traces of simultaneously recorded neuronal and astrocytic calcium signals in LHB over three continuous FSs.
 (G) DeltaF/F ratio of calcium signals from LHB neurons and LHB astrocytes aligned to FS onset. Solid lines indicate mean and shaded areas indicate SEM.
 (H) Average time to peak of LHB neuronal (N-peak, left) and astrocytic (A-peak, middle) calcium signals and average time to inflection of LHB neuronal calcium signals (N-inflection, right) from FS onset using dual-color fiber photometry system. Each circle represents one mouse.
 See also [Figures S2](#) and [S3](#).

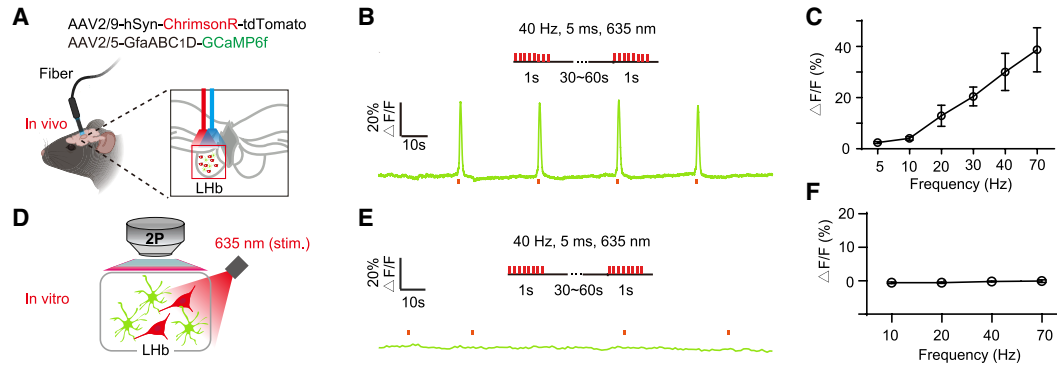
To search for the mediator of the neuron-astrocyte crosstalk in the LHB, we first looked for the astrocytic receptor(s) involved in this process *in vivo*. We measured astrocytic calcium photometry signals in response to FS while intraperitoneally (i.p.) injecting animals with blood-brain-barrier (BBB)-permeable inhibitors or antagonists of receptors for different neurotransmitters or neuromodulators ([Figure 3G](#)). We tested receptors for three classes of neurotransmitter/modulators, which were previously implicated in astrocytic Ca^{2+} signaling: the metabotropic glutamate receptors (mGluR),^{32,67} ACh receptors (AChRs),^{37,40,68} and NE receptors (NER).^{44,45,69,70} Although antagonists for mGluR5, mGluR2/3, muscarinic AChR (mAChR), or ionotropic AChR (nAChR), namely MPEP, LY341495, scopolamine, and mecamylamine, respectively, induced no change, antagonists for the NERs caused strong impacts on FS-evoked LHB astrocytic Ca^{2+} ([Figures 3H](#) and [S5](#)). In particular, the α 1-adrenergic receptors (α 1-ARs) antagonist prazosin largely suppressed FS-evoked LHB astrocytic calcium signals ([Figures 3H](#) and [S5A](#)). On the other hand, atipamezole, the antagonist of α 2-ARs, which are mostly expressed on presynaptic terminals serving an autoinhibitory function,⁷¹ increased FS-evoked LHB astrocytic calcium signals ([Figures 3H](#) and [S5B](#)), possibly due to the release of autoinhibition. Among the α 1-ARs, there are three subtypes: α 1A-AR, α 1B-AR, and α 1D-AR. By using their respective antago-

nists, we further delineated the primary contributor of FS-evoked LHB astrocytic calcium signals to be the α 1A-AR ([Figure 3I](#)).

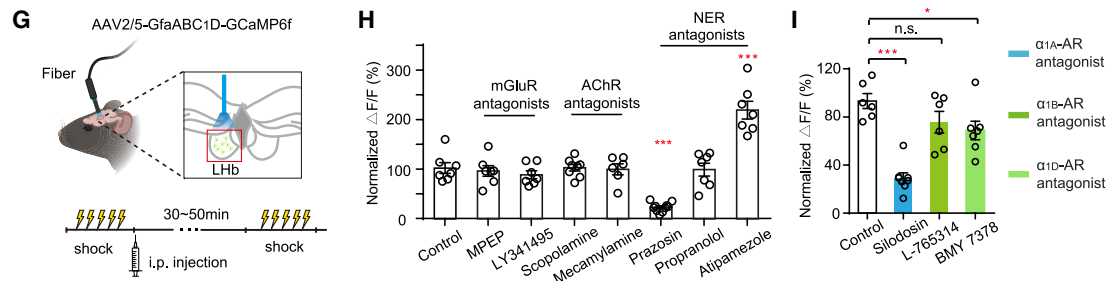
To further confirm that NE can activate LHB astrocytes through the α 1-AR, we performed calcium imaging of astrocytes on LHB brain slices ([Figure S6](#)). Bath application of either NE or the α 1-AR agonist phenylephrine (PE) increased astrocytic calcium signals in the presence of tetrodotoxin (TTX, which blocks all neuronal action potentials) ([Figures S6A–S6E](#)), which were blocked by the α 1-AR antagonist prazosin ([Figures S6F](#) and [S6G](#)).

To detect whether NE is indeed released during FS in the LHB, we virally expressed in the LHB genetically encoded G-protein-coupled receptor activation-based NE (GRAB_{NE}) sensor, NE2h⁷² ([Figure 3J](#)). Interestingly, in response to FS, NE signals exhibited both rapid phasic activity and slower ramping activity ([Figures 3K](#) and [S7A–S7C](#)). The rapid phasic increases in NE signals were time-locked to the delivery of FS and, similar as LHB neuronal Ca^{2+} signals, displayed bimodal distribution ([Figures 3K](#) and [3L](#)). Over the course of 6 FSs, the LHB-NE signals kept ramping up and remained elevated for the duration of the 8-min session in the shock chamber ([Figures 3K](#), [S7A](#), and [S7C](#)). Alignment of LHB-neuron calcium, LHB-NE sensor, and LHB-astrocyte calcium signals to the FS onset revealed a sequential activation of these three signals ([Figures 3M](#) and [3N](#)).

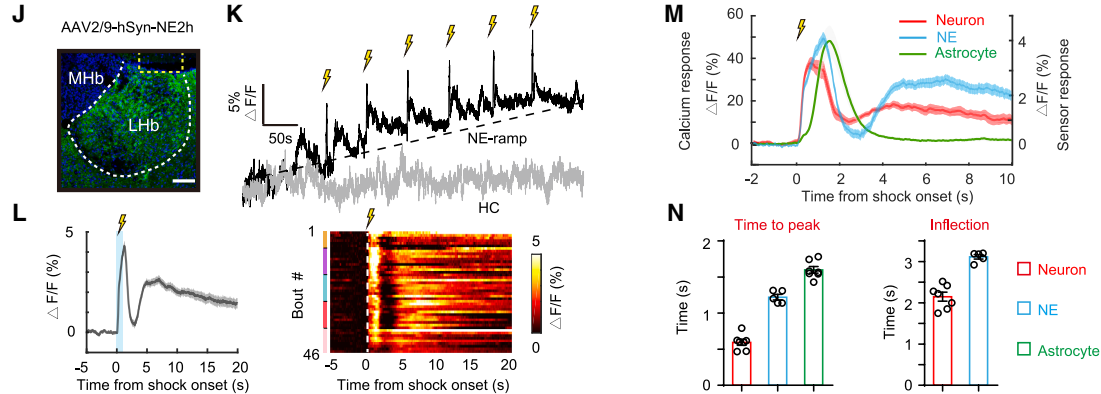
Activation of LHB astrocytic Ca^{2+} by stimulation of LHB neurons in vivo but not in vitro



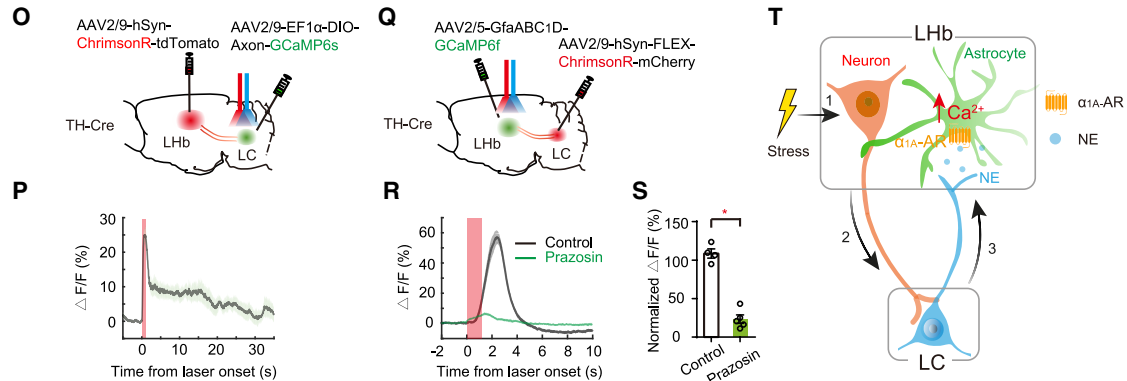
Response of LHB astrocytes to shock is mediated by α_{1A} -AR



Stress triggers sequential activation of neurons, NE signals and astrocytes in LHB



LHB-LC loop contributes to LHB astrocytic Ca^{2+} response



(legend on next page)

The above data suggest that NE may be the potential link mediating the neuron-to-astrocyte crosstalk in the LHB. To further substantiate this hypothesis, we next explored the anatomical and functional connections between the LHB and LC, the hub for noradrenergic neurons and potential source of NE.^{73–75} First, optogenetic activation of LHB terminals in the LC evoked calcium responses of LC-NE neurons (Figures 3P, S8A, and S8B), suggesting that there is functional input from LHB neurons into the LC to activate NE neurons. Next, GCaMP signals were detected from the TH⁺ LC neurons in the LHB (Figure S8A), verifying that, anatomically, there is a direct afferent input from the LC-NE neurons to the LHB region. Furthermore, optogenetic activation of LC-NE neuron terminals in the LHB evoked calcium responses of LHB astrocytes (Figures 3Q, 3R, S8C, and S8D), which was blocked by α 1-AR antagonist prazosin (Figure 3S). Prazosin also abolished LHB astrocytic calcium signals evoked by activation of LHB neurons *in vivo* (Figures S8E–S8H). Furthermore, optogenetic inhibition of LHB neurons or chemogenetic inhibition of LC-NE neurons significantly decreased the calcium responses of LHB astrocytes evoked by FS stress (Figures S8I–S8P). Collectively, this set of data delineates a pathway in which stress activates LHB neurons as one of the inputs to LC, in turn recruiting LC-NE neurons, which, through the release of NE, stimulate the astrocytic calcium in the LHB (Figure 3T).

Astrocyte-to-neuron crosstalk in the LHB

We next explored the signaling pathway mediating the potential crosstalk from LHB astrocytes to neurons. We first determined the effect of LHB astrocytic activation on LHB neuronal activities in freely moving mice (Figures 4A–4E). To mimic the activation of Gq-coupled α 1-AR signaling,⁷⁶ we expressed the human M3 muscarinic DREADD coupled to Gq (hM3Dq) under the GfaABC1D promoter for chemogenetic activation of LHB astrocytes (Figure 4A). Upon injection of the ligand of hM3Dq clozapine, *in vivo* fiber photometry recording revealed significantly elevated, dose-dependent bulk calcium activity in LHB neurons (Figures 4B and 4C). There was also an increase in the immunohistochemical signals of c-Fos, a cellular marker of cell activation, in LHB neurons (Figures 4D and 4E).

In LHB brain slices, calcium imaging recording also revealed successful activation of astrocytes and neurons upon chemogenetic activation of astrocytes (Figures S9A–S9F). In particular, 55% of the recorded neurons (148 of 267) showed significantly increased calcium signals upon clozapine N-oxide (CNO) application (Figure S9F). Among these, 38% were silent and 55% and 7% showed irregular and regular baseline activity, respectively, before the CNO application (Figure S9F). To achieve astrocytic activation in a more transient and temporally controlled manner, we then tried optogenetic activation by expressing chicken opsin 5 (cOpn5), a light-sensitive Gq-coupled GPCR that can trigger a blue-light-induced elevation in intracellular calcium,⁷⁷ in the LHB

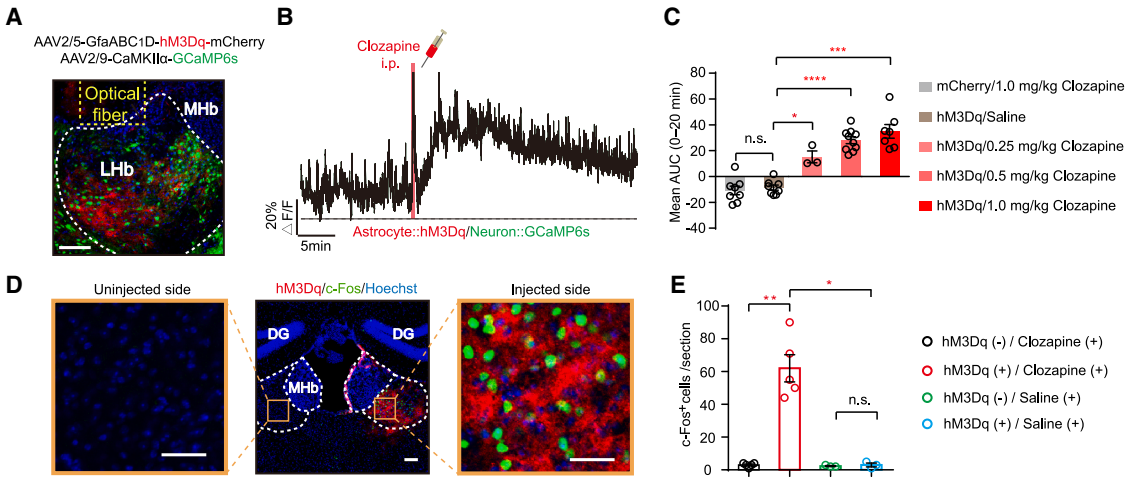
Figure 3. Neuron-to-astrocyte crosstalk in LHB during FS

- (A) Schematic illustrating optogenetic activation of ChrimsonR-expressing neurons and fiber photometry recording of nearby GCaMP6f-expressing astrocytes in LHB *in vivo*.
(B and E) Astrocytic calcium responses to LHB neuronal ChrimsonR activation (1 s, 40 Hz) *in vivo* (B) and in LHB slices (E).
(C and F) Mean astrocytic calcium responses to varying stimulation frequencies *in vivo* (C, $n = 5$ mice) and in LHB slices (F, $n = 7$ slices, 3 mice).
(D) Schematic illustrating optogenetic activation of ChrimsonR-expressing neurons and two-photon imaging of nearby GCaMP6f-expressing astrocytes in LHB slices.
(G) Schematic of *in vivo* fiber photometry recording of LHB astrocytes in response to FS after i.p. injection of various receptor blockers.
(H) Bar graph showing effects of MPEP ($n = 7$ mice), LY341495 ($n = 7$ mice), scopolamine ($n = 8$ mice), mecamylamine ($n = 6$ mice), prazosin ($n = 10$ mice), propranolol ($n = 7$ mice), and atipamezole ($n = 7$ mice) on FS-evoked calcium signals in LHB astrocytes. Each circle represents one mouse.
(I) Bar graph showing effects of α 1-AR subtype-selective antagonists, including silodosin ($n = 8$ mice), L-765314 ($n = 6$ mice), and BMY 7378 ($n = 7$ mice) on FS-evoked calcium signals in LHB astrocytes. Each circle represents one mouse.
(J–L) *In vivo* fiber photometry recording of NE sensor signals in LHB during FS. Viral expression (J, GFP and Hoechst staining) after injection of AAV2/9-hSyn-NE2h and optic fiber placement (yellow dotted line) in LHB, the boundary of which is outlined by the white dotted line. Scale bar, 100 μ m. Example trace (K) of LHB NE sensor signals during FS (black) and homecage (HC, gray). Plots (L, left) of deltaF/F ratio of NE sensor signals aligned to FS onset. Solid lines indicate mean and shaded areas indicate SEM. Heatmap (L, right) of deltaF/F ratio of NE sensor signals in the LHB aligned to FS onset ($n = 46$ trials, 5 mice). Color bars on the left indicate different mice.
(M) Plots of deltaF/F ratio of calcium signals from LHB neurons, astrocytes, and NE-sensor signals aligned to FS onset. Solid lines indicate mean and shaded areas indicate SEM. Data are from (E)–(H) and (L).
(N) Average time to peak of LHB neuronal calcium signals, LHB-NE-sensor signals, and LHB astrocytic calcium signals from FS onset (left) and average time to inflection of LHB neuronal calcium signals and LHB-NE-sensor signals (right). Data are from (E)–(H) and (L).
(O) Schematic illustrating optogenetic activation of LHB-LC terminals and fiber photometry recording of LC-NE neurons in TH-Cre mice.
(P) Calcium response of LC-NE neurons to optogenetic activation of LHB-LC terminals (1 s, 40 Hz). Plots of deltaF/F ratio of calcium signals aligned to laser onset ($n = 3$ mice). Red line represents light on. Solid lines indicate mean and shaded areas indicate SEM.
(Q) Schematic illustrating optogenetic activation of LCTH-LHB terminals and fiber photometry recording of LHB astrocytes in TH-Cre mice.
(R) Calcium response of LHB astrocytes to optogenetic activation of LCTH-LHB terminals (1 s, 40 Hz). Plots of averaged deltaF/F ratio of astrocytic calcium signal induced by optogenetic activation of LCTH-LHB terminals after i.p. injection of saline (black, $n = 4$ mice) or prazosin (green, $n = 5$ mice), aligned to laser onset. Red line represents light on. Solid lines indicate mean and shaded areas indicate SEM.
(S) Bar graph showing effects of prazosin on astrocytic calcium signals induced by optogenetic activation of LCTH-LHB terminals. Each circle represents one mouse.
(T) Working model summarizing the neuron-to-astrocyte crosstalk in LHB during FS. Stress activates LHB neurons, which recruit LC-NE neurons to elevate LHB astrocytic calcium via NE- α 1A-AR signaling.

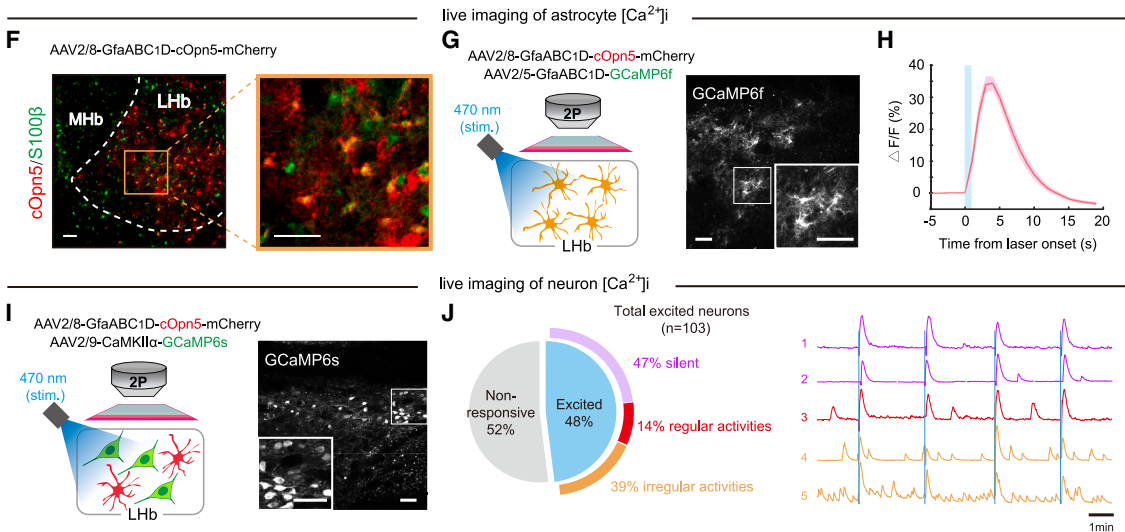
* $p < 0.05$; ** $p < 0.01$; *** $p < 0.001$; **** $p < 0.0001$; n.s., not significant. Data are represented as mean \pm SEM.

See also Figures S4–S8.

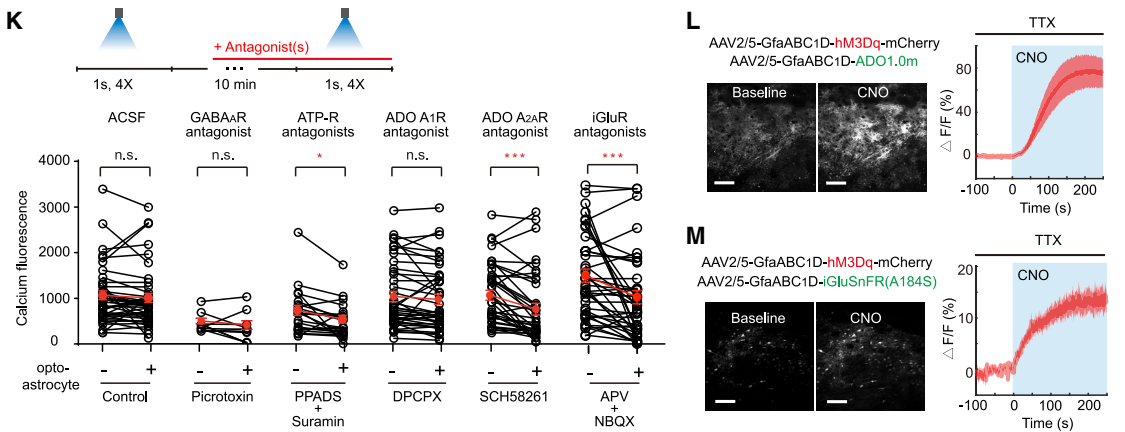
Chemogenetic activation of astrocytic Gq pathway elicits neuronal activities in vivo



Optogenetic activation of astrocytic Gq pathway elicits neuronal Ca²⁺ activities in LHb slices



Activation of LHb astrocytic Gq pathway elicits neuronal Ca²⁺ activities through glutamate and adenosine



(legend on next page)

astrocytes (Figure 4F). Light stimulation (1 s, 473 nm) significantly evoked calcium activities in LHB astrocytes (Figures 4G and 4H). And the signals decayed much faster than CNO-evoked ones (7.8 ± 2.3 s vs. 62.2 ± 23.9 s; Figures 4H and S9C), closer to the FS-evoked physiological condition (Figure 1G). Using this approach, we found that, upon optogenetic activation of LHB astrocytes, 48% (103 of 216) recorded LHB neurons were excited (Figures 4I, 4J, S10A, and S10B). Among these, 47% were silent and 39% and 14% showed irregular and regular baseline activity, respectively, before the stimulation (Figure 4J). Overall, both chemogenetic and optogenetic activation of the astrocyte-Gq pathway significantly increased the activities of LHB neurons.

Although the optogenetic activation of astrocyte-Gq may be less efficient than the chemogenetic method, the change it caused is more physiological (in terms of signal duration; Figures 1A–1G and 4H), which allowed us to identify the gliotransmitter(s) mediating the LHB astrocyte-neuron crosstalk. Calcium signals in astrocytes are known to facilitate the release of various gliotransmitters, including glutamate,^{78–80} GABA,^{81–83} and ATP or its immediate degradation product adenosine.^{63,84–87} Therefore we measured LHB neuronal calcium activities triggered by optogenetic stimulation of LHB astrocytes in brain slices in the presence of antagonists for these gliotransmitter receptors (Figure 4K). Although antagonists for the GABA_A (picrotoxin) and adenosine A₁ (A₁R, DPCPX) receptors did not show any effect (Figure 4K), those blocking adenosine A_{2A} (A_{2A}R, SCH58261) or ionotropic glutamate receptors (iGluR, APV + NBQX) (Figures 4K and S10C–S10E) significantly suppressed astrocyte-stimulated neuronal calcium responses (SCH58261: 34.8% reduction; APV + NBQX: 32% reduction; Figure 4K). 52% and 44% of astrocyte-excited neurons exhibited significantly reduced calcium activities in response to adenosine A_{2A}R and iGluR blockade, respectively (Figures S10D and S10E). Moreover, A_{2A}R and iGluR antagonists showed an additive effect (Figure S10F). All astrocyte-excited neurons exhibited reduced activity after incubation with both antagonists. Among them,

25% showed A_{2A}R-specific inhibition, 35% showed iGluR-specific inhibition, and the remaining 40% exhibited dual-antagonist-dependent inhibition (Figures S10G and S10H), suggesting that partially overlapping but largely distinct neuronal populations are activated by adenosine and glutamate released from astrocytes. On the other hand, blockade of ATP receptors (ATP-R, PPADS + suramin) had a significant but much smaller effect on astrocyte-stimulated neuronal calcium responses (10% reduction; Figure 4K). Furthermore, genetically encoded sensors of adenosine (ADO1.0m)⁸⁸ or glutamate (iGluSnFR)⁸⁹ revealed that activation of the astrocyte-Gq pathway (CNO, 1 μ M, with TTX to exclude indirect release from neuronal activation) significantly increased the levels of adenosine (Figure 4L) and glutamate (Figure 4M). Under the temporal resolution (0.92 Hz frame rate) examined, although adenosine signals exhibited a synchronized increase, glutamate signals showed different time to peak in the soma and distal processes (Figure S11). These results suggest that activation of LHB astrocytes can lead to activation of LHB neurons by boosting extracellular ATP/adenosine and glutamate.

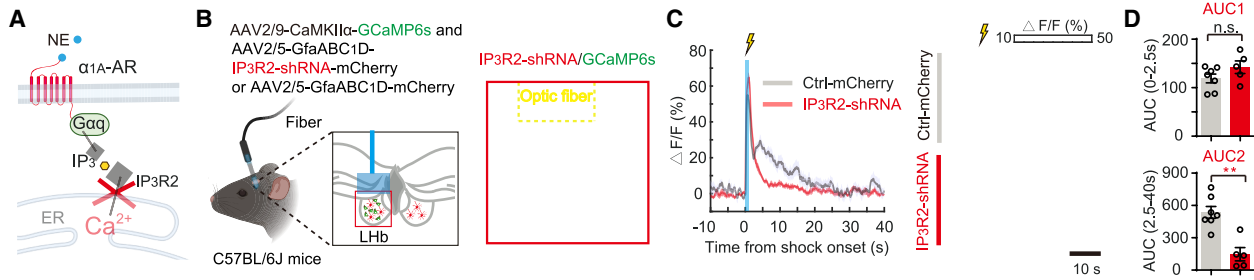
LHB astrocytes account for the second phase of LHB neural activity and NE release

We next investigated the functional impact of LHB astrocytic activities on the FS-evoked LHB neuronal activity and NE signaling *in vivo* (Figure 5). As shown in Figure 3I, we had mapped the NER type involved in the LHB-astrocyte Ca²⁺ response to be α_{1A} -AR, a Gq-coupled GPCR, which initiates IP₃-dependent Ca²⁺ release from intracellular endoplasmic reticulum stores.⁹⁰ Therefore, we first applied two strategies to specifically interfere with this signaling pathway in LHB astrocytes: (1) knockdown of IP₃R2 receptors using a short hairpin RNA (shRNA) to block internal release of Ca²⁺ (Figure 5A)^{90,91} and (2) expression of a 122-residue inhibitory peptide from β -AR kinase1 (β ARK) to interfere with Gq-GPCR signaling⁹² (Figure 5E). AAV expression of these two constructs under the GfaABC1D promoter significantly reduced FS-evoked calcium in LHB astrocytes by 68% and

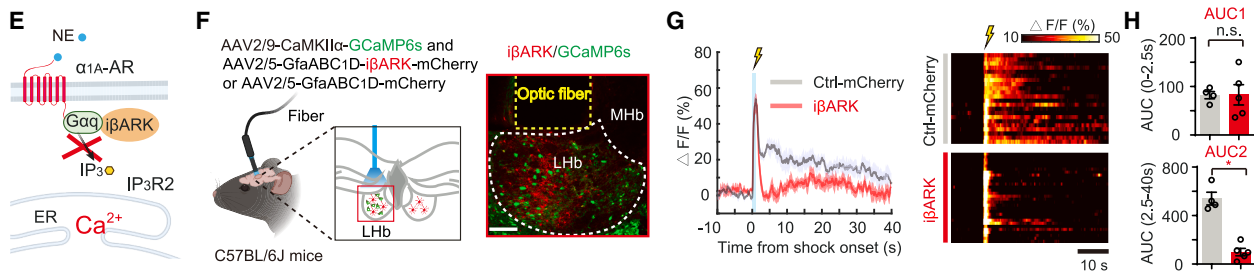
Figure 4. Astrocyte-to-neuron crosstalk in LHB

- (A) Representative image showing viral expression of GCaMP6s in LHB neurons and hM3Dq in LHB astrocytes. Scale bar, 100 μ m.
- (B and C) *In vivo* fiber photometry recording of LHB neuronal calcium response to LHB astrocytic hM3Dq activation. Representative raw trace (B) and bar chart (C) showing mean AUC of neuronal calcium signals following an i.p. injection of saline or clozapine. Each circle represents one mouse.
- (D) Representative images of c-Fos IHC signals following unilateral astrocytic hM3Dq activation in LHB. Note that c-Fos signals appear only on injected side. Green, c-Fos; blue, Hoechst. Scale bar, 40 μ m.
- (E) Quantification of total c-Fos⁺ cells in LHB.
- (F) Representative image of LHB slices with viral expression of cOpn5 in astrocytes. Scale bar, 40 μ m.
- (G) Schematic (left) and representative two-photon image (right) illustrating optogenetic activation of cOpn5-expressing astrocytes while recording their calcium responses in LHB. Scale bar: 50 μ m.
- (H) Plots of $\Delta F/F$ ratio of LHB astrocytic calcium signals aligned to laser onset. Solid lines indicate mean and shaded areas indicate SEM.
- (I) Schematic (left) and representative two-photon image (right) illustrating optogenetic activation of cOpn5-expressing astrocytes while recording neuronal calcium responses in LHB. Scale bar: 50 μ m.
- (J) Pie chart illustrating percentage of excited neurons by astrocytic-cOpn5 activation (left, $n = 4$ slices, 4 mice). Colored outer circle indicates percentage of three types (according to baseline activity) among astrocytic-cOpn5-excited neurons. Representative raw calcium traces from the three types of astrocytic cOpn5-excited neurons (right). Blue line represents light on.
- (K) Bar graph showing effects of artificial CSF (ACSF) ($n = 3$ slices, 3 mice), picrotoxin ($n = 2$ slices, 2 mice), PPADS and suramin ($n = 2$ slices, 2 mice), DPCPX ($n = 3$ slices, 3 mice), SCH58261 ($n = 2$ slices, 2 mice), and APV and NBQX ($n = 3$ slices, 3 mice) on astrocytic cOpn5-evoked neuronal calcium signals in LHB slices. Each circle represents one neuron.
- (L and M) Illustration of AAVs used for expressing hM3Dq and ADO1.0m (L) or iGluSnFR (M) in LHB astrocytes (left top), fluorescence images (left bottom), and traces (right) illustrating astrocyte-induced adenosine (L) or glutamate (M) release in LHB slice ($n = 3$ slices, 3 mice per sensor). Scale bar: 100 μ m.
- * $p < 0.05$; ** $p < 0.01$; *** $p < 0.001$; **** $p < 0.0001$; n.s., not significant. Data are represented as mean \pm SEM.
- See also Figures S9–S11.

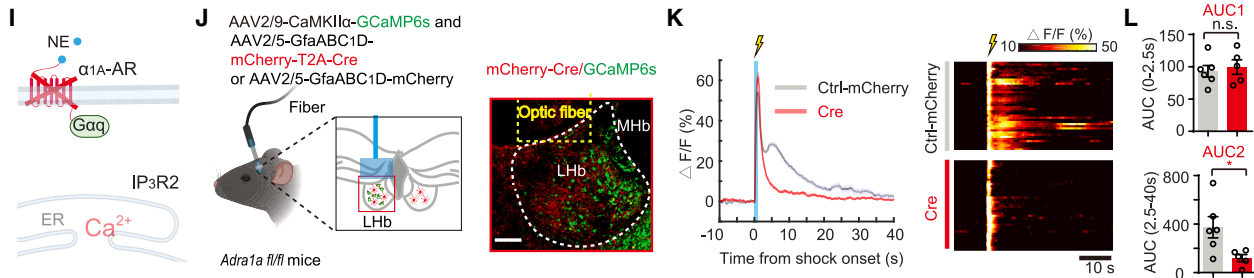
Inhibition of astrocytic Ca^{2+} by astrocyte-specific IP₃R2 knockdown eliminates FS-evoked second wave of neuronal activities



Inhibition of astrocytic Ca^{2+} by β ARK eliminates FS-evoked second wave of neuronal activities



Conditional knockout of α_{1A} -AR in LHb astrocytes eliminates FS-evoked second wave of neuronal activities



Inhibition of astrocytic Ca^{2+} by astrocyte-specific IP₃R2 knockdown decreases FS-evoked NE release

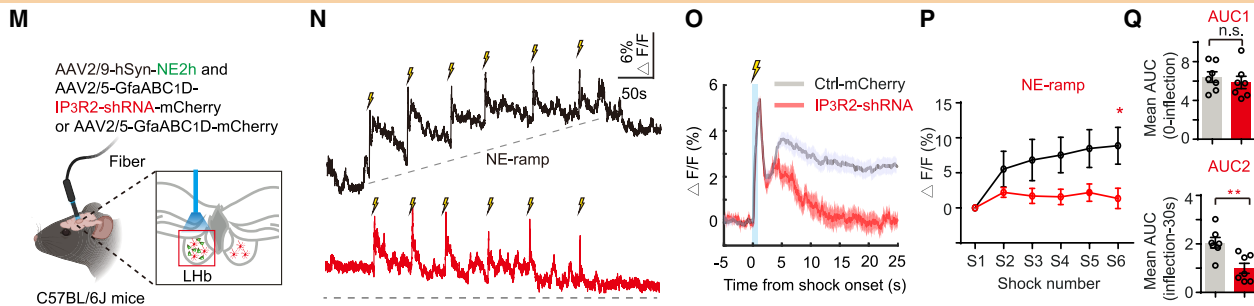


Figure 5. LHb astrocytic Ca^{2+} signaling is required for the second-phase neuronal activities and NE release

(A) Illustration of blockade of astrocytic calcium signaling by IP₃R2-shRNA.

(B) Left: schematic illustrating the expression of astrocyte-specific IP₃R2-shRNA or Ctrl-mCherry in bilateral LHb and neuron-GCaMP6s in unilateral LHb, and fiber photometry recording of LHb neurons. Right: viral expression of IP₃R2-shRNA in LHb astrocytes and GCaMP6s in LHb neurons. Scale bar, 100 μ m.

(C) Plots of averaged $\Delta F/F$ ratio (left) and heatmap (right) of LHb neuronal calcium signals aligned to FS onset in mice expressing Ctrl-mCherry (gray, $n = 69$ trials, 7 mice) or IP₃R2-shRNA (red, $n = 50$ trials, 5 mice) in LHb astrocytes.

(D) Quantification of AUC1 in 0–2.5 s (top) and AUC2 in 2.5–40 s (bottom) of FS-evoked LHb neuronal calcium signals in mice expressing Ctrl-mCherry or IP₃R2-shRNA in LHb astrocytes. Each circle represents one mouse.

(E) Illustration of blockade of astrocytic calcium signaling by β ARK.

(legend continued on next page)

51%, respectively (Figures S12A–S12F). To examine the contribution of LHB astrocytes to neuronal calcium activities during FS stress, we then injected either one of these two viruses into the bilateral LHB, expressed GCaMP6s under the CaMKII α promoter in the unilateral LHB, and installed optic fibers above the LHB for *in vivo* photometry recording (Figures 5B and 5F). Notably, the second-phase LHB neuronal activity evoked by FS was largely eliminated by expression of IP₃R2-shRNA (Figures 5C and 5D) or i β ARK (Figures 5G and 5H) in LHB astrocytes: the first-phase FS-evoked neuronal calcium signals remained unchanged (Figures 5D, 5H, S13A–S13D, and S13F–S13I); in contrast, the second-phase FS-evoked neuronal calcium signals, reflected in the AUC from 2.5 to 40 s (AUC2), were greatly reduced (Figures 5D and 5H). Consequently, the total AUC from the two phases was largely reduced (Figures S13E and S13J).

As a third strategy to block LHB-astrocyte Ca²⁺, we then expressed GfaABC1D-promoter-driven Cre in the LHB of *Adra1a*-floxed mice to knock down local α_{1A} -AR (Figures 5I, 5J, and S13K–S13O). This genetic approach also led to diminished second-phase FS-evoked neuronal calcium signals (Figures 5K and 5L). Together, these results suggest that LHB astrocytic calcium activities are required for second-phase LHB neuronal activity in response to stress.

We then examined the impact of blocking LHB astrocytic Ca²⁺ on NE release by simultaneously expressing IP₃R2-shRNA and NE sensor in the LHB (Figures 5M–5Q). Photometry recording revealed that IP₃R2-shRNA significantly reduced the second-phase NE signals evoked by FS stress (Figures 5N, 5O, and 5Q). Although the AUC of the first-phase FS-evoked NE signals showed no difference, the AUC of the second-phase FS-evoked NE signals was largely reduced in mice expressing IP₃R2-shRNA compared with control (Figure 5Q). Additionally, the ramp-up of NE signals over multiple FSs was also inhibited (Figures 5N and 5P). These results suggest that LHB astrocytes do not affect the first-phase but strongly contribute to the second-phase NE release in response to stress. Combined with the temporal dynamic data in Figure 3M, results in Figure 5 suggest that during

FS, Ca²⁺ activity of LHB astrocytes leads to the reactivation of LHB neurons and the subsequent reactivation of LC-NE neurons and NE release.

Activation of LHB astrocytes facilitates depression-like behaviors

We next explored the functional consequence of LHB-astrocytic activation on the behavioral response to stress (Figure 6). We first tried to activate LHB astrocytes by expressing GfaABC1D-hM3Dq in the LHB (Figure 6D) in a subthreshold stress protocol (1 mA, 1 s, 6 \times FS delivered within 6 min; Figure 6A). This protocol by itself did not induce depression-like phenotypes (Figure 6B). However, when LHB astrocytes were chemogenetically activated (i.p., deschloroclozapine [DCZ], 0.5 mg/kg) before the first FS, mice developed depression-like phenotypes after this subthreshold protocol (Figures 6C–6E). Compared with the mCherry-expressing group, mice expressing hM3Dq in LHB astrocytes were more immobile in the forced swim test (FST), which models behavioral despair, and showed less preference for sucrose water in the sucrose preference test (SPT), which models anhedonia (Figure 6E).

Inhibition of LHB astrocytes prevents stress-induced depression-like behaviors

We next tested whether LHB-astrocytic activity is necessary for stress-induced depression. We tried to inactivate LHB astrocytes by expressing the IP₃R-shRNA under the GfaABC1D promoter (Figure 6I). Mice were then exposed to a series of inescapable and unpredictable FS stress (1 mA, 1 s, 20 \times FS delivered within 20 min; Figure 6F), which was shown to induce depression-like behaviors (Figure 6G).^{15,93} Compared with the 6 \times FS subthreshold protocol, 20 \times FS induced more frequent and more sustained phasic NE signals (Figure S14). Inhibition of LHB astrocytes with IP₃R2-shRNA caused a pronounced reduction in depressive-like phenotypes (Figures 6H–6J), reducing immobility in the FST and increasing sucrose preference in the SPT (Figure 6J). Knockout of α_{1A} -AR in LHB astrocytes also

(F) Left: schematic illustrating the expression of astrocyte-specific i β ARK or Ctrl-mCherry in bilateral LHB and neuron-GCaMP6s in unilateral LHB, and fiber photometry recording of neurons in LHB. Right: viral expression of i β ARK in LHB astrocytes and GCaMP6s in LHB neurons. Scale bar, 100 μ m.

(G) Plots of averaged deltaF/F ratio (left) and heatmap (right) of LHB neuronal calcium signals aligned to FS onset in mice expressing Ctrl-mCherry (gray, $n = 22$ trials, 4 mice) or i β ARK (red, $n = 30$ trials, 5 mice) in LHB astrocytes.

(H) Quantification of AUC1 in 0–2.5 s (top) and AUC2 in 2.5–40 s (bottom) of FS-evoked LHB neuronal calcium signals in mice expressing Ctrl-mCherry or i β ARK in LHB astrocytes. Each circle represents one mouse.

(I) Illustration of blockade of astrocytic calcium signaling by conditional knockout of α_{1A} -AR in LHB astrocytes.

(J) Left: schematic illustrating the expression of astrocyte-specific Cre or Ctrl-mCherry in bilateral LHB and neuron-GCaMP6s in unilateral LHB, and fiber photometry recording of neurons in LHB in *Adra1a*^{fl/fl} mice. Right: expression of Cre in LHB astrocytes and GCaMP6s in LHB neurons (stained with antibody against mCherry). Scale bar, 100 μ m.

(K) Plots of averaged deltaF/F ratio (left) and heatmap (right) of LHB neuronal calcium signals aligned to FS onset in mice expressing Ctrl-mCherry (gray, $n = 40$ trials, 6 mice) or Cre (red, $n = 42$ trials, 5 mice) in LHB astrocytes.

(L) Quantification of AUC1 in 0–2.5 s (top) and AUC2 in 2.5–40 s (bottom) of FS-evoked LHB neuronal calcium signals in mice expressing Ctrl-mCherry or Cre in LHB astrocytes. Each circle represents one mouse.

(M) Schematic illustrating the expression of astrocyte-specific IP₃R2-shRNA or Ctrl-mCherry in bilateral LHB and NE sensor in unilateral LHB, and fiber photometry recording of NE sensor in LHB.

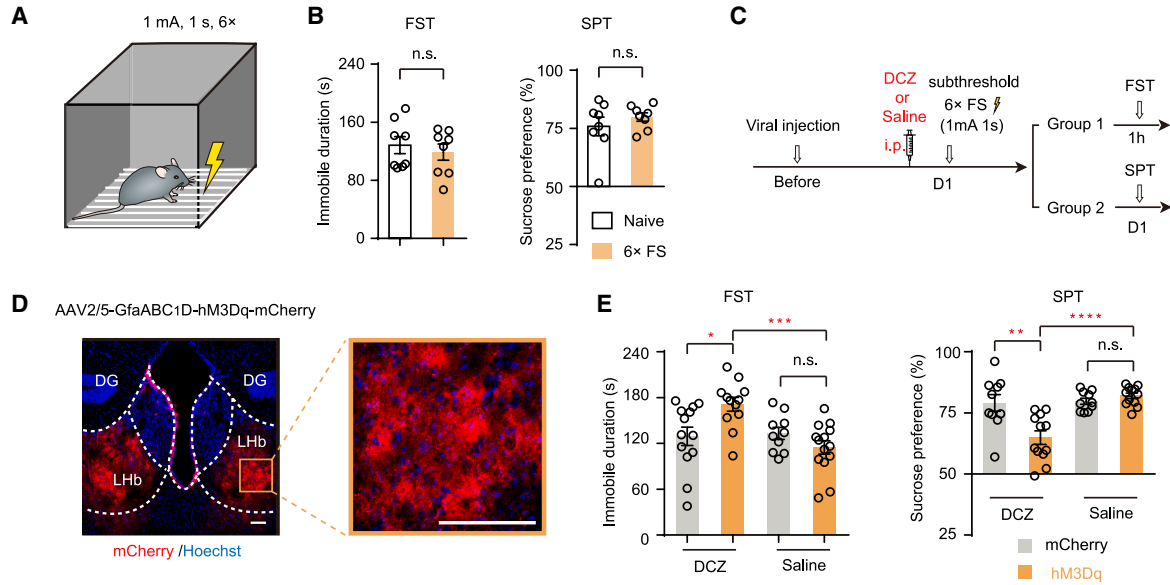
(N and O) Example trace (N) and plots of averaged deltaF/F ratio (O) of LHB-NE signals during FS in mice expressing Ctrl-mCherry (gray, $n = 42$ trials, 7 mice) or IP₃R2-shRNA (red, $n = 42$ trials, 7 mice) in LHB astrocytes.

(P and Q) Basal (tonic) deltaF/F ratio (P) and AUC1 (from 0 to inflection point; Q, top) and AUC2 (from inflection point to 30 s; Q, bottom) of LHB-NE signals aligned to FS onset of LHB-NE signals in response to FS in mice expressing Ctrl-mCherry (gray) or IP₃R2-shRNA (red) in LHB astrocytes.

* $p < 0.05$; ** $p < 0.01$; *** $p < 0.001$; **** $p < 0.0001$; n.s., not significant. Data are represented as mean \pm SEM.

See also Figures S12 and S13.

Activation of LHB astrocytic Gq pathway facilitates depression-like behaviors



Inhibition of LHB astrocytic activities prevents depression-like behaviors

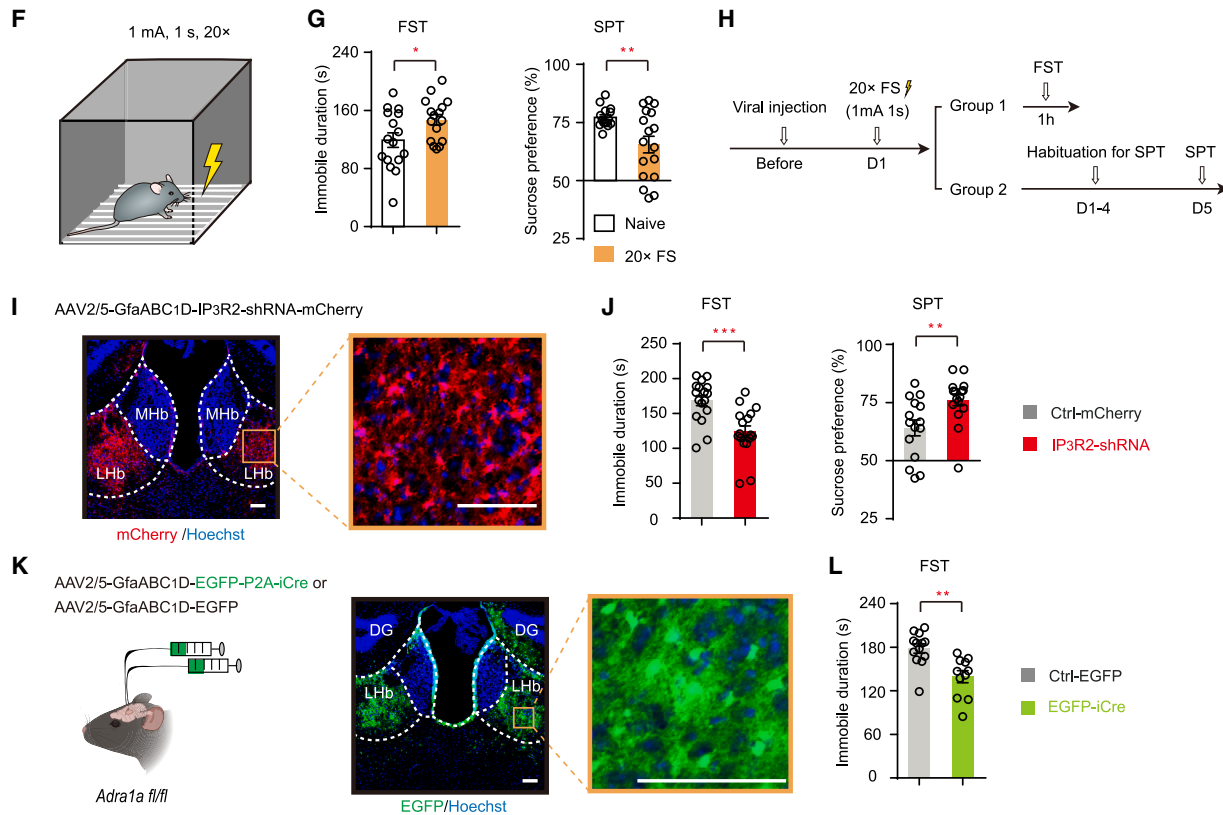


Figure 6. LHB astrocytes regulate stress-induced depression-like behaviors

(A) Schematic of a subthreshold depression-induction protocol with 6× FS.
 (B) Subthreshold 6× FS did not induce depression-like behaviors in FST ($n = 8$, 8 mice, naive vs. FS) and SPT ($n = 8$, 8 mice, naive vs. FS).
 (C) Experimental paradigm for activating Gq pathway of LHB astrocytes during the subthreshold depression-induction protocol.

(legend continued on next page)

caused a significant reduction in depressive-like phenotypes in the FST (Figures 6K and 6L).

NE reuptake inhibitors block FS-evoked phasic NE release and astrocytic activity in the LHb

The foregoing results indicate that NE-dependent LHb astrocytic calcium activity facilitates stress-induced depressive-like behaviors. This is somewhat counter-intuitive, given that the antidepressant norepinephrine reuptake inhibitors (NRIs) and serotonin-norepinephrine reuptake inhibitors (SNRIs) increase extracellular concentration of NE.⁹⁴ We therefore examined the effect of reboxetine, a specific NE reuptake inhibitor,⁹⁵ on the NE level (Figures 7A–7D) and astrocytic activity in the LHb (Figures 7E–7H). When injected at baseline, reboxetine yielded a slow and significant increase in LHb baseline NE signals (Figures 7A and 7B). However, interestingly, there was no significant change in calcium activity of LHb astrocytes (Figures 7E and 7F). Notably, when reboxetine was injected before the FS, it abolished both the FS-induced phasic NE release (Figures 7C and 7D) as well as the LHb astrocytic calcium activity (Figures 7G and 7H). Additionally, SNRI imipramine also blocked FS-evoked phasic increase of NE and astrocytic calcium activity in the LHb (Figure S15).

We then investigated the functional impact of blocking NE transporter (NET) on the FS-evoked LHb neuronal activity. Following an i.p. injection of reboxetine, the first-phase FS-evoked neuronal calcium signals remained unchanged (Figure 7K); in contrast, the second-phase FS-evoked neuronal calcium signals were largely eliminated (Figure 7K). Consequently, the total AUC was significantly reduced (Figure 7K). Collectively, these results demonstrated that although NE reuptake inhibitors induce an increase of NE in a slowly ramping manner, they effectively block FS-induced phasic NE increase. Consequently, they do not trigger—but rather inhibit—LHb astrocytic calcium activities and second-phase neural activities in response to stress.

The above results predicted that NE reuptake inhibitors may prevent depression-like phenotypes induced by FS. To test that, we i.p. injected mice with reboxetine 20 min before the 20× FS (1 mA, 1 s, 20× FS delivered within 20 min) stimulation. Compared with the saline-injected group, reboxetine-injected mice showed significantly decreased immobility time in the FST (Figure 7L), indicating reduced depression-like behavior.

DISCUSSION

This work defines a stress-induced recurrent network involving LHb neurons, LC-NE neurons, and LHb astrocytes (Figure 7M): stress first activates LHb neurons, which triggers astrocytic calcium surge via LC- and α_{1A} -AR-dependent noradrenergic signaling (Figure 3); in tandem, through gliotransmitters glutamate and ATP/adenosine, LHb astrocytes drive the second-phase of both local LHb neural activity and NE release (Figures 4 and 5), establishing a positive feedback loop where LHb astrocytes act as a critical signaling relay. Together, these findings establish a framework for neuron-astrocyte interplay in stress-driven depression, highlighting the LHb-LC loop as a central hub in psychiatric disorders.

Functional implications and possible mechanisms underlying stress-induced biphasic calcium activities in LHb neurons

A key question in neurophysiology is how neurons sustain persistent activity following transient sensory stimuli. Previous studies have identified mechanisms involving slow-acting neuromodulators or recurrent neural networks.^{96,97} Our study reveals yet another mechanism for a persistent neural dynamic pattern, in the context of FS stress, driven by astrocyte signaling. In particular, we observed biphasic calcium signals in LHb neurons: a fast, time-locked first phase and a slow, heavy-tailed second phase. Notably, more calcium enters neurons during the second phase (Figure 2D), which may activate calcium-dependent genes. On the other hand, Gq pathway activation in astrocytes can also influence gene transcription.²⁶ In light of this, it is of interest to note that we have previously identified several neuronal genes (e.g., β CaMKII⁹⁸) and glial genes (e.g., Kir4.1¹⁹) to be upregulated in depression-like states. It is foreseeable that the calcium events we identified here may engage transcriptional changes in both neurons and astrocytes, contributing to depression etiology over a long timescale.

In contrast to the LHb, the five other brain regions examined did not exhibit biphasic calcium activation under FS stress (Figure S2), suggesting a region-specific mechanism. Several factors may explain the dynamics in the LHb. First, LHb neurons possess distinct intrinsic properties, containing calcium-permeable AMPA receptors (CP-AMPA)^{14,16,99} and pacemaker

(D) Viral expression of hM3Dq in LHb astrocytes. Scale bar, 100 μ m.

(E) Depression-like behaviors in FST ($n = 13, 12, 10, 14$ mice, Ctrl-mCherry/DCZ, hM3Dq/DCZ, Ctrl-mCherry/saline, hM3Dq/Saline) and SPT ($n = 10, 12, 10, 12$ mice, Ctrl-mCherry/DCZ, hM3Dq/DCZ, Ctrl-mCherry/saline, hM3Dq/Saline) of mice expressing Ctrl-mCherry (gray) or hM3Dq (blue) in LHb astrocytes.

(F) Schematic of a depression-induction protocol with 20× FS.

(G) 20× FS induced depression-like behaviors in FST ($n = 16, 16$ mice, naive vs. FS) and SPT ($n = 15, 17$ mice, naive vs. FS).

(H) Experimental paradigm for inhibiting LHb astrocytic calcium signaling during the depression-induction protocol.

(I) Viral expression of IP₃R2-shRNA in LHb astrocytes. Scale bar, 100 μ m.

(J) Depression-like behaviors in FST ($n = 17, 17$ mice, Ctrl-mCherry vs. IP₃R2-shRNA) and SPT ($n = 15, 16$ mice, Ctrl-mCherry vs. IP₃R2-shRNA) of mice expressing Ctrl-mCherry (gray) or IP₃R2-shRNA (red) in LHb astrocytes.

(K) Schematic illustrating the viral expression of astrocyte-specific iCre or Ctrl-EGFP in LHb astrocytes (left). Illustration of viral expression of iCre in LHb astrocytes in *adra1A*^{fl/fl} mice (middle, right, GFP staining). Scale bar, 100 μ m.

(L) Depression-like behaviors in FST ($n = 13, 11$ mice, Ctrl-EGFP vs. iCre) of *adra1A*^{fl/fl} mice expressing Ctrl-EGFP (gray) or iCre (green) in LHb astrocytes.

* $p < 0.05$; ** $p < 0.01$; *** $p < 0.001$; **** $p < 0.0001$; n.s., not significant. Data are represented as mean \pm SEM.

See also Figure S14.

channels (e.g., hyperpolarization-activated cyclic-nucleotide-gated [HCN] and T-type calcium channels).^{17,100} Through the glutamate-CP-AMPA receptors and adenosine-A₂-receptor-coupled HCN channels,^{84,101} gliotransmitters released from LHB astrocytes may drive the second-phase neural calcium activation. Second, variations in gliotransmitter types and astrocytic activity dynamics across brain regions may also contribute. In the LHB, the tight temporal coupling (~1 s apart) between neuronal and astrocytic calcium signals during FS stress may enable astrocyte-released glutamate to activate N-methyl-D-aspartate (NMDAR)-mediated Ca²⁺ signals in depolarized neurons, thereby facilitating the second-phase activation.

Functional implications and possible mechanisms underlying stress-induced rapid activities in LHB astrocytes

Compared with the five other brain regions recorded, LHB astrocytes exhibited the earliest calcium response to FS stress (Figures 1D–1G). This property may stem from several potential mechanisms. First, NE release in the LHB may occur earlier than in other regions. Second, regional differences in astrocytic gap junction coupling,¹⁰² which influences the speed of calcium propagation, could play a role. Third, variations in neuromodulator receptor signaling across brain regions may affect the timing and magnitude of calcium responses. For example, auditory cortical astrocytes are regulated by ACh during FS stress,⁴⁰ whereas LHB astrocytes are regulated by NE (Figure 3H). Lastly, local neuronal activity may differentially modulate astrocyte sensitivity to NE, as shown in the visual cortex, where neuronal activity acts as a gain control for astrocytic responses to NE.⁴⁴

Furthermore, the function of the stress-induced LHB astrocytic activity may extend beyond the local neuron-astrocyte network. Through the second-wave activation of LC-NE neurons, which project broadly across the brain,^{103,104} local LHB astrocytes may influence global neural activity.

Phasic and tonic NE release

Monoamine release is often subdivided into phasic and tonic modes.^{105–107} Recent biosensor studies have revealed both slowly ramping and phasic monoamine signals in behaving mice, such as striatal dopamine during reward-directed tasks and basal forebrain NE under FS stress.^{108,109} These findings suggest that different release modes may support distinct brain functions.

In this study, we identified two distinct NE signaling modes in the LHB during FS stress: rapid phasic bursts and slowly ramping tonic signals. Phasic NE release was critical for activating LHB astrocytic calcium, with large calcium transients time-locked to phasic NE signals. Notably, despite elevated tonic NE levels in late stress sessions, astrocytic calcium was not induced (Figure S7), suggesting that NE signal dynamics (not just concentration) determine α ₁-AR engagement. Mechanistically, the sharp, transient nature of phasic NE may favor GPCR signaling toward the G-protein signaling, whereas the gradual rise of tonic NE could promote β -arrestin recruitment and receptor desensitization.¹¹⁰

Functional manipulation experiments revealed a dual role of LHB astrocytes in shaping NE dynamics: they not only induce

the second-phase phasic NE activity triggered by individual FS but also drive ramp-up of basal NE signals over repeated FS (Figures 5N and 5P). This is potentially mediated by astrocyte-dependent enhancement of presynaptic transmitter release.¹¹¹ It remains to be explored whether elevated basal NE activity contributes to depression-related pathophysiology and how astrocytes spatiotemporally orchestrate these NE dynamics. Further investigation into the functional significance and organizational principles of these temporally distinct NE signaling patterns will advance our understanding of stress-induced neuroadaptations.

Role of NE system in depression

The NE system is a key player in stress response and mood disorders, with dysfunction strongly linked to depression.^{73–75,103,112–114} The efficacy of SNRIs and NRIs in treating depression,^{115–117} along with evidence that NET knockout mice resist stress-induced depressive-like behavior,¹¹⁸ supports the prevailing hypothesis of NE deficiency in depression.^{104,119–121} Paradoxically, however, elevated NE levels in cerebrospinal fluid (CSF) and plasma of depressed patients^{122,123} increased LC neuron activity in depression models,^{124,125} and the antidepressant effects of reducing LC activity^{119,126–128} suggest instead an association between depression and the hyperactivity of the NE system.^{104,119–121}

This paradox may be explained by our current finding: while NE reuptake inhibitors increased tonic NE level, they actually blocked phasic NE release. Phasic NE release relies heavily on NETs for reuptake and vesicle recycling,^{109,129,130} which is disrupted by reuptake inhibitors. As shown in the current finding, the inhibition of phasic NE release may suppress α _{1A}-AR-dependent LHB-astrocytic calcium signaling, preventing stress-induced depression-like behaviors. Additionally, during depression, LHB neurons exhibit high-frequency bursting activity,^{17,18,131} which may engage the LHB-LC loop, triggering phasic NE release and activation of astrocytic Ca²⁺. Blockade of this loop may also be the mechanism by which NE reuptake blockers exert their antidepressant effects. Collectively, our study suggests that drugs targeting the NE system—such as the NE reuptake inhibitors, α _{1A}-AR inhibitors, or α ₂-AR agonists (Figure 3H)—may hold potential for the prevention and treatment of depression.

Limitations of the study

One limitation is that the biphasic calcium activity of LHB neurons was analyzed from bulk signals, preventing differentiation of whether the two phases involve the same or distinct subpopulations. Future studies should explore miniscope/endscope imaging in the LHB, though this remains technically challenging. Another limitation is the lack of experimental data explaining why LHB astrocytes respond most rapidly to stress. Although we discussed potential mechanisms, further investigation is needed to clarify the underlying processes.

RESOURCE AVAILABILITY

Lead contact

Requests for further information and resources should be directed to, and will be fulfilled by, the lead contact, Hailan Hu (huhailan@zju.edu.cn).

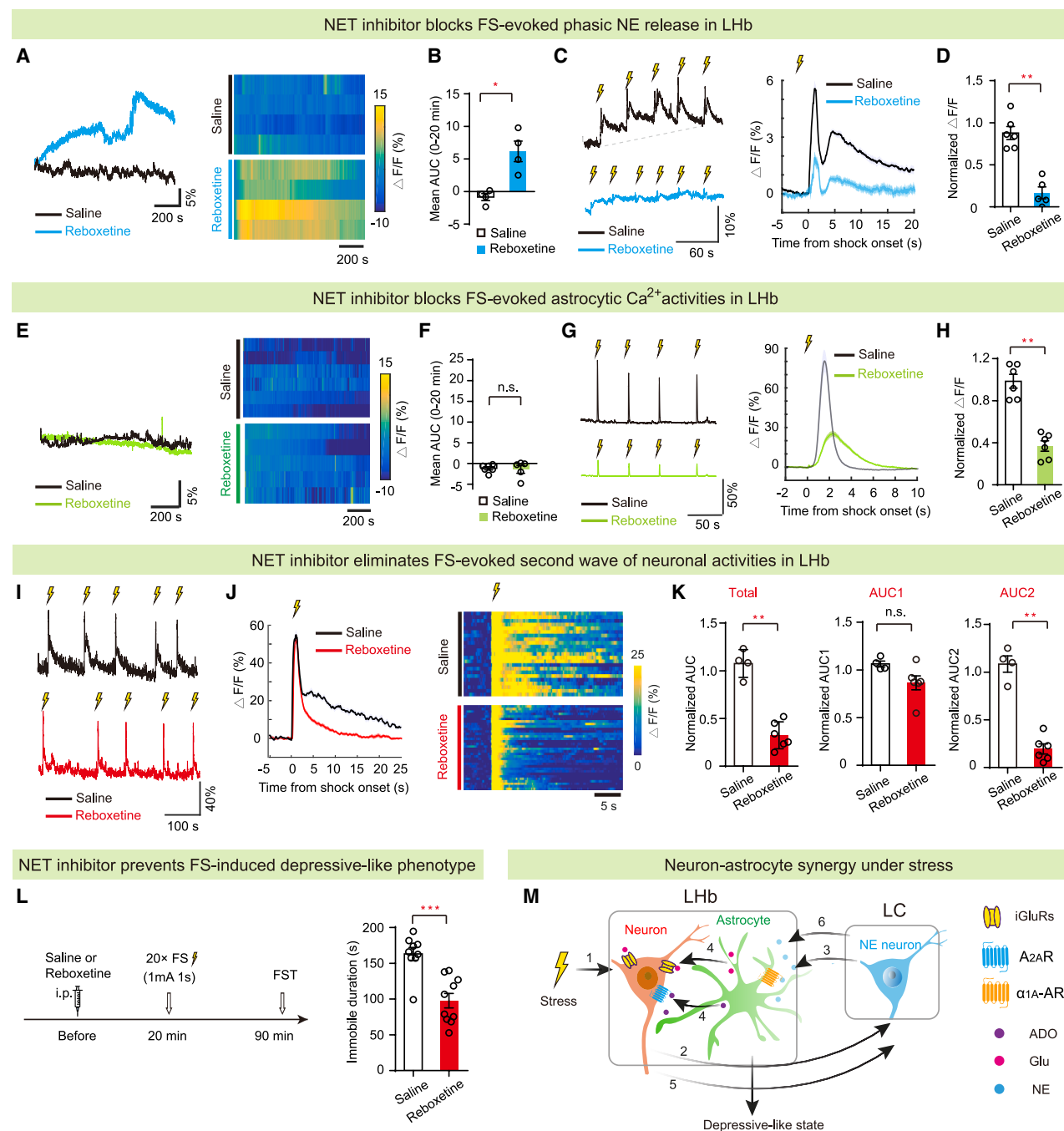


Figure 7. NE reuptake inhibitors block FS-evoked phasic NE release and astrocytic activity in LHB

(A and B) Representative raw traces (A, left), heatmaps (A, right), and bar graph (B) showing responses of LHB NE sensor following an i.p. injection of saline (black, $n = 4$ mice) or reboxetine (blue, 20 mg/kg, $n = 4$ mice) in home cage.

(C and D) Representative raw traces (C, left), plots of averaged $\Delta F/F$ ratio (C, right), and bar graph (D) showing responses of LHB NE sensor to FS following an i.p. injection of saline (black, $n = 6$ mice) or reboxetine (blue, 20 mg/kg, $n = 5$ mice).

(E and F) Representative raw traces (E, left), heatmaps (E, right), and bar graph (F) showing responses of LHB astrocytic calcium following an i.p. injection of saline (black, $n = 6$ mice) or reboxetine (green, 20 mg/kg, $n = 5$ mice) in home cage.

(G and H) Representative raw traces (G, left), plots of averaged $\Delta F/F$ ratio (G, right), and bar graph (H) showing responses of LHB astrocytic calcium to FS following an i.p. injection of saline (black, $n = 6$ mice) or reboxetine (green, 20 mg/kg, $n = 6$ mice).

(I) Representative raw traces showing responses of LHB neuronal calcium to FS following an i.p. injection of saline (black) or reboxetine (red, 20 mg/kg).

(J) Plots of averaged $\Delta F/F$ ratio (left) and heatmap (right) of LHB astrocytic calcium response to FS following an i.p. injection of saline (black) or reboxetine (red, 20 mg/kg).

(legend continued on next page)

Materials availability

This study did not generate new unique reagents.

Data and code availability

- All data reported in this paper will be shared by the [lead contact](#) upon request.
- All original code has been deposited at Zenodo at <https://zenodo.org/records/15087544> and is publicly available as of the date of publication
- Any additional information required to reanalyze the data reported in this paper is available from the [lead contact](#) upon request.

ACKNOWLEDGMENTS

We thank Yingzhuo Gou, Yang Xiong, Min Chen, Huafeng Zhang, Shiqi Wang, and colleagues from the Hu lab for assistance with experiments; Minmin Luo for providing the GfaABC₁D-cOpm5-mCherry virus; Xiaowei Chen and Kuan Zhang for gifting the GfaABC₁D-lck-GCaMP6f virus; Qin Han and Hangjun Wu for technical assistance with two-photon imaging; and Hui Li and Xiaoke Xie for advice on two-photon imaging. Some graphic components were created with BioRender. This work was supported by the ST12030-Major Projects (2021ZD0203000 and 2021ZD0203001), the National Natural Science Foundation of China (32130042, 82288101, and 31830032), the New Cornerstone Science Foundation to H.H., the Key R&D Program of Zhejiang (2024SSYS0016), the Fundamental Research Funds for the Central Universities (2025ZFJH01-01), the Non-profit Central Research Institute Fund of Chinese Academy of Medical Sciences (2023-PT310-01), and the Project for Hangzhou Medical Disciplines of Excellence and Key Project for Hangzhou Medical Disciplines to H.H.

AUTHOR CONTRIBUTIONS

Q.X., J.W., and J.Z. conducted the behavioral pharmacology experiments and the related behavioral analysis. Q.X. and J.W. performed the *in vivo* fiber photometry recording. J.W. and Q.X. performed the *in vitro* two-photon imaging. Q.X. performed immunohistochemistry experiments with the assistance of J.Z., Y.T., X.J., and Z.X. Z.N. assisted J.W. and Q.X. in analyzing two-photon imaging data. Y.L., J.F., and Z.W. shared the NE sensor and adenosine sensor. X.L. and H.M. contributed to experimental design and discussions. H.H., Q.X., and J.W. designed the study. H.H. supervised the project and wrote the manuscript with Q.X. and J.W.

DECLARATION OF INTERESTS

H.H. is a member of the advisory board of *Cell*.

DECLARATION OF GENERATIVE AI AND AI-ASSISTED TECHNOLOGIES IN THE WRITING PROCESS

The authors used ChatGPT and DeepSeek to check for grammar and style.

STAR★METHODS

Detailed methods are provided in the online version of this paper and include the following:

(K) Bar graph showing the effects of reboxetine on LHB neuronal calcium activities induced by FS ($n = 4, 6$ mice, saline vs. 20 mg/kg reboxetine).

(L) Reboxetine prevents FS-induced depressive-like behavior. Experimental paradigm (left). Depression-like behaviors in FST ($n = 9, 10$ mice, saline vs. reboxetine, right).

(M) LHB neuron-astrocyte synergy in depression. Stress first activates LHB neurons, which in turn recruit LC-NE neurons. NE release in LHB then triggers astrocytic Ca^{2+} through α_{1A} -AR-dependent signaling. In tandem, through gliotransmitters glutamate (Glu) and ATP/adenosine (Ado), LHB astrocytes prompt the second-phase of both local LHB neural activities and NE release. Through such a positive reinforcing loop, LHB astrocytes facilitate stress-induced depression-like behaviors.

* $p < 0.05$; ** $p < 0.01$; *** $p < 0.001$; **** $p < 0.0001$; n.s., not significant. Data are represented as mean \pm SEM.

See also [Figure S15](#).

- KEY RESOURCES TABLE
- EXPERIMENTAL MODEL AND STUDY PARTICIPANT DETAILS
 - Animals
- METHOD DETAILS
 - Surgery and viral injection
 - *In vivo* fiber photometry recording
 - Acute brain slice preparation for imaging
 - *In vitro* imaging
 - Immunohistochemistry
 - Behavioral assays
- QUANTIFICATION AND STATISTICAL ANALYSIS

SUPPLEMENTAL INFORMATION

Supplemental information can be found online at <https://doi.org/10.1016/j.cell.2025.04.010>.

Received: September 8, 2024

Revised: January 8, 2025

Accepted: April 3, 2025

Published: April 24, 2025

REFERENCES

1. Henn, F.A., and Vollmayr, B. (2005). Stress models of depression: forming genetically vulnerable strains. *Neurosci. Biobehav. Rev.* 29, 799–804. <https://doi.org/10.1016/j.neubiorev.2005.03.019>.
2. Duman, R.S., Nakagawa, S., and Malberg, J. (2001). Regulation of adult neurogenesis by antidepressant treatment. *Neuropsychopharmacology* 25, 836–844. [https://doi.org/10.1016/S0893-133X\(01\)00358-X](https://doi.org/10.1016/S0893-133X(01)00358-X).
3. Cathomas, F., Holt, L.M., Parise, E.M., Liu, J., Murrrough, J.W., Casaccia, P., Nestler, E.J., and Russo, S.J. (2022). Beyond the neuron: Role of non-neuronal cells in stress disorders. *Neuron* 110, 1116–1138. <https://doi.org/10.1016/j.neuron.2022.01.033>.
4. Proulx, C.D., Hikosaka, O., and Malinow, R. (2014). Reward processing by the lateral habenula in normal and depressive behaviors. *Nat. Neurosci.* 17, 1146–1152. <https://doi.org/10.1038/nn.3779>.
5. Hikosaka, O. (2010). The habenula: from stress evasion to value-based decision-making. *Nat. Rev. Neurosci.* 11, 503–513. <https://doi.org/10.1038/nrn2866>.
6. Hu, H., Cui, Y., and Yang, Y. (2020). Circuits and functions of the lateral habenula in health and in disease. *Nat. Rev. Neurosci.* 21, 277–295. <https://doi.org/10.1038/s41583-020-0292-4>.
7. Sutherland, R.J. (1982). The dorsal diencephalic conduction system: a review of the anatomy and functions of the habenular complex. *Neurosci. Biobehav. Rev.* 6, 1–13. [https://doi.org/10.1016/0149-7634\(82\)90003-3](https://doi.org/10.1016/0149-7634(82)90003-3).
8. Namboodiri, V.M.K., Rodríguez-Romaguera, J., and Stuber, G.D. (2016). The habenula. *Curr. Biol.* 26, R873–R877. <https://doi.org/10.1016/j.cub.2016.08.051>.
9. Andalman, A.S., Burns, V.M., Lovett-Barron, M., Broxton, M., Poole, B., Yang, S.J., Grosenick, L., Lerner, T.N., Chen, R., Benster, T., et al. (2019). Neuronal Dynamics Regulating Brain and Behavioral State Transitions. *Cell* 177, 970–985.e20. <https://doi.org/10.1016/j.cell.2019.02.037>.

10. Shabel, S.J., Wang, C., Monk, B., Aronson, S., and Malinow, R. (2019). Stress transforms lateral habenula reward responses into punishment signals. *Proc. Natl. Acad. Sci. USA* 116, 12488–12493. <https://doi.org/10.1073/pnas.1903334116>.
11. Lecca, S., Meye, F.J., Trusel, M., Tchenio, A., Harris, J., Schwarz, M.K., Burdakov, D., Georges, F., and Mameli, M. (2017). Aversive stimuli drive hypothalamus-to-habenula excitation to promote escape behavior. *eLife* 6, e30697. <https://doi.org/10.7554/eLife.30697>.
12. Fan, Z., Chang, J., Liang, Y., Zhu, H., Zhang, C., Zheng, D., Wang, J., Xu, Y., Li, Q.J., and Hu, H. (2023). Neural mechanism underlying depressive-like state associated with social status loss. *Cell* 186, 560–576.e17. <https://doi.org/10.1016/j.cell.2022.12.033>.
13. Morris, J.S., Smith, K.A., Cowen, P.J., Friston, K.J., and Dolan, R.J. (1999). Covariation of activity in habenula and dorsal raphe nuclei following tryptophan depletion. *Neuroimage* 10, 163–172. <https://doi.org/10.1006/nimg.1999.0455>.
14. Li, B., Piriz, J., Mirrione, M., Chung, C., Proulx, C.D., Schulz, D., Henn, F., and Malinow, R. (2011). Synaptic potentiation onto habenula neurons in the learned helplessness model of depression. *Nature* 470, 535–539. <https://doi.org/10.1038/nature09742>.
15. Lecca, S., Pelosi, A., Tchenio, A., Moutkine, I., Lujan, R., Hervé, D., and Mameli, M. (2016). Rescue of GABAB and GIRK function in the lateral habenula by protein phosphatase 2A inhibition ameliorates depression-like phenotypes in mice. *Nat. Med.* 22, 254–261. <https://doi.org/10.1038/nm.4037>.
16. Cerniauskas, I., Winterer, J., de Jong, J.W., Lukacsovich, D., Yang, H., Khan, F., Peck, J.R., Obayashi, S.K., Lilascharoen, V., Lim, B.K., et al. (2019). Chronic Stress Induces Activity, Synaptic, and Transcriptional Remodeling of the Lateral Habenula Associated with Deficits in Motivated Behaviors. *Neuron* 104, 899–915.e8. <https://doi.org/10.1016/j.neuron.2019.09.005>.
17. Yang, Y., Cui, Y., Sang, K., Dong, Y., Ni, Z., Ma, S., and Hu, H. (2018). Ketamine blocks bursting in the lateral habenula to rapidly relieve depression. *Nature* 554, 317–322. <https://doi.org/10.1038/nature25509>.
18. Chen, M., Ma, S., Liu, H., Dong, Y., Tang, J., Ni, Z., Tan, Y., Duan, C., Li, H., Huang, H., et al. (2024). Brain region-specific action of ketamine as a rapid antidepressant. *Science* 385, eado7010. <https://doi.org/10.1126/science.ado7010>.
19. Cui, Y., Yang, Y., Ni, Z., Dong, Y., Cai, G., Foncelle, A., Ma, S., Sang, K., Tang, S., Li, Y., et al. (2018). Astroglial Kir4.1 in the lateral habenula drives neuronal bursts in depression. *Nature* 554, 323–327. <https://doi.org/10.1038/nature25752>.
20. Cui, W., Mizukami, H., Yanagisawa, M., Aida, T., Nomura, M., Isomura, Y., Takayanagi, R., Ozawa, K., Tanaka, K., and Aizawa, H. (2014). Glial dysfunction in the mouse habenula causes depressive-like behaviors and sleep disturbance. *J. Neurosci.* 34, 16273–16285. <https://doi.org/10.1523/JNEUROSCI.1465-14.2014>.
21. Kang, S., Li, J., Bekker, A., and Ye, J.H. (2018). Rescue of glutamate transport in the lateral habenula alleviates depression- and anxiety-like behaviors in ethanol-withdrawn rats. *Neuropharmacology* 129, 47–56. <https://doi.org/10.1016/j.neuropharm.2017.11.013>.
22. Allen, N.J., and Eroglu, C. (2017). Cell Biology of Astrocyte-Synapse Interactions. *Neuron* 96, 697–708. <https://doi.org/10.1016/j.neuron.2017.09.056>.
23. Kofuji, P., and Araque, A. (2021). Astrocytes and Behavior. *Annu. Rev. Neurosci.* 44, 49–67. <https://doi.org/10.1146/annurev-neuro-101920-112225>.
24. Koh, W., Kwak, H., Cheong, E., and Lee, C.J. (2023). GABA tone regulation and its cognitive functions in the brain. *Nat. Rev. Neurosci.* 24, 523–539. <https://doi.org/10.1038/s41583-023-00724-7>.
25. Nagai, J., Yu, X., Papouin, T., Cheong, E., Freeman, M.R., Monk, K.R., Hastings, M.H., Haydon, P.G., Rowitch, D., Shaham, S., et al. (2021). Behaviorally consequential astrocytic regulation of neural circuits. *Neuron* 109, 576–596. <https://doi.org/10.1016/j.neuron.2020.12.008>.
26. Williamson, M.R., Kwon, W., Woo, J., Ko, Y., Maleki, E., Yu, K., Murali, S., Sardar, D., and Deneen, B. (2025). Learning-associated astrocyte ensembles regulate memory recall. *Nature* 637, 478–486. <https://doi.org/10.1038/s41586-024-08170-w>.
27. Sun, W., Liu, Z., Jiang, X., Chen, M.B., Dong, H., Liu, J., Südhof, T.C., and Quake, S.R. (2024). Spatial transcriptomics reveal neuron-astrocyte synergy in long-term memory. *Nature* 627, 374–381. <https://doi.org/10.1038/s41586-023-07011-6>.
28. Lee, H.G., Wheeler, M.A., and Quintana, F.J. (2022). Function and therapeutic value of astrocytes in neurological diseases. *Nat. Rev. Drug Discov.* 21, 339–358. <https://doi.org/10.1038/s41573-022-00390-x>.
29. Agulhon, C., Petravic, J., McMullen, A.B., Sweger, E.J., Minton, S.K., Taves, S.R., Casper, K.B., Fiocco, T.A., and McCarthy, K.D. (2008). What is the role of astrocyte calcium in neurophysiology? *Neuron* 59, 932–946. <https://doi.org/10.1016/j.neuron.2008.09.004>.
30. Theparambil, S.M., Kopach, O., Braga, A., Nizari, S., Hosford, P.S., Sagi-Kiss, V., Hadjihambi, A., Konstantinou, C., Esteras, N., Gutierrez Del Arroyo, A., et al. (2024). Adenosine signalling to astrocytes coordinates brain metabolism and function. *Nature* 632, 139–146. <https://doi.org/10.1038/s41586-024-07611-w>.
31. Nagai, J., Rajbhandari, A.K., Gangwani, M.R., Hachisuka, A., Coppola, G., Masmanidis, S.C., Fanselow, M.S., and Khakh, B.S. (2019). Hyperactivity with Disrupted Attention by Activation of an Astrocyte Synaptogenic Cue. *Cell* 177, 1280–1292.e20. <https://doi.org/10.1016/j.cell.2019.03.019>.
32. Cornell-Bell, A.H., Finkbeiner, S.M., Cooper, M.S., and Smith, S.J. (1990). Glutamate induces calcium waves in cultured astrocytes: long-range glial signaling. *Science* 247, 470–473. <https://doi.org/10.1126/science.1967852>.
33. Corkrum, M., Covelio, A., Lines, J., Bellocchio, L., Pisansky, M., Loke, K., Quintana, R., Rothwell, P.E., Lujan, R., Marsicano, G., et al. (2020). Dopamine-Evoked Synaptic Regulation in the Nucleus Accumbens Requires Astrocyte Activity. *Neuron* 105, 1036–1047.e5. <https://doi.org/10.1016/j.neuron.2019.12.026>.
34. Tewari, B.P., Woo, A.M., Prim, C.E., Chaunsali, L., Patel, D.C., Kimbrough, I.F., Engel, K., Browning, J.L., Campbell, S.L., and Sontheimer, H. (2024). Astrocytes require perineuronal nets to maintain synaptic homeostasis in mice. *Nat. Neurosci.* 27, 1475–1488. <https://doi.org/10.1038/s41593-024-01714-3>.
35. Semyanov, A., Henneberger, C., and Agarwal, A. (2020). Making sense of astrocytic calcium signals - from acquisition to interpretation. *Nat. Rev. Neurosci.* 21, 551–564. <https://doi.org/10.1038/s41583-020-0361-8>.
36. Cahill, M.K., Collard, M., Tse, V., Reitman, M.E., Etchenique, R., Kirst, C., and Poskanzer, K.E. (2024). Network-level encoding of local neurotransmitters in cortical astrocytes. *Nature* 629, 146–153. <https://doi.org/10.1038/s41586-024-07311-5>.
37. Sharma, G., and Vijayaraghavan, S. (2001). Nicotinic cholinergic signaling in hippocampal astrocytes involves calcium-induced calcium release from intracellular stores. *Proc. Natl. Acad. Sci. USA* 98, 4148–4153. <https://doi.org/10.1073/pnas.071540198>.
38. Araque, A., Martín, E.D., Perea, G., Arellano, J.I., and Buño, W. (2002). Synaptically released acetylcholine evokes Ca²⁺ elevations in astrocytes in hippocampal slices. *J. Neurosci.* 22, 2443–2450. <https://doi.org/10.1523/JNEUROSCI.22-07-02443.2002>.
39. Papouin, T., Dunphy, J.M., Tolman, M., Dineley, K.T., and Haydon, P.G. (2017). Septal Cholinergic Neuromodulation Tunes the Astrocyte-Dependent Gating of Hippocampal NMDA Receptors to Wakefulness. *Neuron* 94, 840–854.e7. <https://doi.org/10.1016/j.neuron.2017.04.021>.
40. Zhang, K., Förster, R., He, W., Liao, X., Li, J., Yang, C., Qin, H., Wang, M., Ding, R., Li, R., et al. (2021). Fear learning induces $\alpha 7$ -nicotinic acetylcholine receptor-mediated astrocytic responsiveness that is required for

- memory persistence. *Nat. Neurosci.* 24, 1686–1698. <https://doi.org/10.1038/s41593-021-00949-8>.
41. Requeie, L.M., Gómez-Gonzalo, M., Speggorin, M., Managò, F., Melone, M., Congiu, M., Chiavegato, A., Lia, A., Zonta, M., Losi, G., et al. (2022). Astrocytes mediate long-lasting synaptic regulation of ventral tegmental area dopamine neurons. *Nat. Neurosci.* 25, 1639–1650. <https://doi.org/10.1038/s41593-022-01193-4>.
42. González-Arias, C., Sánchez-Ruiz, A., Esparza, J., Sánchez-Puelles, C., Arancibia, L., Ramírez-Franco, J., Gobbo, D., Kirchhoff, F., and Perea, G. (2023). Dysfunctional serotonergic neuron-astrocyte signaling in depressive-like states. *Mol. Psychiatry* 28, 3856–3873. <https://doi.org/10.1038/s41380-023-02269-8>.
43. Bekar, L.K., He, W., and Nedergaard, M. (2008). Locus coeruleus alpha-adrenergic-mediated activation of cortical astrocytes in vivo. *Cereb. Cortex* 18, 2789–2795. <https://doi.org/10.1093/cercor/bhn040>.
44. Paukert, M., Agarwal, A., Cha, J., Doze, V.A., Kang, J.U., and Bergles, D. E. (2014). Norepinephrine controls astroglial responsiveness to local circuit activity. *Neuron* 82, 1263–1270. <https://doi.org/10.1016/j.neuron.2014.04.038>.
45. Mu, Y., Bennett, D.V., Rubinov, M., Narayan, S., Yang, C.T., Tanimoto, M., Mensh, B.D., Looger, L.L., and Ahrens, M.B. (2019). Glia Accumulate Evidence that Actions Are Futile and Suppress Unsuccessful Behavior. *Cell* 178, 27–43.e19. <https://doi.org/10.1016/j.cell.2019.05.050>.
46. Duque, M., Chen, A.B., Hsu, E., Narayan, S., Rymbek, A., Begum, S., Saher, G., Cohen, A.E., Olson, D.E., Li, Y., et al. (2025). Ketamine induces plasticity in a norepinephrine-astroglial circuit to promote behavioral perseverance. *Neuron* 113, 426–443.e5. <https://doi.org/10.1016/j.neuron.2024.11.011>.
47. Pannasch, U., Freche, D., Dallérac, G., Ghézali, G., Escartin, C., Ezan, P., Cohen-Salmon, M., Benchenane, K., Abudara, V., Dufour, A., et al. (2014). Connexin 30 sets synaptic strength by controlling astroglial synapse invasion. *Nat. Neurosci.* 17, 549–558. <https://doi.org/10.1038/nn.3662>.
48. Muthukumar, A.K., Stork, T., and Freeman, M.R. (2014). Activity-dependent regulation of astrocyte GAT levels during synaptogenesis. *Nat. Neurosci.* 17, 1340–1350. <https://doi.org/10.1038/nn.3791>.
49. Verkhatsky, A., Untiet, V., and Rose, C.R. (2020). Ionic signalling in astroglia beyond calcium. *J. Physiol.* 598, 1655–1670. <https://doi.org/10.1113/JP277478>.
50. Scemes, E., and Giaume, C. (2006). Astrocyte calcium waves: what they are and what they do. *Glia* 54, 716–725. <https://doi.org/10.1002/glia.20374>.
51. Araque, A., Carmignoto, G., Haydon, P.G., Oliet, S.H.R., Robitaille, R., and Volterra, A. (2014). Gliotransmitters travel in time and space. *Neuron* 81, 728–739. <https://doi.org/10.1016/j.neuron.2014.02.007>.
52. Bazargani, N., and Attwell, D. (2016). Astrocyte calcium signaling: the third wave. *Nat. Neurosci.* 19, 182–189. <https://doi.org/10.1038/nn.4201>.
53. Volterra, A., Liaudet, N., and Savtchouk, I. (2014). Astrocyte Ca²⁺ signaling: an unexpected complexity. *Nat. Rev. Neurosci.* 15, 327–335. <https://doi.org/10.1038/nrn3725>.
54. Nedergaard, M. (1994). Direct signaling from astrocytes to neurons in cultures of mammalian brain cells. *Science* 263, 1768–1771. <https://doi.org/10.1126/science.8134839>.
55. Ma, Z., Stork, T., Bergles, D.E., and Freeman, M.R. (2016). Neuromodulators signal through astrocytes to alter neural circuit activity and behaviour. *Nature* 539, 428–432. <https://doi.org/10.1038/nature20145>.
56. Fellin, T., Pascual, O., Gobbo, S., Pozzan, T., Haydon, P.G., and Carmignoto, G. (2004). Neuronal synchrony mediated by astrocytic glutamate through activation of extrasynaptic NMDA receptors. *Neuron* 43, 729–743. <https://doi.org/10.1016/j.neuron.2004.08.011>.
57. Pirttimäki, T.M., Sims, R.E., Saunders, G., Antonio, S.A., Codadu, N.K., and Parri, H.R. (2017). Astrocyte-Mediated Neuronal Synchronization Properties Revealed by False Gliotransmitter Release. *J. Neurosci.* 37, 9859–9870. <https://doi.org/10.1523/JNEUROSCI.2761-16.2017>.
58. Kwak, H., Koh, W., Kim, S., Song, K., Shin, J.I., Lee, J.M., Lee, E.H., Bae, J.Y., Ha, G.E., Oh, J.E., et al. (2020). Astrocytes Control Sensory Acuity via Tonic Inhibition in the Thalamus. *Neuron* 108, 691–706.e10. <https://doi.org/10.1016/j.neuron.2020.08.013>.
59. Zhang, J.M., Wang, H.K., Ye, C.Q., Ge, W., Chen, Y., Jiang, Z.L., Wu, C. P., Poo, M.M., and Duan, S. (2003). ATP released by astrocytes mediates glutamatergic activity-dependent heterosynaptic suppression. *Neuron* 40, 971–982. [https://doi.org/10.1016/s0896-6273\(03\)00717-7](https://doi.org/10.1016/s0896-6273(03)00717-7).
60. Adamsky, A., Kol, A., Kreisel, T., Doron, A., Ozeri-Engelhard, N., Melcer, T., Refaeli, R., Horn, H., Regev, L., Groysman, M., et al. (2018). Astrocytic Activation Generates De Novo Neuronal Potentiation and Memory Enhancement. *Cell* 174, 59–71.e14. <https://doi.org/10.1016/j.cell.2018.05.002>.
61. Dallérac, G., Zapata, J., and Rouach, N. (2018). Versatile control of synaptic circuits by astrocytes: where, when and how? *Nat. Rev. Neurosci.* 19, 729–743. <https://doi.org/10.1038/s41583-018-0080-6>.
62. Noh, K., Cho, W.H., Lee, B.H., Kim, D.W., Kim, Y.S., Park, K., Hwang, M., Barcelon, E., Cho, Y.K., Lee, C.J., et al. (2023). Cortical astrocytes modulate dominance behavior in male mice by regulating synaptic excitatory and inhibitory balance. *Nat. Neurosci.* 26, 1541–1554. <https://doi.org/10.1038/s41593-023-01406-4>.
63. Gordon, G.R.J., Baimoukhametova, D.V., Hewitt, S.A., Rajapaksha, W.R. A.K.J.S., Fisher, T.E., and Bains, J.S. (2005). Norepinephrine triggers release of glial ATP to increase postsynaptic efficacy. *Nat. Neurosci.* 8, 1078–1086. <https://doi.org/10.1038/nn1498>.
64. Shigetomi, E., Bushong, E.A., Haustein, M.D., Tong, X., Jackson-Weaver, O., Kracun, S., Xu, J., Sofroniew, M.V., Ellisman, M.H., and Khakh, B.S. (2013). Imaging calcium microdomains within entire astrocyte territories and endfeet with GCaMPs expressed using adeno-associated viruses. *J. Gen. Physiol.* 141, 633–647. <https://doi.org/10.1085/jgp.201210949>.
65. Chen, T.W., Wardill, T.J., Sun, Y., Pulver, S.R., Renninger, S.L., Baohan, A., Schreiter, E.R., Kerr, R.A., Orger, M.B., Jayaraman, V., et al. (2013). Ultrasensitive fluorescent proteins for imaging neuronal activity. *Nature* 499, 295–300. <https://doi.org/10.1038/nature12354>.
66. Dana, H., Mohar, B., Sun, Y., Narayan, S., Gordus, A., Hasseman, J.P., Tsegaye, G., Holt, G.T., Hu, A., Walpita, D., et al. (2016). Sensitive red protein calcium indicators for imaging neural activity. *eLife* 5, e12727. <https://doi.org/10.7554/eLife.12727>.
67. Kellner, V., Kersbergen, C.J., Li, S., Babola, T.A., Saher, G., and Bergles, D.E. (2021). Dual metabotropic glutamate receptor signaling enables coordination of astrocyte and neuron activity in developing sensory domains. *Neuron* 109, 2545–2555.e7. <https://doi.org/10.1016/j.neuron.2021.06.010>.
68. Takata, N., Mishima, T., Hisatsune, C., Nagai, T., Ebisui, E., Mikoshiba, K., and Hirase, H. (2011). Astrocyte calcium signaling transforms cholinergic modulation to cortical plasticity in vivo. *J. Neurosci.* 31, 18155–18165. <https://doi.org/10.1523/JNEUROSCI.5289-11.2011>.
69. Reitman, M.E., Tse, V., Mi, X., Willoughby, D.D., Peinado, A., Avizaidis, A., Myagmar, B.E., Simpson, P.C., Bayraktar, O.A., Yu, G., et al. (2023). Norepinephrine links astrocytic activity to regulation of cortical state. *Nat. Neurosci.* 26, 579–593. <https://doi.org/10.1038/s41593-023-01284-w>.
70. Rupperecht, P., Duss, S.N., Becker, D., Lewis, C.M., Bohacek, J., and Helmchen, F. (2024). Centripetal integration of past events in hippocampal astrocytes regulated by locus coeruleus. *Nat. Neurosci.* 27, 927–939. <https://doi.org/10.1038/s41593-024-01612-8>.
71. Wang, B., Wang, Y., Wu, Q., Huang, H.P., and Li, S. (2017). Effects of alpha2A Adrenoceptors on Norepinephrine Secretion from the Locus Coeruleus during Chronic Stress-Induced Depression. *Front. Neurosci.* 11, 243. <https://doi.org/10.3389/fnins.2017.00243>.

72. Feng, J., Dong, H., Lischinsky, J.E., Zhou, J., Deng, F., Zhuang, C., Miao, X., Wang, H., Li, G., Cai, R., et al. (2024). Monitoring norepinephrine release in vivo using next-generation GRAB_{NE} sensors. *Neuron* 112, 1930–1942.e6. <https://doi.org/10.1016/j.neuron.2024.03.001>.
73. Berridge, C.W., and Waterhouse, B.D. (2003). The locus coeruleus-noradrenergic system: modulation of behavioral state and state-dependent cognitive processes. *Brain Res. Brain Res. Rev.* 42, 33–84. [https://doi.org/10.1016/s0165-0173\(03\)00143-7](https://doi.org/10.1016/s0165-0173(03)00143-7).
74. Sara, S.J. (2009). The locus coeruleus and noradrenergic modulation of cognition. *Nat. Rev. Neurosci.* 10, 211–223. <https://doi.org/10.1038/nrn2573>.
75. Jordan, R. (2024). The locus coeruleus as a global model failure system. *Trends Neurosci.* 47, 92–105. <https://doi.org/10.1016/j.tins.2023.11.006>.
76. Graham, R.M., Perez, D.M., Hwa, J., and Piascik, M.T. (1996). alpha 1-adrenergic receptor subtypes. Molecular structure, function, and signaling. *Circ. Res.* 78, 737–749. <https://doi.org/10.1161/01.res.78.5.737>.
77. Dai, R., Yu, T., Weng, D., Li, H., Cui, Y., Wu, Z., Guo, Q., Zou, H., Wu, W., Gao, X., et al. (2022). A neuropsin-based optogenetic tool for precise control of G_q signaling. *Sci. China Life Sci.* 65, 1271–1284. <https://doi.org/10.1007/s11427-022-2122-0>.
78. de Ceglia, R., Ledonne, A., Litvin, D.G., Lind, B.L., Carriero, G., Latagliata, E.C., Bindocci, E., Di Castro, M.A., Savtchouk, I., Vitali, I., et al. (2023). Specialized astrocytes mediate glutamatergic gliotransmission in the CNS. *Nature* 622, 120–129. <https://doi.org/10.1038/s41586-023-06502-w>.
79. Woo, D.H., Han, K.S., Shim, J.W., Yoon, B.E., Kim, E., Bae, J.Y., Oh, S.J., Hwang, E.M., Marmorstein, A.D., Bae, Y.C., et al. (2012). TREK-1 and Best1 channels mediate fast and slow glutamate release in astrocytes upon GPCR activation. *Cell* 151, 25–40. <https://doi.org/10.1016/j.cell.2012.09.005>.
80. Parpura, V., Basarsky, T.A., Liu, F., Jeftinija, K., Jeftinija, S., and Haydon, P.G. (1994). Glutamate-mediated astrocyte-neuron signalling. *Nature* 369, 744–747. <https://doi.org/10.1038/369744a0>.
81. Cheng, Y.T., Woo, J., Luna-Figueroa, E., Maleki, E., Harmanci, A.S., and Deneen, B. (2023). Social deprivation induces astrocytic TRPA1-GABA suppression of hippocampal circuits. *Neuron* 111, 1301–1315.e5. <https://doi.org/10.1016/j.neuron.2023.01.015>.
82. Lee, S., Yoon, B.E., Berglund, K., Oh, S.J., Park, H., Shin, H.S., Augustine, G.J., and Lee, C.J. (2010). Channel-mediated tonic GABA release from glia. *Science* 330, 790–796. <https://doi.org/10.1126/science.1184334>.
83. Duan, D., Zhang, H., Yue, X., Fan, Y., Xue, Y., Shao, J., Ding, G., Chen, D., Li, S., Cheng, H., et al. (2020). Sensory Glia Detect Repulsive Odorants and Drive Olfactory Adaptation. *Neuron* 108, 707–721.e8. <https://doi.org/10.1016/j.neuron.2020.08.026>.
84. Lezmy, J., Arancibia-Cárcamo, I.L., Quintela-López, T., Sherman, D.L., Brophy, P.J., and Attwell, D. (2021). Astrocyte Ca²⁺-evoked ATP release regulates myelinated axon excitability and conduction speed. *Science* 374, eabh2858. <https://doi.org/10.1126/science.abh2858>.
85. Cao, X., Li, L.P., Wang, Q., Wu, Q., Hu, H.H., Zhang, M., Fang, Y.Y., Zhang, J., Li, S.J., Xiong, W.C., et al. (2013). Astrocyte-derived ATP modulates depressive-like behaviors. *Nat. Med.* 19, 773–777. <https://doi.org/10.1038/nm.3162>.
86. Lefton, K.B., Wu, Y., Yen, A., Okuda, T., Zhang, Y., Dai, Y., Walsh, S., Manno, R., Dougherty, J.D., Samineni, V.K., et al. (2024). Norepinephrine Signals Through Astrocytes To Modulate Synapses. Preprint at bioRxiv. <https://doi.org/10.1101/2024.05.21.595135>.
87. Chen, A.B., Duque, M., Wang, V.M., Dhanasekar, M., Mi, X., Rymbek, A., Tocquer, L., Narayan, S., Prober, D., Yu, G., et al. (2024). Norepinephrine changes behavioral state via astroglial purinergic signaling. Preprint at bioRxiv. <https://doi.org/10.1101/2024.05.23.595576>.
88. Peng, W., Wu, Z., Song, K., Zhang, S., Li, Y., and Xu, M. (2020). Regulation of sleep homeostasis mediator adenosine by basal forebrain glutamatergic neurons. *Science* 369, eabb0556. <https://doi.org/10.1126/science.abb0556>.
89. Marvin, J.S., Scholl, B., Wilson, D.E., Podgorski, K., Kazemipour, A., Müller, J.A., Schoch, S., Quiroz, F.J.U., Rebola, N., Bao, H., et al. (2018). Stability, affinity, and chromatic variants of the glutamate sensor iGluSnFR. *Nat. Methods* 15, 936–939. <https://doi.org/10.1038/s41592-018-0171-3>.
90. Bosanac, I., Michikawa, T., Mikoshiba, K., and Ikura, M. (2004). Structural insights into the regulatory mechanism of IP3 receptor. *Biochim. Biophys. Acta* 1742, 89–102. <https://doi.org/10.1016/j.bbamcr.2004.09.016>.
91. Wang, Q., Kong, Y., Wu, D.Y., Liu, J.H., Jie, W., You, Q.L., Huang, L., Hu, J., Chu, H.D., Gao, F., et al. (2021). Impaired calcium signaling in astrocytes modulates autism spectrum disorder-like behaviors in mice. *Nat. Commun.* 12, 3321. <https://doi.org/10.1038/s41467-021-23843-0>.
92. Nagai, J., Bellafard, A., Qu, Z., Yu, X., Ollivier, M., Gangwani, M.R., Diaz-Castro, B., Coppola, G., Schumacher, S.M., Golshani, P., et al. (2021). Specific and behaviorally consequential astrocyte G_q GPCR signaling attenuation in vivo with ibetaARK. *Neuron* 109, 2256–2274.e9. <https://doi.org/10.1016/j.neuron.2021.05.023>.
93. Stamatakis, A.M., and Stuber, G.D. (2012). Activation of lateral habenula inputs to the ventral midbrain promotes behavioral avoidance. *Nat. Neurosci.* 15, 1105–1107. <https://doi.org/10.1038/nn.3145>.
94. Bymaster, F.P., Dreshfield-Ahmad, L.J., Threlkeld, P.G., Shaw, J.L., Thompson, L., Nelson, D.L., Hemrick-Luecke, S.K., and Wong, D.T. (2001). Comparative affinity of duloxetine and venlafaxine for serotonin and norepinephrine transporters in vitro and in vivo, human serotonin receptor subtypes, and other neuronal receptors. *Neuropsychopharmacology* 25, 871–880. [https://doi.org/10.1016/S0893-133X\(01\)00298-6](https://doi.org/10.1016/S0893-133X(01)00298-6).
95. Sacchetti, G., Bernini, M., Bianchetti, A., Parini, S., Invernizzi, R.W., and Samanin, R. (1999). Studies on the acute and chronic effects of reboxetine on extracellular noradrenaline and other monoamines in the rat brain. *Br. J. Pharmacol.* 128, 1332–1338. <https://doi.org/10.1038/sj.bjp.0702926>.
96. Major, G., and Tank, D. (2004). Persistent neural activity: prevalence and mechanisms. *Curr. Opin. Neurobiol.* 14, 675–684. <https://doi.org/10.1016/j.conb.2004.10.017>.
97. Kennedy, A., Kunwar, P.S., Li, L.Y., Stagkourakis, S., Wagenaar, D.A., and Anderson, D.J. (2020). Stimulus-specific hypothalamic encoding of a persistent defensive state. *Nature* 586, 730–734. <https://doi.org/10.1038/s41586-020-2728-4>.
98. Li, K., Zhou, T., Liao, L., Yang, Z., Wong, C., Henn, F., Malinow, R., Yates, J.R., 3rd, and Hu, H. (2013). βCaMKII in lateral habenula mediates core symptoms of depression. *Science* 341, 1016–1020. <https://doi.org/10.1126/science.1240729>.
99. Zhang, J., Lv, S., Tang, G., Bian, G., Yang, Y., Li, R., Yang, J., and Liu, J. (2019). Activation of calcium-impermeable GluR2-containing AMPA receptors in the lateral habenula produces antidepressant-like effects in a rodent model of Parkinson's disease. *Exp. Neurol.* 322, 113058. <https://doi.org/10.1016/j.expneurol.2019.113058>.
100. Cao, X.Z., Zhu, M.Y., Xu, G., Li, F., Yan, Y., Zhang, J.J., Wang, J., Zeng, F., Bao, Y., Zhang, X.X., et al. (2024). HCN channels in the lateral habenula regulate pain and comorbid depressive-like behaviors in mice. *CNS Neurosci. Ther.* 30, e14831. <https://doi.org/10.1111/cns.14831>.
101. Zhang, M., Vollmer, C., and Nurse, C.A. (2018). Adenosine and dopamine oppositely modulate a hyperpolarization-activated current I_h in chemosensory neurons of the rat carotid body in co-culture. *J. Physiol.* 596, 3101–3117. <https://doi.org/10.1113/JP274743>.
102. Lee, S.H., Kim, W.T., Cornell-Bell, A.H., and Sontheimer, H. (1994). Astrocytes exhibit regional specificity in gap-junction coupling. *Glia* 11, 315–325. <https://doi.org/10.1002/glia.440110404>.

103. Schwarz, L.A., Miyamichi, K., Gao, X.J., Beier, K.T., Weissbourd, B., DeLoach, K.E., Ren, J., Ibanes, S., Malenka, R.C., Kremer, E.J., et al. (2015). Viral-genetic tracing of the input-output organization of a central noradrenergic circuit. *Nature* 524, 88–92. <https://doi.org/10.1038/nature14600>.
104. Poe, G.R., Foote, S., Eschenko, O., Johansen, J.P., Bouret, S., Aston-Jones, G., Harley, C.W., Manahan-Vaughan, D., Weinschenker, D., Valentino, R., et al. (2020). Locus coeruleus: a new look at the blue spot. *Nat. Rev. Neurosci.* 21, 644–659. <https://doi.org/10.1038/s41583-020-0360-9>.
105. Liu, C., Goel, P., and Kaeser, P.S. (2021). Spatial and temporal scales of dopamine transmission. *Nat. Rev. Neurosci.* 22, 345–358. <https://doi.org/10.1038/s41583-021-00455-7>.
106. Aston-Jones, G., and Cohen, J.D. (2005). An integrative theory of locus coeruleus-norepinephrine function: adaptive gain and optimal performance. *Annu. Rev. Neurosci.* 28, 403–450. <https://doi.org/10.1146/annurev.neuro.28.061604.135709>.
107. Cai, X., Liu, C., Tsutsui-Kimura, I., Lee, J.H., Guo, C., Banerjee, A., Lee, J., Amo, R., Xie, Y., Patriarchi, T., et al. (2024). Dopamine dynamics are dispensable for movement but promote reward responses. *Nature* 635, 406–414. <https://doi.org/10.1038/s41586-024-08038-z>.
108. Kim, H.R., Malik, A.N., Mikhael, J.G., Bech, P., Tsutsui-Kimura, I., Sun, F., Zhang, Y., Li, Y., Watabe-Uchida, M., Gershman, S.J., et al. (2020). A Unified Framework for Dopamine Signals across Timescales. *Cell* 183, 1600–1616.e25. <https://doi.org/10.1016/j.cell.2020.11.013>.
109. Li, L., Rana, A.N., Li, E.M., Feng, J., Li, Y., and Bruchas, M.R. (2023). Activity-dependent constraints on catecholamine signaling. *Cell Rep.* 42, 113566. <https://doi.org/10.1016/j.celrep.2023.113566>.
110. Grundmann, M., and Kostenis, E. (2017). Temporal Bias: Time-Encoded Dynamic GPCR Signaling. *Trends Pharmacol. Sci.* 38, 1110–1124. <https://doi.org/10.1016/j.tips.2017.09.004>.
111. Martín, E.D., Fernández, M., Perea, G., Pascual, O., Haydon, P.G., Araque, A., and Ceña, V. (2007). Adenosine released by astrocytes contributes to hypoxia-induced modulation of synaptic transmission. *Glia* 55, 36–45. <https://doi.org/10.1002/glia.20431>.
112. Chrousos, G.P. (2009). Stress and disorders of the stress system. *Nat. Rev. Endocrinol.* 5, 374–381. <https://doi.org/10.1038/nrendo.2009.106>.
113. Strawn, J.R., and Geraciotti, T.D., Jr. (2008). Noradrenergic dysfunction and the psychopharmacology of posttraumatic stress disorder. *Depress. Anxiety* 25, 260–271. <https://doi.org/10.1002/da.20292>.
114. Wood, S.K., and Valentino, R.J. (2017). The brain norepinephrine system, stress and cardiovascular vulnerability. *Neurosci. Biobehav. Rev.* 74, 393–400. <https://doi.org/10.1016/j.neubiorev.2016.04.018>.
115. Taylor, D., Lenox-Smith, A., and Bradley, A. (2013). A review of the suitability of duloxetine and venlafaxine for use in patients with depression in primary care with a focus on cardiovascular safety, suicide and mortality due to antidepressant overdose. *Ther. Adv. Psychopharmacol.* 3, 151–161. <https://doi.org/10.1177/2045125312472890>.
116. Gold, P.W., Machado-Vieira, R., and Pavlatou, M.G. (2015). Clinical and biochemical manifestations of depression: relation to the neurobiology of stress. *Neural Plast.* 2015, 581976. <https://doi.org/10.1155/2015/581976>.
117. Blier, P. (2016). Neurobiology of depression and mechanism of action of depression treatments. *J. Clin. Psychiatry* 77, e319. <https://doi.org/10.4088/JCP.13097tx3c>.
118. Haenisch, B., Bilkei-Gorzo, A., Caron, M.G., and Bönisch, H. (2009). Knockout of the norepinephrine transporter and pharmacologically diverse antidepressants prevent behavioral and brain neurotrophin alterations in two chronic stress models of depression. *J. Neurochem.* 111, 403–416. <https://doi.org/10.1111/j.1471-4159.2009.06345.x>.
119. Chandley, M.J., and Ordway, G.A. (2012). Noradrenergic Dysfunction in Depression and Suicide. In *The Neurobiological Basis of Suicide*, Y. Dwivedi, ed. (CRC Press/Taylor & Francis).
120. Delgado, P.L., and Moreno, F.A. (2000). Role of norepinephrine in depression. *J. Clin. Psychiatry* 61 (Suppl 1), 5–12.
121. Moret, C., and Briley, M. (2011). The importance of norepinephrine in depression. *Neuropsychiatr. Dis. Treat.* 7 (Suppl 1), 9–13. <https://doi.org/10.2147/NDT.S19619>.
122. Goekoop, J.G., de Winter, R.F.P., Wolterbeek, R., Van Kempen, G.M.J., and Wiegant, V.M. (2012). Increased plasma norepinephrine concentration in psychotic depression. *Ther. Adv. Psychopharmacol.* 2, 51–63. <https://doi.org/10.1177/2045125312436574>.
123. Linnoila, M., Oliver, J., Adinoff, B., and Potter, W.Z. (1988). High correlations of norepinephrine, dopamine, and epinephrine and their major metabolite excretion rates. *Arch. Gen. Psychiatry* 45, 701–704. <https://doi.org/10.1001/archpsyc.1988.01800320011001>.
124. Weiss, J.M., and Simson, P.E. (1988). Neurochemical and electrophysiological events underlying stress-induced depression in an animal model. *Adv. Exp. Med. Biol.* 245, 425–440. https://doi.org/10.1007/978-1-4899-2064-5_33.
125. Pavcovich, L.A., and Ramirez, O.A. (1991). Time course effects of uncontrollable stress in locus coeruleus neuronal activity. *Brain Res. Bull.* 26, 17–21. [https://doi.org/10.1016/0361-9230\(91\)90186-n](https://doi.org/10.1016/0361-9230(91)90186-n).
126. Daniels, S., El Mansari, M., Hamoudeh, R., and Blier, P. (2023). Ketamine promptly normalizes excess norepinephrine and enhances dopamine neuronal activity in Wistar Kyoto rats. *Front. Pharmacol.* 14, 1276309. <https://doi.org/10.3389/fphar.2023.1276309>.
127. Grant, M.M., and Weiss, J.M. (2001). Effects of chronic antidepressant drug administration and electroconvulsive shock on locus coeruleus electrophysiologic activity. *Biol. Psychiatry* 49, 117–129. [https://doi.org/10.1016/s0006-3223\(00\)00936-7](https://doi.org/10.1016/s0006-3223(00)00936-7).
128. Melia, K.R., Rasmussen, K., Terwilliger, R.Z., Haycock, J.W., Nestler, E. J., and Duman, R.S. (1992). Coordinate regulation of the cyclic AMP system with firing rate and expression of tyrosine hydroxylase in the rat locus coeruleus: effects of chronic stress and drug treatments. *J. Neurochem.* 58, 494–502. <https://doi.org/10.1111/j.1471-4159.1992.tb09748.x>.
129. Tellioglu, T., and Robertson, D. (2001). Genetic or acquired deficits in the norepinephrine transporter: current understanding of clinical implications. *Expert Rev. Mol. Med.* 2001, 1–10. <https://doi.org/10.1017/S1462399401003878>.
130. Zhou, J. (2004). Norepinephrine transporter inhibitors and their therapeutic potential. *Drugs Future* 29, 1235–1244. <https://doi.org/10.1358/df.2004.029.12.855246>.
131. Ma, S., Chen, M., Jiang, Y., Xiang, X., Wang, S., Wu, Z., Li, S., Cui, Y., Wang, J., Zhu, Y., et al. (2023). Sustained antidepressant effect of ketamine through NMDAR trapping in the LHb. *Nature* 622, 802–809. <https://doi.org/10.1038/s41586-023-06624-1>.
132. Zhang, C., Zhu, H., Ni, Z., Xin, Q., Zhou, T., Wu, R., Gao, G., Gao, Z., Ma, H., Li, H., et al. (2022). Dynamics of a disinhibitory prefrontal microcircuit in controlling social competition. *Neuron* 110, 516–531.e6. <https://doi.org/10.1016/j.neuron.2021.10.034>.
133. Friard, O., and Gamba, M. (2016). BORIS: a free, versatile open-source event-logging software for video/audio coding and live observations. *Methods Ecol. Evol.* 7, 1325–1330. <https://doi.org/10.1111/2041-210X.12584>.

STAR★METHODS

KEY RESOURCES TABLE

REAGENT or RESOURCE	SOURCE	IDENTIFIER
Antibodies		
Rabbit anti-c-fos	Synaptic Systems	Cat# 226008; RRID:AB_2891278
Mouse anti-NeuN	Millipore	MAB337; RRID:AB_2298772
Rabbit anti-S100 β	Dako Products	Z0311; RRID:AB_10013383
Chicken anti-GFP	Aves Labs	GFP-1010; RRID:AB_2307313
Rabbit anti-GFP	Invitrogen	A11122; RRID:AB_221569
Chicken anti-TH	Aves Labs	TYH-0020; RRID:AB_10013440
Rabbit anti-TH	Santa Cruz Biotechnology	sc-14007; RRID:AB_671397
Rabbit anti-RFP	Rockland	600-401-379; RRID:AB_2209751
Chicken-anti-mCherry	Abcam	AB205402; RRID:AB_2722769
Goat anti-rabbit Alexa Fluor 546	Invitrogen	A11035; RRID:AB_2534093
Goat anti-rabbit Alexa Fluor 488	Invitrogen	A11034; RRID:AB_2576217
Goat anti-mouse Alexa Fluor Cy5	Invitrogen	A10524; RRID:AB_10562712
Goat anti-chicken Alexa Fluor 488	Invitrogen	A11039; RRID:AB_2534096
Goat anti-mouse Alexa Fluor 488	Invitrogen	A11029; RRID:AB_2534088
Goat anti- mouse Alexa Fluor 546	Invitrogen	A11030; RRID:AB_2737024
Goat anti-chicken Alexa Fluor 546	Invitrogen	A11040; RRID:AB_1500590
Bacterial and virus strains		
AAV2/9-CaMKIIa-GCaMP6s	Addgene	Cat# 107790-AAV9
AAV2/9-hSyn-jRGECO1a	Addgene	Cat# 100854-AAV9
AAV2/5-GfaABC ₁ D-cyto-GCaMP6f	Addgene	Cat# 52925-AAV5
AAV2/5-GfaABC ₁ D-lck-GCaMP6f	Addgene	Cat# 2924-AAV5
AAV2/9-CAG-Flex-GCaMP6s-WPRE-pA	Taitool Bioscience (Shanghai)	Cat# S0354-9
AAV2/9-EF1a-DIO-Axon-GCaMP6s-WPRE-pA	BrainVTA (Wuhan)	Cat# PT-1227
AAV2/9-hSyn-GRAB _{NE2H} -WPRE-SV40-pA	Vigene (Shandong)	Cat# YL003011-AAV9
AAV2/5-GfaABC ₁ D-SF1GluSnFR(A184S)-WPRE-SV40pA	BrainVTA (Wuhan)	Cat# PT-2450
AAV2/5-GfaABC ₁ D-Ado1.0m-WPRE-SV40pA	BrainVTA (Wuhan)	Cat# PT-9019
AAV2/9-hSyn-eNpHR3.0-mCherry-WPRE-pA	Taitool Bioscience (Shanghai)	Cat# S0463-9
AAV2/9-EF1a-DIO-hM4Di-EGFP-WPRE-pA	BrainVTA (Wuhan)	Cat# PT-0987
AAV2/9-hSyn-mCherry-WPRE-pA	Taitool Bioscience (Shanghai)	Cat# S0238-9
AAV2/5-GfaABC ₁ D-hM3Dq-mCherry	Taitool Bioscience (Shanghai)	Cat# S0483-5
AAV2/9-hSyn-ChrimsonR-tdTomato-WPRE-SV40pA	Taitool Bioscience (Shanghai)	Cat# S0459-9
AAV2/9-hSyn-Flex-ChrimsonR-mCherry-WPRE-pA	Taitool Bioscience (Shanghai)	Cat# S0739-9
AAV2/5-GfaABC ₁ D-mCherry	Sunbio Medical Biotechnology (Shanghai)	PAAVE3126
AAV2/8-GfaABC ₁ D-cOpn5-T2A-mCherry-WPRE-pA	Minmin Luo Lab (Chinese Institution for Brain Research, Beijing)	N/A
AAV2/5-GfaABC ₁ D-cOpn5-T2A-mCherry-WPRE-pA	Taitool Bioscience (Shanghai)	AAV2/5-XT670

(Continued on next page)

Continued

REAGENT or RESOURCE	SOURCE	IDENTIFIER
AAV2/5-GfaABC ₁ D- β ARK-p2A-mCherry-WPRE-pA	Sunbio Medical Biotechnology (Shanghai)	Cat# PSE5374
AAV2/5-GfaABC ₁ D-IP ₃ R2-shRNA-mCherry-WPRE-pA	Sunbio Medical Biotechnology (Shanghai)	PAAVE3465
AAV2/5-GfaABC ₁ D-mCherry-T2A-Cre-WPRE-pA	OBiO scientific service (Shanghai)	H9463
AAV2/5-GfaABC ₁ D-EGFP-P2A-iCre-WPRE-pA	Taitool Bioscience (Shanghai)	S0407-5
AAV2/5-GfaABC ₁ D-EGFP-WPRE-pA	Taitool Bioscience (Shanghai)	S0246-5

Chemicals, peptides, and recombinant proteins

Tetrodotoxin citrate (TTX)	alomone labs	T-550
Norepinephrine (NE)	Sigma	HY-13715
Picrotoxin (PTX)	Tocris	1128
Serotonin	MCE	HY-B1473A
γ -Aminobutyric acid	Sigma	A2129
Dopamine	APEXBio	B1482
Clozapine N-oxide	Sigma	C0832
Deschloroclozapine	MCE	HY-42110
Clozapine	MCE	HY-14539
PPADS tetrasodium	MCE	HY-101044
Suramin hexasodium salt	APEXBio	B6752
DPCPX	MCE	HY-100937
SCH582661	MCE	HY-19533
APV	Sigma	A5282
NBQX	MCE	HY-15068
Prazosin hydrochloride	MCE	HY-B0193A
Atipamezole hydrochloride	MCE	HY-12380
Propranolol hydrochloride	MCE	HY-B0573
Scopolamine	Tocris	114-49-8
Mecamylamine hydrochloride	MCE	HY-B1395
MPEP hydrochloride	MCE	HY-14609
LY341495	MCE	HY-70059
Silodosin	MCE	HY-10122
L-765314	MCE	HY-101385
BMY-7378	Tocris	HY-100554
Reboxetine mesylate	MCE	HY-14560C
Imipramine	Sigma	10899-5G

Experimental models: Organisms/strains

C57BL/6J mice	Qizhen or Jihui Laboratory animal Shanghai	N/A
Aldh111-Cre	The Jackson Laboratory	JAX. 023748
TH-Cre	The Jackson Laboratory	JAX. 008601
Adra1a-flox	GemPharmatech Co., Ltd	T007139

Software and algorithms

CamFibrePhotometry	ThinkerTech, Nanjing	http://www.thinkerbiotech.com/
InperStudioMultiColorEVAL15	Inper Ltd., China	https://www.inper.com
InperStudio	Inper Ltd., China	https://www.inper.com
Inper Data Process.	Inper Ltd., China	https://www.inper.com
MATLAB R2015b or R2019b	MathWorks	https://www.mathworks.com/products/matlab.html

(Continued on next page)

Continued

REAGENT or RESOURCE	SOURCE	IDENTIFIER
Custom analysis code	This paper and Zhang et al. ¹³²	https://zenodo.org/records/15087544 ; https://zenodo.org/record/5591050
Prism	GraphPad Software	https://www.graphpad.com/scientific-software/prism
BORIS	Friard and Gamba ¹³³	http://www.boris.unito.it/
ImageJ	National Institutes of Health	https://imagej.nih.gov/ij/index.html
FV31S-SW	OLYMPUS	https://www.olympus-lifescience.com/en/downloads/detail-iframe/?0[downloads][id]=847252002
HCIImage Live	HAMAMATSU Photonics	https://hcimage.com/hcimage-overview/hcimage-live/
NIS-Elements AR4.5.00	OLYMPUS	http://www.olympusconfocal.com/products/fv1000/fv1000software.html
Any-maze software	Stoelting	https://stoeltingco.com/Neuroscience/ANY-maze
Electrical V1.0.4	SansBio, Jiangsu	https://www.sansbio.com/
Other		
473 nm, 589 nm and 635 nm laser LED	Inper Ltd., China	https://www.inper.com
Fiber photometry system	ThinkerTech, Nanjing or Inper Ltd., China	http://www.thinkerbiotech.com/ ; https://www.inper.com

EXPERIMENTAL MODEL AND STUDY PARTICIPANT DETAILS

Animals

Data for experiments were collected from male adult C57BL/6J strain mice (Qizhen or Jihui Laboratory animal), Aldh111-Cre (The Jackson Laboratory, JAX. 023748), TH-Cre (The Jackson Laboratory, JAX. 008601) and Adra1a-flox (GemPharmatech Co., Ltd, T007139) transgenic mice, all over 8 weeks of age. Mice were housed in groups of four or five randomly under standard conditions (12-hour light/dark cycle) with food and water available *ad libitum*. Mice were habituated in the behavioral rooms for 0.5-1h before all the behavioral experimentations. All animal-related experimental procedures were under the guidelines of the Animal Care and Use Committee of the animal facility at Zhejiang University.

METHOD DETAILS

Surgery and viral injection

Mice were deeply anaesthetized by 1% pentobarbital sodium (100 mg/kg body weight) and head-fixed in a stereotactic frame (RWD Instruments). Virus was injected into the target brain regions (LHb: AP, - 1.72 mm from bregma; ML, \pm 0.46 mm; DV, - 2.62 mm from the brain surface; mPFC: AP, + 2.43 mm from bregma; ML, \pm 0.4 mm; DV, - 1.3 mm from the brain surface; LH: AP, - 0.90 mm from bregma; ML, \pm 1.10 mm; DV, - 4.90 mm from the brain surface; STR: AP, + 0.80 mm from bregma; ML, \pm 2.0 mm; DV, - 2.20 mm from the brain surface; BLA: AP, + 1.40 mm from bregma; ML, \pm 3.10 mm; DV, - 4.5 mm from the brain surface; HPC: AP, -2.20 mm from bregma; ML, \pm 1.35 mm; DV, - 1.20 mm from the brain surface; LC: AP, -5.5 mm from bregma; ML, \pm 0.9 mm; DV, - 3.40 mm from the brain surface) using a pulled glass pipette connected to a pressure microinjector (Picospritzer III, Parker). The injection needle remained in place for approximately 10 min before being withdrawn to prevent fluid reflux. For optic fiber implantation, a 200- μ m optic fiber was placed 300 μ m above the center of the viral injection site and cemented onto the skull with dental acrylic. For bilateral inhibition of the LHb neurons or multi-regions photometry recording, optic fiber was implanted to target brain regions (LHb: -1.72 mm AP, \pm 1.14 mm ML, -2.35 mm DV, and angled at 15 from the vertical in the lateral direction; LH: -0.9 mm AP, \pm 2.32 mm ML, -4.4 mm DV, and angled at 15 from the vertical in the lateral direction). After surgery, mice were allowed to recover from anesthesia on a heat pad.

After all experiments were completed, mice were transcardially perfused under deep anesthesia with 0.1 M phosphate buffered saline (PBS) followed 4% w/v paraformaldehyde (PFA) to verify the sites of virus injection and fiber placement. Brains were postfixed in 4% w/v PFA for 12 hours, followed by cryoprotection in a 30% w/v sucrose solution for 1~2 days. The dehydrated brains were then sectioned into 40 μ m thick coronal slices using a cryostat (Leica). The slices were counterstained with DAPI or Hoechst before imaging. Fluorescent image acquisition was performed using an Olympus Fluoview FV1000 confocal microscope. Only data from mice with correct virus injection site and optic fiber location site were used.

For calcium recording experiments, the following viruses were used: AAV2/9-CaMKIIa-GCaMP6s (titre: 1.0×10^{13} vector genome (v. g.)/ml, dilution: 1: 8, 0.1 μ l into LHb, BLA, 0.2 μ l into LH, mPFC, STR, HPC, Addgene), AAV2/9-hSyn-jRGECO1a (titre: 1.0×10^{13} vector genome (v. g.)/ml, dilution: 1:3, 0.15 μ l into LHb, Addgene), AAV2/5-GfaABC₁D-cyto-GCaMP6f (titre: 7.0×10^{12} vector genome (v. g.)/ml, 0.25 μ l into LHb, BLA, LH, mPFC, HPC, STR, Addgene), AAV2/5-GfaABC₁D-lck-GCaMP6f (titre: 7.0×10^{12} vector genome (v. g.)/ml, 0.25 μ l into LHb, BLA, LH, mPFC, HPC, STR, Addgene), AAV2/9-CAG-Flex-GCaMP6s-WPRE-pA (titre: 1.66×10^{13} vector genome (v. g.)/ml, dilution: 1: 5, 0.2 μ l into LHb, Taitool Bioscience), AAV2/9-EF1a-DIO-Axon-GCaMP6s-WPRE-pA (titre: 5.14×10^{12} vector genome (v. g.)/ml, 0.2 μ l into LC, BrainVTA).

For sensor recording experiments, the following viruses were used: AAV2/9-hSyn-GRAB_{NE2H}-WPRE-SV40-pA (titre: 1.0×10^{13} vector genome (v. g.)/ml, dilution: 1: 3, 0.2 μ l into LHb, Vigene), AAV2/5-GfaABC₁D-SFiGluSnFR (A184S)-WPRE-SV40pA (titre: 1.0×10^{13} vector genome (v. g.)/ml, 0.2 μ l into LHb, BrainVTA), AAV2/5-GfaABC₁D-ADO1.0m-WPRE-SV40pA (titre: 1.0×10^{13} vector genome (v. g.)/ml, 0.2 μ l into LHb, BrainVTA).

For manipulation experiments of neurons, the following viruses were used: AAV2/9-hSyn-ChrimsonR-tdTomato-WPRE-SV40pA (titre: 2.27×10^{13} vector genome (v. g.)/ml, dilution: 1: 10, 0.1 μ l into LHb, Taitool Bioscience), AAV2/9-hSyn-eNpHR3.0-mCherry-WPRE-pA (titre: 1.76×10^{13} vector genome (v. g.)/ml, dilution: 1: 8, 0.1 μ l into LHb, Taitool Bioscience), AAV2/9-hSyn-mCherry-WPRE-pA (titre: 2.49×10^{13} vector genome (v. g.)/ml, dilution: 1: 5, 0.1 μ l into LHb, Taitool Bioscience), AAV2/9-hSyn-Flex-ChrimsonR-mCherry-WPRE-pA (titre: 1.30×10^{13} vector genome (v. g.)/ml, dilution: 1: 5, 0.15 μ l into LC, Taitool Bioscience), AAV2/9-EF1a-DIO-hM4Di-EGFP-WPRE-pA (titre: 5.35×10^{12} vector genome (v. g.)/ml, 0.2 μ l per side bilateral into LC, BrainVTA).

For manipulation experiments of astrocytes, the following viruses were used: AAV2/5-GfaABC₁D-hM3Dq-mCherry (titre: 1.45×10^{13} vector genome (v. g.)/ml, dilution: 1: 5, 0.2 μ l per side bilateral into LHb, plasmid from Addgene); AAV2/5-GfaABC₁D-mCherry (titre: 2.08×10^{13} vector genome (v. g.)/ml, dilution: 1: 5, 0.2 μ l per side bilateral into LHb, Sunbio Medical Biotechnology); AAV2/8-GfaABC₁D-cOpn5-T2A-mCherry-WPRE-pA (0.2 μ l per side bilateral into LHb, provided by M. Luo); AAV2/5-GfaABC₁D-cOpn5-T2A-mCherry-WPRE-pA (0.2 μ l per side bilateral into LHb, Taitool Bioscience); AAV2/5-GfaABC₁D- β ARK-p2A-mCherry-WPRE-pA (titre: 1.9×10^{13} vector genome (v. g.)/ml, 0.2 μ l per side bilateral into LHb, plasmid from Addgene); AAV2/5-GfaABC₁D-IP₃R2-shRNA-mCherry-WPRE-pA (titre: 2.61×10^{13} vector genome (v. g.)/ml, 0.2 μ l per side bilateral into LHb, Sunbio Medical Biotechnology); AAV2/5-GfaABC₁D-mCherry-T2A-Cre-WPRE-pA (titre: 1.14×10^{13} vector genome (v. g.)/ml, 0.15 μ l per side bilateral into LHb, OBiO scientific service); AAV2/5-GfaABC₁D-EGFP-P2A-iCre-WPRE-pA (titre: 1×10^{13} vector genome (v. g.)/ml, 0.1 μ l per side bilateral into LHb, Taitool Bioscience); AAV2/5-GfaABC₁D-EGFP-WPRE-pA (titre: 1×10^{13} vector genome (v. g.)/ml, 0.1 μ l per side bilateral into LHb, Taitool Bioscience).

For the experiments of astrocytic manipulation and neuronal recording, the virus of manipulating astrocyte was injected first, followed by the injection of neuronal GCaMP 3-4 weeks later.

In vivo fiber photometry recording

The calcium signals of multi-regions were simultaneously recorded using fiber photometry systems (ThinkerTech, Nanjing). A beam of 488 nm excitation light was delivered, and fluorescence signals were acquired at a sampling rate of 50 Hz. To minimize fluorescence signal bleaching, the laser intensity was adjusted to a low level (40 μ W) at the tip of optic fiber.

The calcium signals of astrocytes and neurons were simultaneously recorded using dual-color fiber photometry recording systems (ThinkerTech, Nanjing; Inper Ltd., China). System delivered two excitation light sources, 470 nm and 580 nm, allowing simultaneous recording of red and green indicators at a frequency of 40 or 25 frames per channel per second. The light power was approximately 40 μ W for the 470 nm wavelength and the 50 μ W for the 580 nm wavelength at the tip of optic fiber.

During the recording of signals under the FS stress, the mice were placed into an FS chamber (SansBio, Jiangsu) with metal grid floor and subjected to unpredictable FS (1s, 0.4-1 mA). A video camera was positioned above the chamber to track each mouse.

Optogenetic manipulations in fiber photometry recording

To synchronize optogenetic manipulation and photometry recording, we utilized fiber photometry recording systems combined with photostimulation (Inper Ltd., China). In the experiments involving the activation of LHb neurons, LHb-LC terminals and LCTH-LHb terminals, we applied 1 s red-light pulses (635 nm, 2-5 mW at fiber tip, 5 ms or 10 ms pulse width). In the experiments involving inhibition of LHb neurons, we applied constant yellow light (589 nm, 10 mW at fiber tip). When the light was delivered, a trigger simultaneously sent a TTL pulse to the data recording systems, allowing verification of the exact time points when the light was turned on.

Analysis of fiber photometry data

Data were analyzed using the codes (e. g. OpSignal, from Thinker Tech Nanjing Biotech Co., Ltd. and Inper Ltd., China) based on MATLAB. The fluorescence responses were indicated by $\Delta F/F_0$ (calculated as $(F-F_0)/F_0$). F_0 represents the baseline average fluorescence signals in a 2-second-long period prior to the onset of FS stress or light on. $\Delta F/F_0$ are presented as heatmaps and also as average plots with a shaded area indicating the SEM. For the quantification of rise and decay of signals, rise time was defined as latency from 10% peak signal timing to 80% peak signal timing. Decay time was defined as latency from peak timing decay to 50% peak activity timing. The peak of signals during response period (10 s from the stimulus onset) was detected by finding a maximum response. For quantification of inflection point, average fluorescence signals evoked by FS stress for each mouse were used to define the point of decay slope change as the inflection point. For signal-phase analysis of neuronal calcium, phase1 was defined as the period from the onset of FS timing to the inflection point timing and phase2 was defined as the period from the inflection point timing to 10% peak activity timing. For astrocyte-loss-of-function experiments, the phases of neuronal calcium signals

were defined as follows: phase1 was the period from the onset of FS to 2.5 s, and phase2 was from 2.5 s to 40 s (It is difficult to identify the inflection point of neuronal calcium signals when inhibiting astrocytic calcium signaling). The quantification of AUC1 and AUC2 of NE signals evoked by FS excluded ramp values.

Drugs application in vivo recording

The following drugs were administered intraperitoneally (i.p.). Concentrations were as follows: Prazosin hydrochloride (4 mg/kg, MCE), Propranolol (40 mg/kg, MCE), Atipamezole hydrochloride (0.5 mg/kg, MCE), Scopolamine (1 mg/kg, Tocris), Mecamylamine hydrochloride (2.5 mg/kg, MCE), MPEP hydrochloride (20 mg/kg, MCE), LY341495 (2.5 mg/kg, MCE), Silodosin (5 mg/kg, MCE), L-765314 (5 mg/kg, MCE) and BMY-7378 (2.5 mg/kg, Tocris), Reboxetine (20 mg/kg, MCE), Imipramine (10 mg/kg and 20 mg/kg, Sigma).

For inhibition of LC NE neurons, four weeks after injection of AAV2/9-EF1a-DIO-hM4Di-EGFP-WPRE-pA into LC, clozapine (1 mg/kg, MCE) or saline was administered to TH-Cre mice by intraperitoneal injection.

For activation of LHb astrocytes, four weeks after injection of AAV2/5-GfaABC₁D-hM3Dq-mCherry or AAV2/5-GfaABC₁D-mCherry and AAV2/9-CaMKII α -GCaMP6s into LHb, clozapine (0.25, 0.5, 1 mg/kg, MCE) or saline was administered to mice by intraperitoneal injection.

For experiments of inhibitors and antagonists administration, each recording session was separated by 30-50 minutes to ensure drug effectiveness.

Acute brain slice preparation for imaging

Sagittal LHb slices were prepared from C57BL/6J or Aldh111-Cre mice with AAV virus injection for in vitro calcium imaging. Briefly, mice were deeply anesthetized with pentobarbital sodium and decapitated with sharp shears. The brains were sliced in ice-cold modified artificial CSF (ACSF) (oxygenated with 95% O₂ and 5% CO₂) containing the following (in mM): 220 sucrose, 2 KCl, 6 MgCl₂, 0.2 CaCl₂, 26 NaHCO₃, 1.2 NaH₂PO₄, and 10 D-glucose. A vibratome (Leica2000) was used to cut 300 μ m brain sections. The slices were allowed to equilibrate for 30 min at 34-36 °C in normal ACSF containing (in mM): 125 NaCl, 2.5 KCl, 2 CaCl₂, 1 MgCl₂, 25 NaHCO₃, 1.25 NaH₂PO₄, and 25 D-glucose with 1 mM pyruvate added, continuously bubbled with 95% O₂ and 5% CO₂. Slices were allowed to recover for at least 1h in the same buffer until use. All slices were used within 5-8 hours of slicing.

In vitro imaging

Slice preparation was performed as described above. In neuronal calcium imaging and sensors imaging experiments, images were captured on an Olympus two-photon microscope (FVMPE-RS, Tokyo, Japan) equipped with a mode-locked Ti:Sapphire laser (MaiTai DeepSee, SpectraPhysics, San Francisco, USA) set at 920 nm and a water-immersion objective lens (25 \times , N.A. 1.05; Nikon, Tokyo, Japan). Regions with virus expression in the LHb were identified and full-frame images were acquired at 0.92 Hz. In astrocytic calcium imaging experiments, for optogenetic manipulation experiments, images were captured on an Olympus two-photon microscope (FVMPE-RS, Tokyo, Japan). For other experiments, images were captured on a digital CMOS camera (ORCA-Flash4.0 V3; HAMAMATSU and FL 9BW; TUCSEN) with a water-immersion objective lens (40 \times , N.A. 0.85). Full-frame images were acquired at 4 Hz. A constant flow of fresh buffer perfused the imaging chamber at all times.

Optogenetic manipulations in two-photon imaging

Experiments were conducted on mice expressing GfaABC₁D-cOPN5 and CaMKII α -GCaMP6s, with cOPN5 being expressed one month prior to GCaMP6s to ensure optimal expression of cOPN5. In optogenetic manipulation experiments, an optical fiber connecting a photostimulation system (Inper, China) was placed on the slices and delivered red light (635 nm, 5 mW at fiber tip, 5 ms or 10 ms pulse width) for neuronal ChrimsonR activation, or blue light (473 nm, 60 μ W at fiber tip, 1 s constant) for astrocytic cOPn5 activation.

Drug applications in vitro

The following drugs were applied in the bath: Norepinephrine (5 μ M and 10 μ M, MCE), Phenylephrine (10 μ M, Sigma), γ -Aminobutyric acid (300 μ M, Sigma), Serotonin (20 μ M, MCE), Dopamine (10 μ M, APEXBio), Clozapine N-oxide (CNO; 1 μ M, Sigma), Picrotoxin (100 μ M, Tocris), PPADS tetrasodium (50 μ M, MCE), Suramin hexasodium salt (75 μ M, APEXBio), DPCPX (300 nM, MCE), SCH582661 (100 nM, MCE), APV (50 μ M, Sigma), NBQX (10 μ M, MCE), Prazosin hydrochloride (10 μ M, MCE), Atipamezole hydrochloride (1 μ M, MCE), Propranolol hydrochloride (10 μ M, MCE), Tetrodotoxin citrate (TTX; 1 μ M, Alomone labs).

For experiments of inhibitors and antagonists bath, each slice imaging session was separated at least 10 min to permit drug penetration.

Analysis of imaging data

Calcium imaging analysis was conducted using FIJI (ImageJ) and MATLAB. Image XY drift was corrected using MATLAB. For CMOS camera imaging data (excluding [Figures S6F](#) and [S6G](#)), the entire field of view (FOV) was selected as the region of interest (ROI). In [Figures S6F](#) and [S6G](#), the FOV was uniformly divided into 128 \times 128 segments and the segments with calcium activities exceeding the threshold ($\Delta F/F_0 > 10\%$ in response to 5 μ M NE) were selected as ROIs. For two-photon imaging data of sensors and astrocytic calcium signals, regions exhibiting fluorescence (including soma and process of astrocytes) during the experiment were selected as ROIs. For two-photon imaging data of neuronal calcium signals, the neuronal somatic regions were selected as ROIs and any neurons with unintended expression of cOPN5 were excluded from the analysis. The fluorescence responses were indicated by

$\Delta F/F_0$ (calculated as $(F-F_0)/F_0$). F_0 represents the baseline average fluorescence signals in a 10-second period prior to the onset of light on or a 60-second period prior to the drug application. $\Delta F/F_0$ were presented as heatmaps and also as average plots with a shaded area indicating the SEM.

The recorded neurons show three modes of spontaneous calcium activity at resting conditions. We calculated the standard deviation (SD) of calcium fluorescence value and the SD of calcium-event intervals for each neuron during the resting conditions. Neurons were classified as silent if they showed no calcium events during recording (SD of fluorescence value < 30); Neurons were classified as regular if they showed periodic calcium events during recording (SD of fluorescence value > 30 and SD of calcium-event interval < 10); Neurons were classified as irregular if they showed irregular calcium events during recording (SD of fluorescence value > 30 and SD of calcium-event interval > 10).

For the recording of LHb neurons during astrocytic-hM3Dq activation, we calculated the mean fluorescence for each neuron during the control period (180-second period before CNO application) and during the CNO-responsive period (180-second period during CNO application). Neurons were identified as excited if their mean fluorescence during CNO-responsive period was at least 2.5-fold above during the control period. For the recording of LHb neurons during astrocyte-cOpn5 activation, photostimulations (473 nm, 60 μ W at fiber tip, 1s constant) were performed 6-8 times. Neurons were identified as excited if they exhibited high response fidelity (> 80%). To quantify the effect of inhibitors and antagonists, neurons with stable responses (response fidelity > 80%, signal decay < 10%) to cOPN5 in normal ACSF were included in the analysis. We separately calculated the mean cOPN5-evoked calcium peak in normal ACSF (control) and in ACSF with inhibitors or antagonists added. Neurons were identified as inhibited if their mean calcium peak in the presence of inhibitors or antagonists decreased by at least 30% compared to the control.

Immunohistochemistry

In experiment of immunohistochemistry for c-Fos, four weeks after injection of AAV2/5-GfaABC₁D-hM3Dq-mCherry or AAV2/5-GfaABC₁D-mCherry into LHb, deschloroclozapine (0.5 mg/kg, MCE), clozapine (0.25 mg/kg, 0.5 mg/kg, 1 mg/kg, MCE) or saline was administered to mice by intraperitoneal injection. Two hours after administration, mice were sacrificed for immunohistochemistry of c-Fos. In experiment of immunohistochemistry for NeuN, S100 β , GFP and RFP, mice were sacrificed, after all the experiments were completed.

Mice were deeply anesthetized with 1% pentobarbital sodium and perfused transcardially with 0.1 M phosphate buffer saline (PBS, pH = 7.4) followed by 4% paraformaldehyde in PBS. Brains were removed and postfixed overnight and dehydrated in 30% sucrose in PBS. Coronal brain sections (40 μ m) were serially cut and divided for 6 interleaved sets.

The antibodies used were rabbit anti-c-Fos (1:2000, SYSY), mouse anti-NeuN (1:500, Millipore), rabbit anti-S100 β (1:1000, Dako Products), chicken anti-GFP (1:2000, Aves Labs), rabbit anti-GFP (1:2000, Invitrogen), chicken anti-TH (1:1000, Aves Labs), rabbit anti-TH (1:1000, Santa Cruz Biotechnology), rabbit anti-RFP (1:1000, Rockland), Chicken-anti-mCherry (1:1000, Abcam); Alexa Fluor 546 goat anti-rabbit IgG, Alexa Fluor 488 goat anti-rabbit IgG, Alexa Fluor Cy5 goat anti-mouse IgG, Alexa Fluor 488 goat anti-chicken IgG, Alexa Fluor 488 goat anti-mouse IgG, Alexa Fluor 546 goat anti-mouse IgG, Alexa Fluor 546 goat anti-chicken IgG (all 1:1000, Invitrogen).

Slices for checking the injection site were counterstained with Hoechst in the final incubation step. Fluorescent image acquisition was performed with an Olympus Fluoview FV1000 confocal microscope.

Behavioral assays

Foot-shock stress (FS)

In FS-induced depression-like behaviors protocol, FS was performed as previously described.^{15,93} Mice were placed into a standard FS chamber (SansBio, Jiangsu) with metal grid floor and habituated to the new environment for 5 min. During a 20-min FS session, mice were subjected to 20 unpredictable FS (1 mA, 1 s) with an intershock interval of 45-75 s. In subthreshold FS protocol, mice were subjected to 6 unpredictable FS (1 mA, 1 s) with an intershock interval of 45-75 s. For activation of LHb astrocytic Gq pathway, Deschloroclozapine (0.5 mg/kg, MCE) was administered intraperitoneally (i.p.) 10 min before FS.

Forced swim test (FST)

FST was performed as previously described.^{17,131} Mice were gently and individually placed in a cylinder (12 cm diameter, 25 cm height) of water (23-24 °C) and swam for 6 min under normal light (100-200 lux). Water depth (15 cm) was set to prevent mice from touching the bottom with their tails or hind limbs. The entire test lasted for 6 min. A camera was set at the side of the cylinder to record the behaviors. The immobile duration during the last 4-min test were counted offline by an experienced observer blinded to the animal treatments. Immobility was defined by animals remaining floating or motionless with only small and necessary movements for keeping balance.

Sucrose preference test (SPT)

SPT was conducted as previously described.^{17,131} Animals were single housed and habituated to two bottles of drinking water for 2 days, followed by two bottles of 2% sucrose for 2 days. After habituation, the preference for any specific bottle was checked. Only mice without basal preference (between 25-75%) were used. Mice with basal preference of one bottle on the last day of habituation (below 25% or above 75%) were excluded. Mice were then water deprived for 24 hours. In the test phase, mice exposed to one

bottle of 2% sucrose and one bottle of water for 2 hours in the dark phase. The positions of 2 bottles were switched after 1 hour. The sucrose preference was calculated as the average of consumption of sucrose/ total consumption of water and sucrose during the 2 hours.

QUANTIFICATION AND STATISTICAL ANALYSIS

All data are shown as mean \pm SEM. Statistical analyses were done with Prism 6 (GraphPad) or MATLAB. By pre-established criteria, values were excluded from analyses if virus expression was poor or optic fiber location was out of the interested region. The data were analyzed by Student's test for Gaussian distributions, while Mann-Whitney test for non-Gaussian distributions. Results were considered statistically significant when the P value $<$ 0.05. More details are provided in [Table S1](#).

Supplemental figures

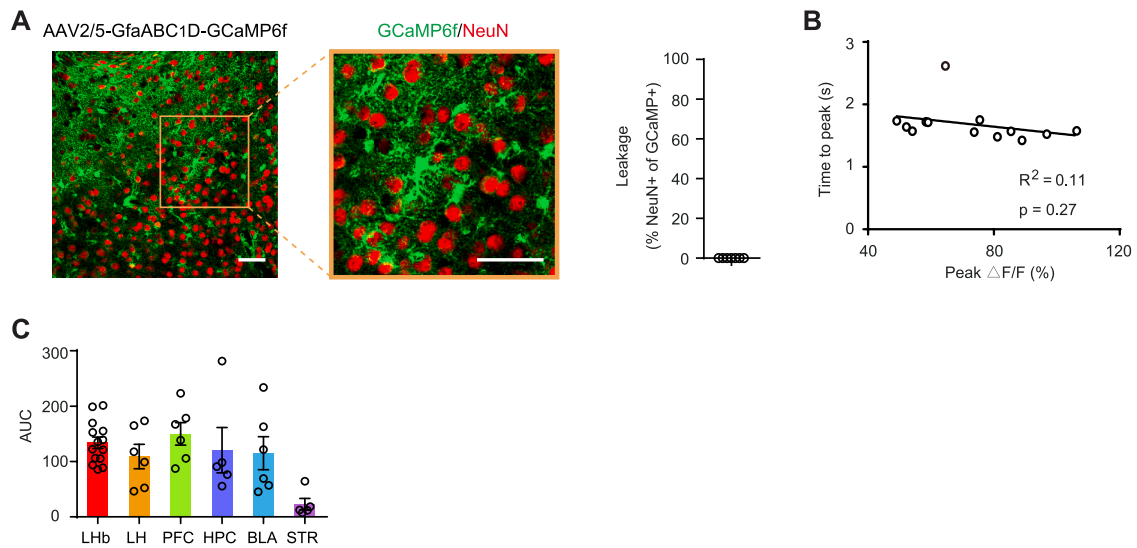


Figure S1. FS induces the most rapid calcium rise in LHb astrocytes, related to Figure 1

(A) GfaABC₁D-promoter-driven GCaMP is not expressed in neurons. Left and middle: representative images of LHb brain slices stained with antibodies against GFP (indicating GCaMP-positive cells, green) and NeuN (neuronal marker, red). Scale bar, 50 μ m. Right: bar graph showing percentage of GCaMP-positive cells that are NeuN positive ($n = 7$ slices from 4 mice).

(B) Scatterplots showing the relationship between peak amplitude and time to peak of LHb astrocytic calcium signals evoked by FS. Each circle represents one mouse.

(C) Average AUC of astrocytic calcium signals evoked by FS in 6 brain regions. Each circle represents one mouse.

* $p < 0.05$; ** $p < 0.01$; *** $p < 0.001$; **** $p < 0.0001$; n.s., not significant. Data are represented as mean \pm SEM.

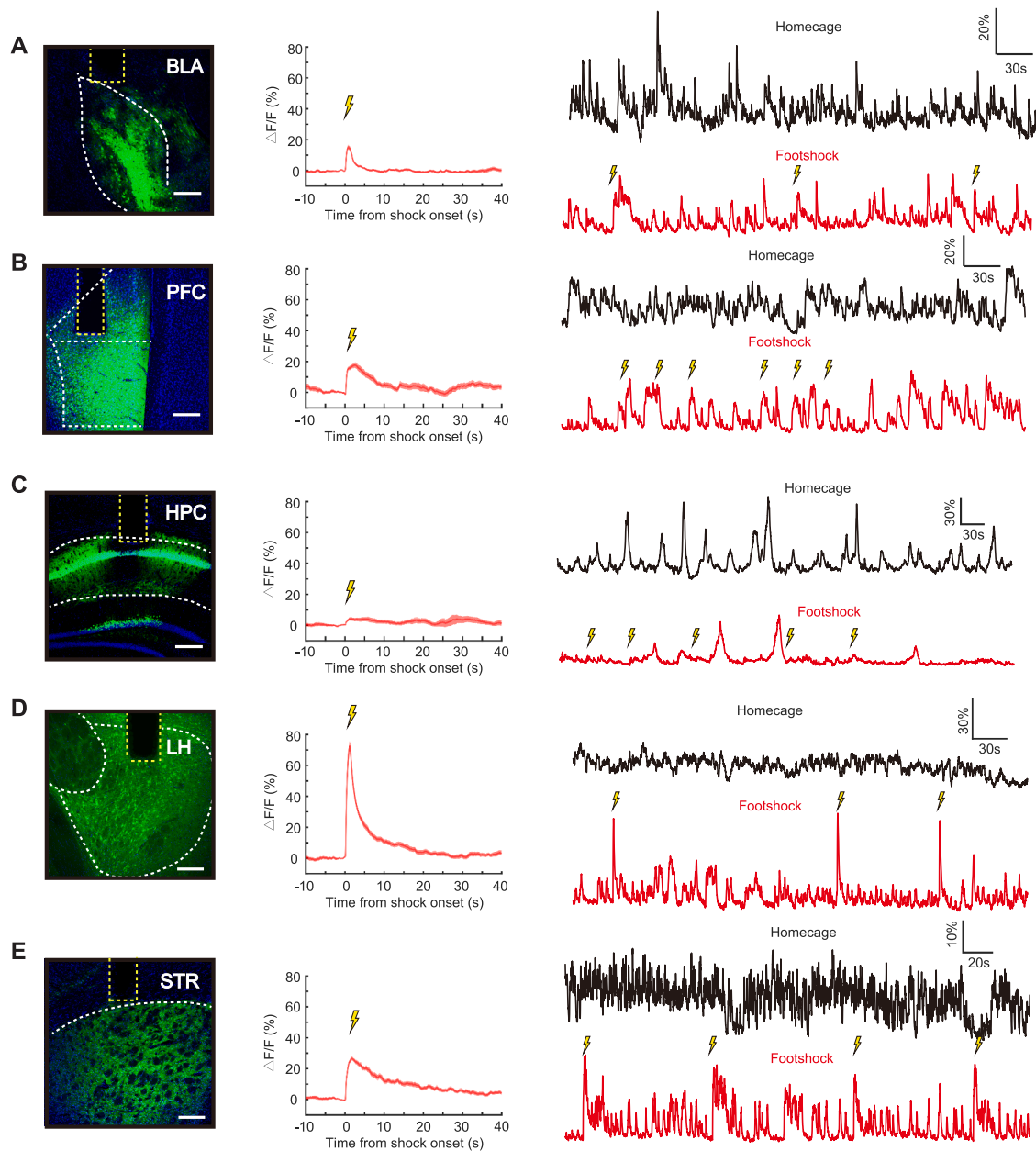


Figure S2. Neuronal calcium response evoked by FS in the other five brain regions, related to Figure 2

(A–E) Left: illustration of viral expression and optic fiber placement (indicated by the yellow dotted line) in BLA (A), mPFC (B), HPC (C), LH (D), and STR (E), the boundary of which is outlined by the white dotted line. Green, GCaMP6s; blue, Hoechst. Scale bars, 100 μ m. Middle: average $\Delta F/F$ ratio of neuronal calcium signals from BLA (A, $n = 3$ mice), mPFC (B, $n = 7$ mice), HPC (C, $n = 7$ mice), LH (D, $n = 3$ mice), and STR (E, $n = 3$ mice), aligned to the onset of FS. Solid lines indicate mean and shaded areas indicate SEM. Right: representative traces of recorded neuronal calcium signals from the 5 CNS regions during homecage (top) and continuous FSs (bottom).

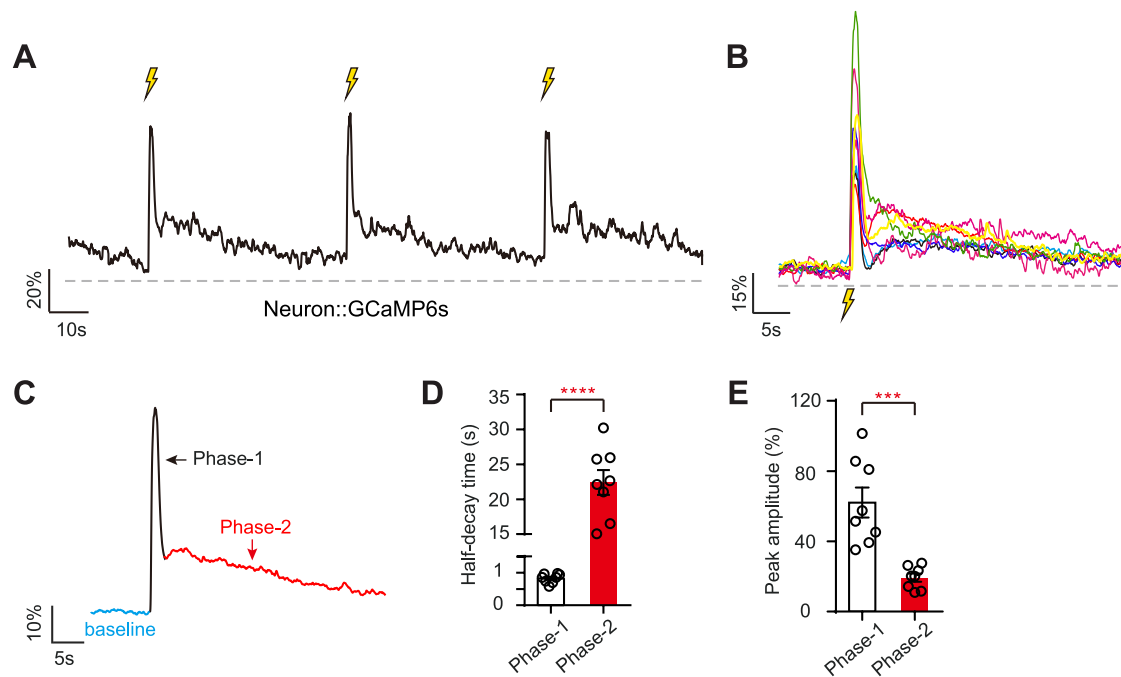


Figure S3. FS induces biphasic calcium activities in LHB neurons, related to Figure 2

(A) Representative traces of recorded neuronal calcium signals in LHB over three continuous FSs. Scale bars, 20% deltaF/F, 10 s.

(B) Alignment of FS-onset plots of average calcium signals of recorded neurons from individual animal during FS (n = 8 mice). Each trace represents one mouse.

(C) Illustration of segmented phases of FS-evoked LHB neuronal calcium signals.

(D) Average half-decay time in phase 1 and phase 2 of FS-evoked neuronal calcium signals. Each circle represents one mouse.

(E) Average peak amplitude in phase 1 and phase 2 of FS-evoked neuronal calcium signals. Each circle represents one mouse.

* $p < 0.05$; ** $p < 0.01$; *** $p < 0.001$; **** $p < 0.0001$; n.s., not significant. Data are represented as mean \pm SEM.

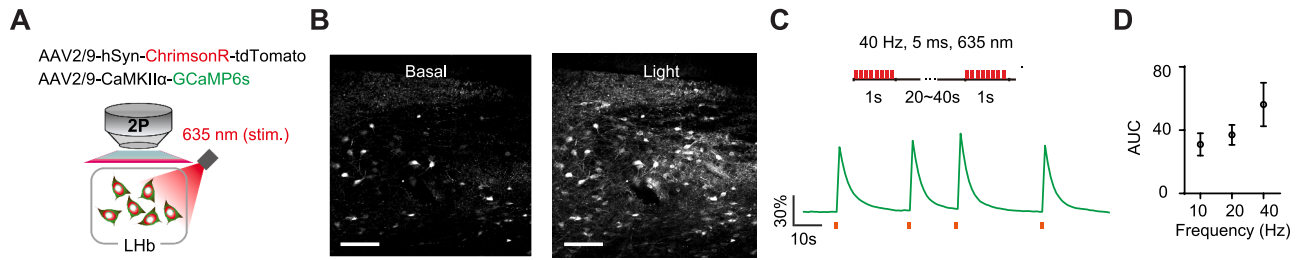


Figure S4. Optogenetic activation of ChrimsonR-expressing neurons induces neuronal calcium in Lhb slice, related to Figure 3

(A) Schematic illustrating optogenetic activation of ChrimsonR-expressing neurons while recording two-photon images of Lhb neuronal calcium responses.

(B) Calcium fluorescence images of Lhb neurons before (B, left) and after (B, right) optogenetic activation of Lhb neurons (1 s, 40 Hz).

(C) Neuronal calcium responses to optogenetic activation of Lhb neurons (1 s, 40 Hz) in Lhb slices.

(D) Mean neuronal calcium responses to varying stimulation frequencies in Lhb slices ($n = 10$ slices from 3 mice).

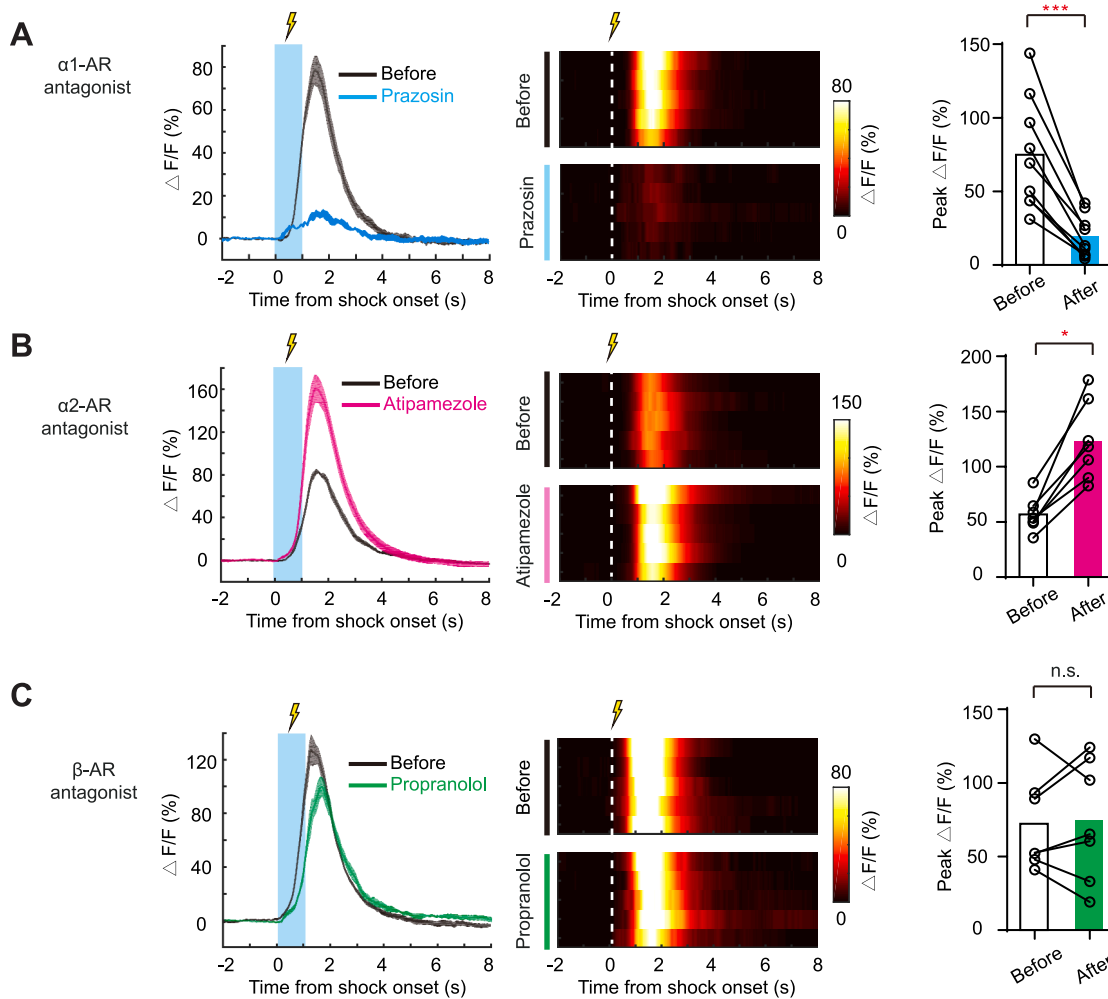


Figure S5. Calcium activities evoked by FS in Lhb astrocytes require noradrenergic signaling, related to Figure 3

(A–C) Plots of averaged $\Delta F/F$ ratio (left) and heatmap (middle) of FS-evoked calcium signals in Lhb astrocytes before and after i.p. injection of prazosin ($\alpha 1$ -AR antagonist, A), atipamezole ($\alpha 2$ -AR antagonist, B), and propranolol (β -AR antagonist, C), aligned to FS onset. Bar graph showing effects of NER antagonists on FS-evoked calcium signals in Lhb astrocytes (right). Each circle represents one mouse.

* $p < 0.05$; ** $p < 0.01$; *** $p < 0.001$; **** $p < 0.0001$; n.s., not significant. Data are represented as mean \pm SEM.

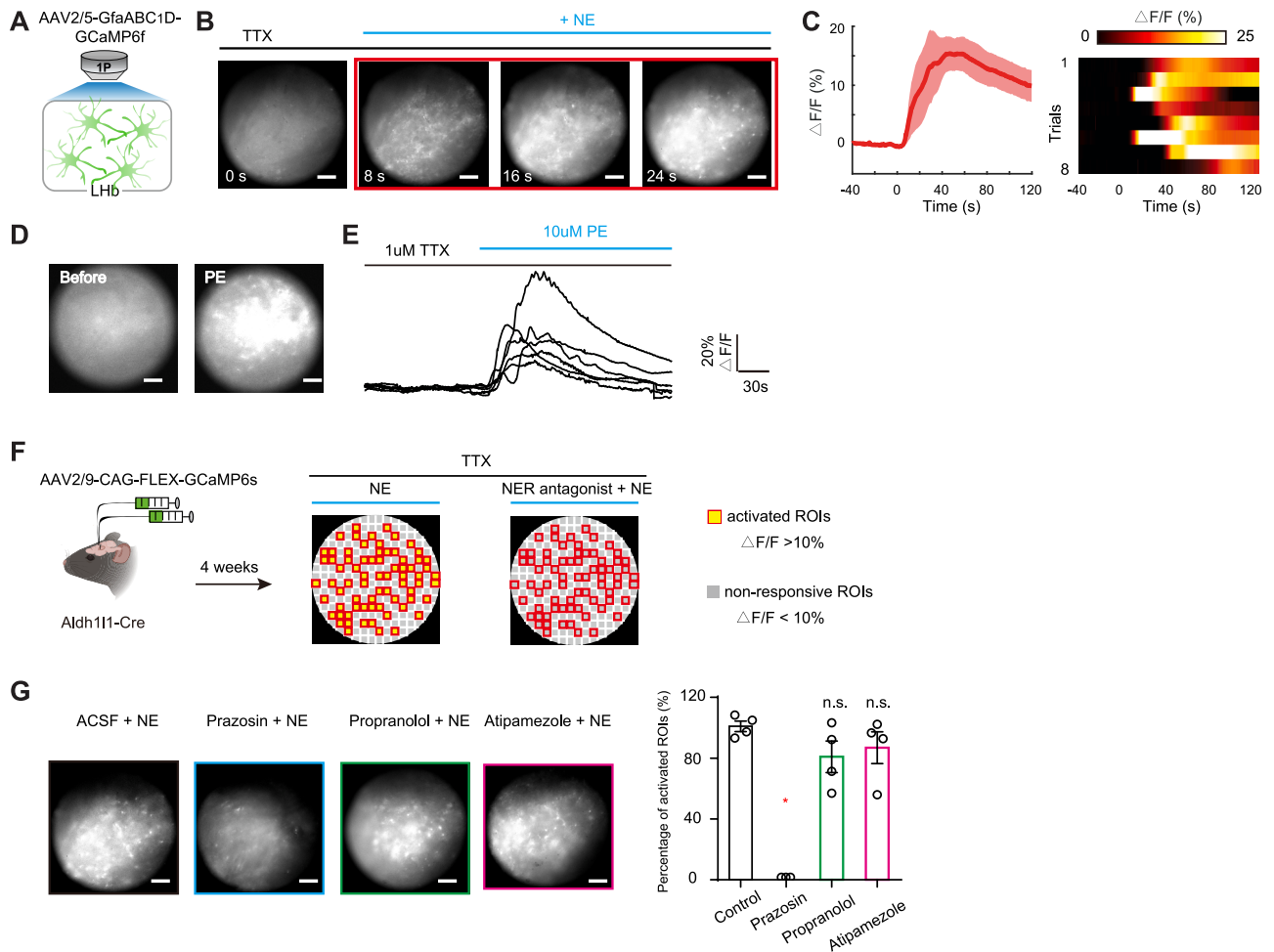


Figure S6. NE triggers calcium signal in LHB astrocytes via $\alpha 1$ -AR, related to Figure 3

(A) Schematic illustrating *in vitro* calcium imaging of LHB astrocytes in slices.

(B) Calcium fluorescence images of LHB astrocytes showing calcium increase at different time points after NE application ($n = 8$ slices from 8 mice). Scale bar: 50 μm (experiments were performed in TTX).

(C) Plots of $\Delta F/F$ ratio (left) and heatmap (right) of calcium signals in LHB astrocytes induced by NE ($n = 8$ slices from 8 mice). Solid lines indicate mean and shaded areas indicate SEM.

(D and E) Calcium fluorescence images of LHB astrocytes before (D, left) and after (D, right) application of PE ($\alpha 1$ -AR agonist). Traces (E) of LHB astrocytic calcium signals before and after PE application ($n = 6$ slices from 4 mice). Scale bars, 20% $\Delta F/F$, 30 s (experiments were performed in TTX).

(F) Schematic illustrating viral injection of Cre-dependent GCaMP6s in LHB in Aldh111-Cre mice and *in vitro* calcium imaging of LHB astrocytes in response to NE after application of NER antagonist. Region of interest (ROI) detection using a grid array (see STAR Methods for details).

(G) Representative calcium fluorescence images (left) and bar graph (right) showing effects of prazosin ($\alpha 1$ -AR antagonist), propranolol (β -AR antagonist), and atipamezole ($\alpha 2$ -AR antagonist) on LHB astrocytic calcium signals evoked by NE. Scale bar: 50 μm . Each circle represents one slice.

* $p < 0.05$; ** $p < 0.01$; *** $p < 0.001$; **** $p < 0.0001$; n.s., not significant. Data are represented as mean \pm SEM.

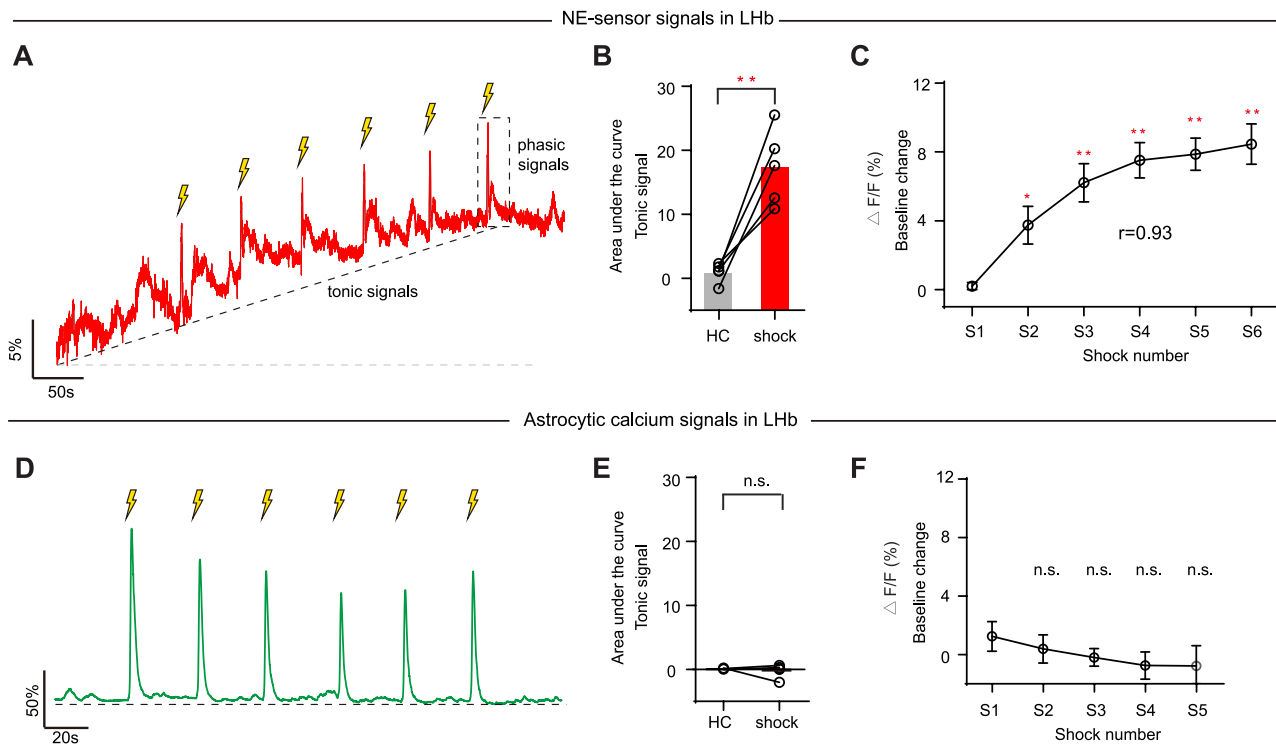


Figure S7. LHb NE sensor and astrocytic calcium signal induced by FS, related to Figure 3

(A) Example trace of LHb-NE-sensor signals over multiple FSs. Scale bars, 5% $\Delta F/F$, 50 s.

(B) AUC of basal (tonic) signal of LHb NE sensor in homecage (HC, gray) and in response to FS (red). Each circle represents one mouse.

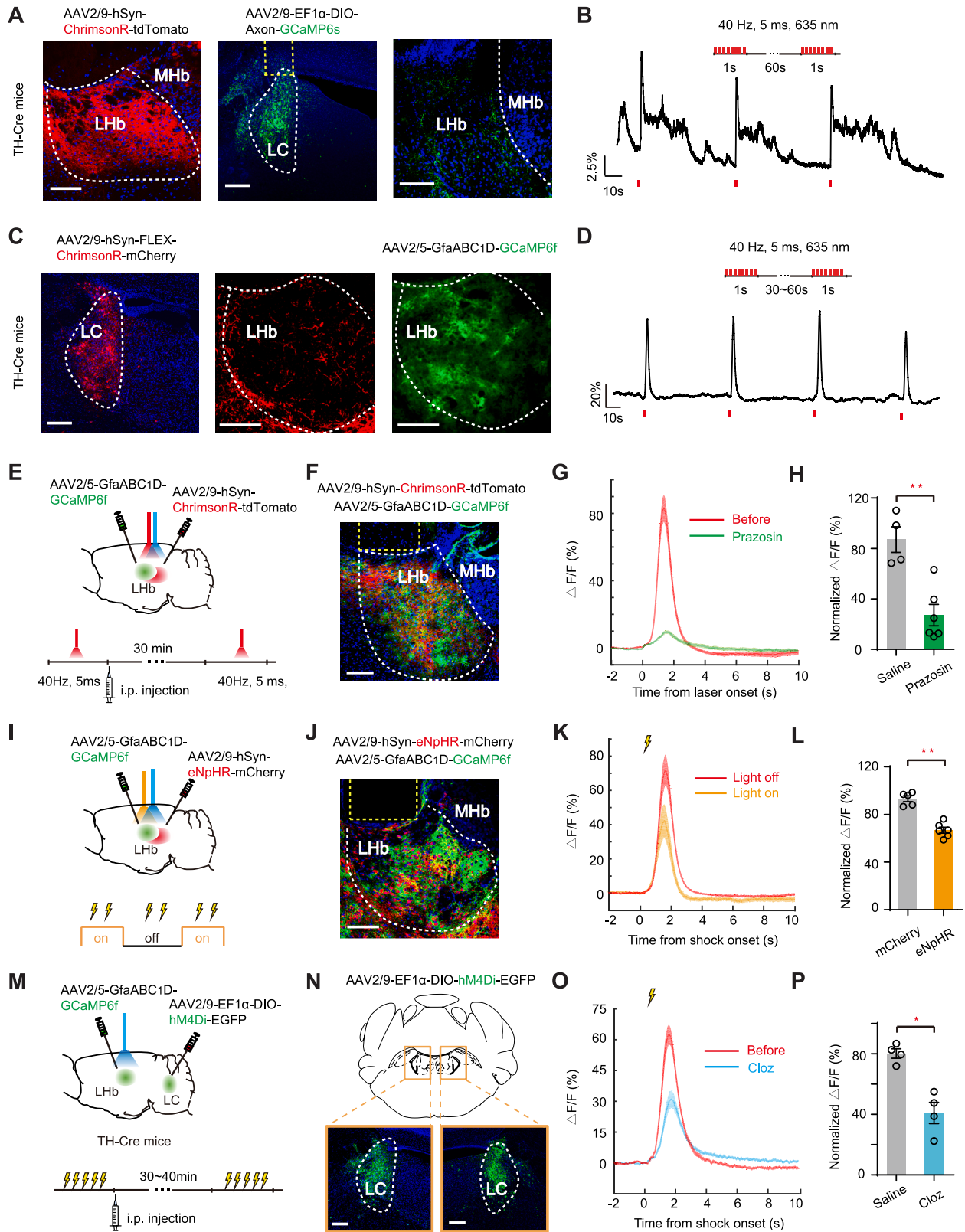
(C) Plots showing basal (tonic) signal change of LHb NE sensor in response to FS.

(D) Example trace of LHb astrocytic calcium signals over multiple FSs. Scale bars, 50% $\Delta F/F$, 20 s.

(E) AUC of basal signal of LHb astrocytic calcium in homecage (gray) and in response to FS (red). Each circle represents one mouse.

(F) Plots showing basal signal change of LHb astrocytic calcium in response to FS.

* $p < 0.05$; ** $p < 0.01$; *** $p < 0.001$; **** $p < 0.0001$; n.s., not significant. Data are represented as mean \pm SEM.



(legend on next page)

Figure S8. Effects of manipulating LHb and LC-NE neurons on LHb astrocytic calcium, related to Figure 3

(A and B) Effects of activating LHb-LC terminals on LC-NE neurons.

(A) Representative images showing viral expression of ChrimsonR in LHb neurons (left), GCaMP6s in LC-NE neurons (middle), and LC-NE neuron terminals in LHb (right, stained with antibody against GFP) in TH-Cre mice. Scale bar, 100 μm .

(B) Calcium responses of LC-NE neurons to optogenetic activation of LHb-LC terminals (1 s, 40 Hz) *in vivo*.

(C and D) Effects of activating LCTH-LHb terminals on LHb astrocytes.

(C) Representative images showing viral expression of ChrimsonR in LC-NE-neurons (left), LCTH-LHb terminals (middle, stained with antibody against RFP), and GCaMP6f in LHb astrocytes (right) in TH-Cre mice. Scale bar, 100 μm .

(D) Calcium responses of LHb astrocytes to optogenetic activation of LCTH-LHb terminals (1 s, 40 Hz).

(E–H) Effects of prazosin (α 1-AR antagonist) on LHb astrocytic calcium signals evoked by LHb neuron activation *in vivo*.

(E) Schematic illustrating optogenetic activation of LHb neurons and fiber photometry recording of LHb astrocytes.

(F) Representative image showing viral expression of ChrimsonR in LHb neurons and GCaMP6f in LHb astrocytes. Scale bar, 100 μm .

(G) Plots of averaged deltaF/F ratio of LHb astrocytic calcium signals induced by LHb neurons before and after i.p. injection of prazosin (α 1-AR antagonist), aligned to the laser onset. Solid lines indicate mean and shaded areas indicate SEM.

(H) Bar graph showing the effects of prazosin (α 1-AR antagonist) on astrocytic calcium signals evoked by LHb neurons. Each circle represents one mouse.

(I–L) Effects of inhibiting LHb neurons on FS-evoked calcium signals in LHb astrocytes.

(I) Schematic illustrating optogenetic inhibition of LHb neurons and fiber photometry recording of LHb astrocytes in response to FS.

(J) Representative image showing viral expression of eNpHR in LHb neurons and GCaMP6f in LHb astrocytes. Scale bar, 100 μm .

(K) Plots of averaged deltaF/F ratio of FS-evoked calcium signals in LHb astrocytes during light off and light on, aligned to FS onset. Solid lines indicate mean and shaded areas indicate SEM.

(L) Bar graph showing effects of inhibiting LHb neurons on FS-evoked calcium signals in LHb astrocytes. Each circle represents one mouse.

(M–P) Effects of inhibiting LC-NE neurons on FS-evoked calcium signals in LHb astrocytes.

(M) Schematic illustrating chemogenetic inhibition of LC-NE neurons and fiber photometry recording of LHb astrocytes in response to FS.

(N) Representative image showing viral expression of hM4Di (human M4 muscarinic designer receptors exclusively activated by designer drugs [DREADD] coupled to Gi) in LC-NE neurons. Scale bar, 100 μm .

(O) Plots of averaged deltaF/F ratio of FS-evoked calcium signals in LHb astrocytes before and after i.p. injection of clozapine (Cloz), aligned to FS onset. Solid lines indicate mean and shaded areas indicate SEM.

(P) Bar graph showing effects of inhibiting LC-NE neurons on FS-evoked calcium signals in LHb astrocytes. Each circle represents one mouse.

* $p < 0.05$; ** $p < 0.01$; *** $p < 0.001$; **** $p < 0.0001$; n.s., not significant. Data are represented as mean \pm SEM.

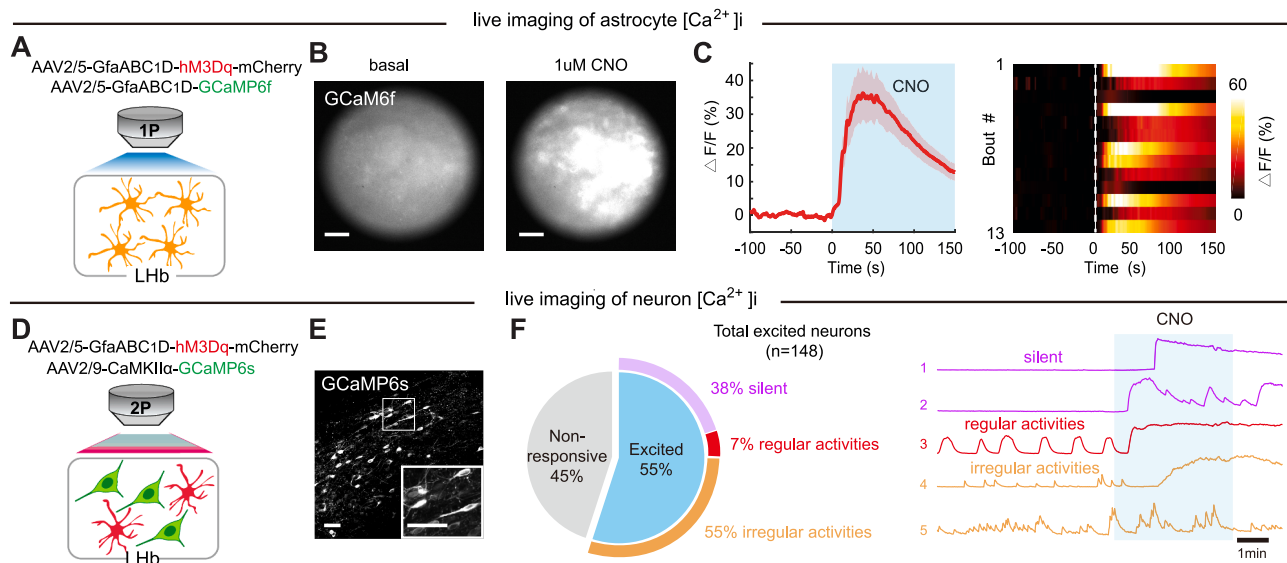


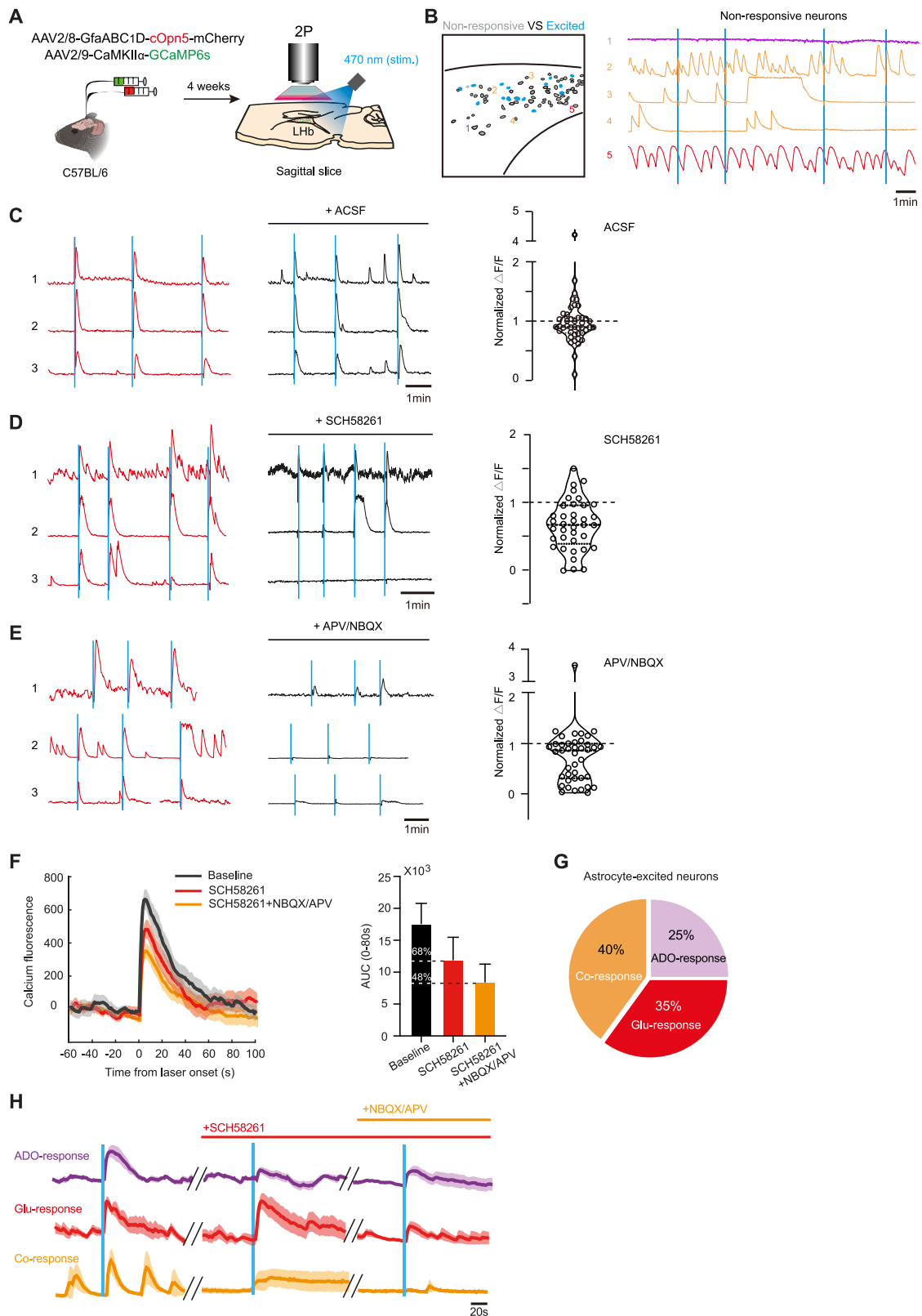
Figure S9. Chemogenetic activation of astrocytic Gq pathway in LHb slice, related to Figure 4

(A and B) Schematic (A) and representative calcium fluorescence images (B) illustrating chemogenetic activation of hM3Dq-expressing astrocytes while recording calcium fluorescence images of LHb astrocytic calcium responses. Scale bar: 50 μ m.

(C) Plots of $\Delta F/F$ ratio (left) and heatmap (right) of calcium signals in LHb astrocytes before and after CNO application ($n = 3$ mice). Solid lines indicate mean and shaded areas indicate SEM.

(D and E) Schematic (D) and representative two-photon image (E) illustrating chemogenetic activation of hM3Dq-expressing astrocytes while recording two-photon image of LHb neuronal calcium responses. Scale bar: 50 μ m.

(F) Pie chart illustrating percent abundance of excited neurons by astrocytic hM3Dq activation (left, $n = 3$ slices from 2 mice). Colored outer circle indicates percentage of three types (according to baseline activity) among astrocytic-hM3Dq-excited neurons. Representative raw calcium traces from the three types of astrocytic hM3Dq-excited neurons (right).



(legend on next page)

Figure S10. Pharmacology on optogenetic activation of astrocytic Gq pathway in LHb slice, related to Figure 4

- (A) Schematic illustrating optogenetic activation of cOpn5-expressing astrocytes while recording two-photon images of LHb neuronal calcium responses.
- (B) Left: example spatial map of astrocytic cOpn5-excited and non-responsive neurons in LHb. Right: representative raw calcium traces from the three types of non-responsive neurons. Blue line represents light on.
- (C–E) Traces of LHb neuronal calcium signals induced by astrocyte-cOpn5 before (left) and after (middle) application of various receptor antagonists. Right: bar graph showing effects of ACSF (control, C), SCH58261 (adenosine $A_{2A}R$ antagonist, D), and APV/NBQX (iGluR antagonists, E) on LHb neuronal calcium signals induced by astrocyte-cOpn5. Each circle represents one neuron.
- (F–H) Effect of antagonists of glutamate receptors and adenosine receptors on astrocyte-evoked neuronal calcium activities.
- (F) Left: plots of calcium fluorescence in LHb neurons aligned to laser onset under baseline, SCH58261, and combining SCH58261 with NBQX and APV incubation. Right: bar graph showing effects of $A_{2A}R$ and combining $A_{2A}R$ with iGluRs antagonists on neuronal calcium fluorescence evoked by astrocytes ($n = 3$ slices from 3 mice).
- (G) Pie chart illustrating percent of subclasses neurons responding to astrocytic excitation ($n = 3$ slices from 3 mice).
- (H) Example calcium traces from the three types of astrocytic-cOpn5-excited neurons.

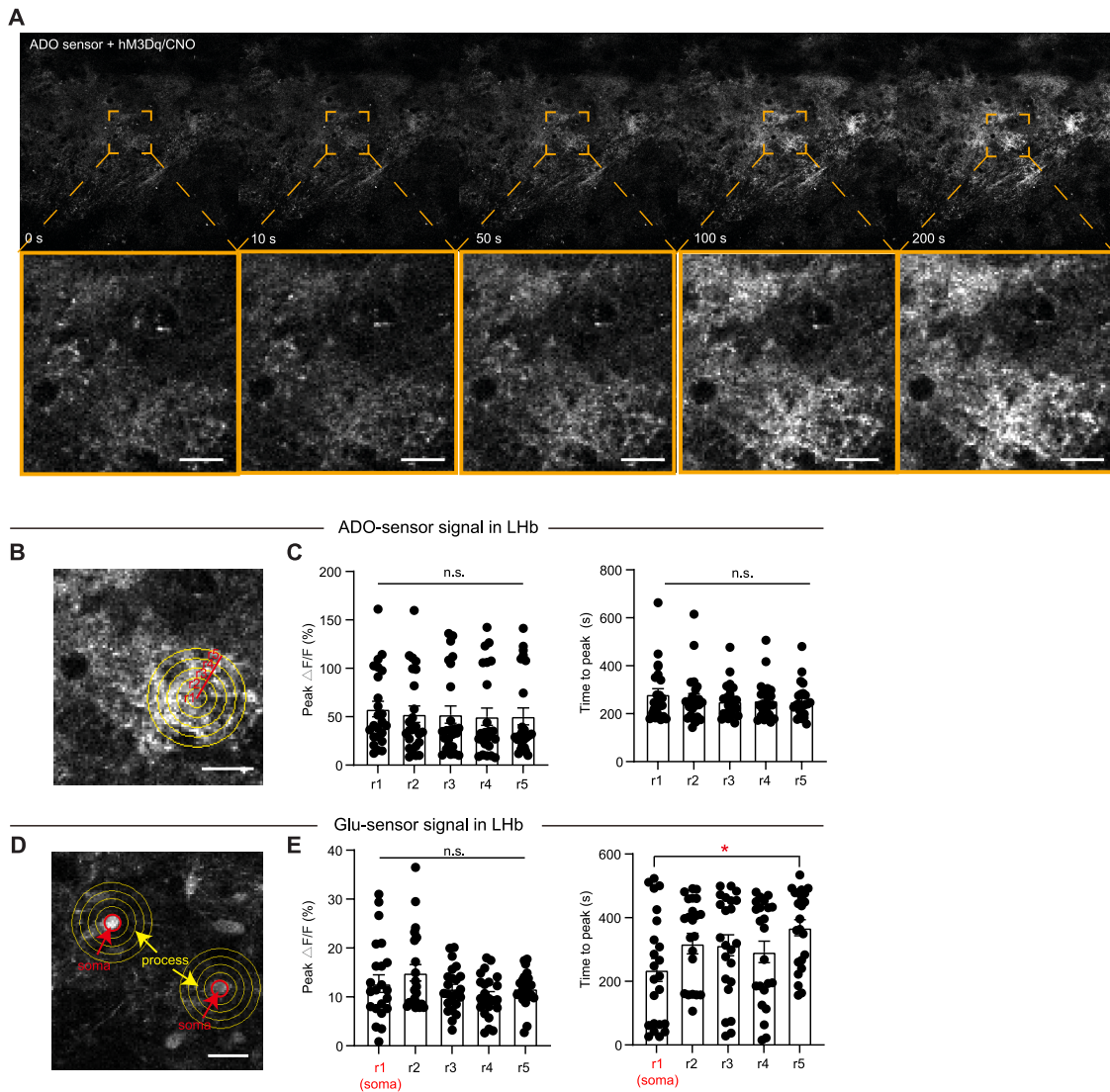


Figure S11. The spatial and temporal distribution of adenosine and glutamate released by astrocytes in LHB, related to Figure 4

(A) ADO sensor responses to chemogenetic activation of LHB astrocytes. Top: global increased fluorescence of ADO sensor in LHB with CNO application (1 μ M, with TTX to exclude indirect release from neuronal activation). Bottom: zoomed-in images showing the release patterns of adenosine upon astrocytic Gq activation. Experiments are in wild-type (WT) mice expressing ADO sensor and hM3Dq in LHB astrocytes.

(B) Example zoomed-in image showing equidistant distribution of ADO signals in ROIs.

(C) Bar graphs showing peak amplitude (left) and time to peak (right) of ADO signals following astrocytic activation by hM3Dq (24 ROIs for each equal distance, $n = 3$ slices from 3 mice). Each circle represents one ROI. Note that there was no significant difference in peak amplitude and time to peak across randomly selected ROIs.

(D) Example zoomed-in image showing equidistant distribution of Glu signals in ROIs of soma and process signals.

(E) Bar graphs showing the peak amplitude (left) and time to peak (right) of Glu signals following astrocytic activation by hM3Dq (23 ROIs for each equal distance, $n = 3$ slices from 3 mice). Each circle represents one ROI. Note that there was a difference in time to peak between soma and distal process (r1 vs. r5).

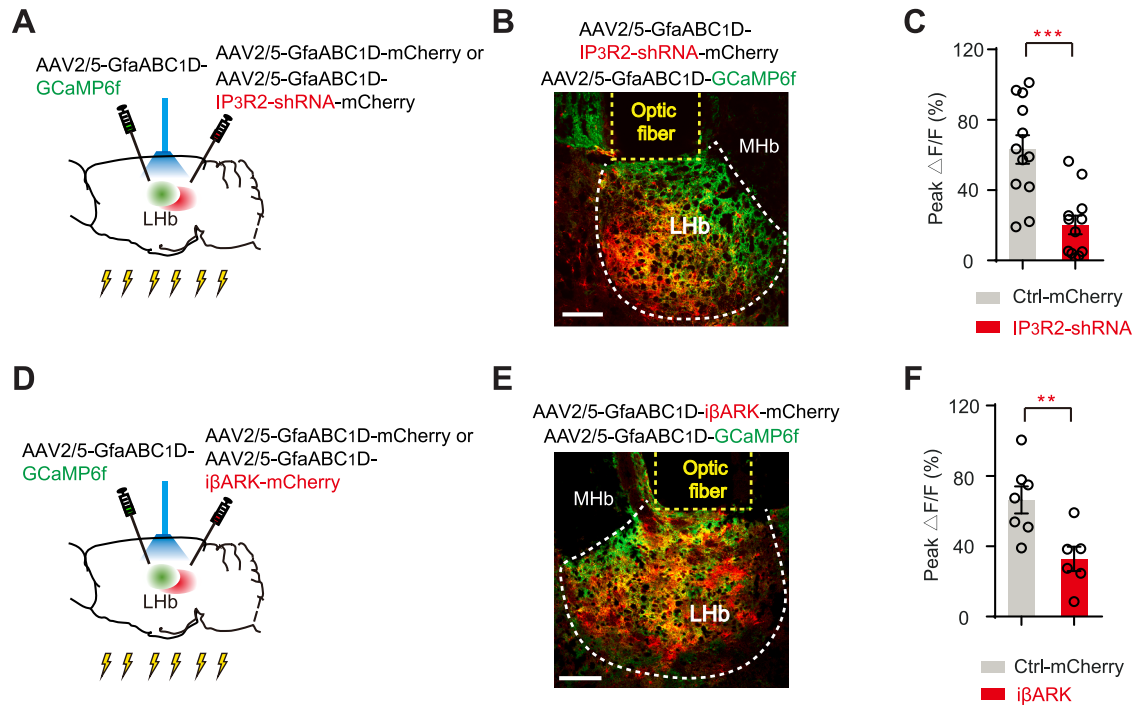


Figure S12. Effects of inhibition of astrocytic calcium signaling on FS-evoked astrocytic calcium in LHb, related to Figure 5

(A–C) Schematic (A) illustrating the viral expression of astrocyte-specific IP₃R2-shRNA or Ctrl-mCherry and GCaMP6f, and fiber photometry recording of astrocytes in LHb in response to FS. Representative image (B) illustrating viral expression of IP₃R2-shRNA and GCaMP6f in LHb astrocytes. Scale bar, 100 μ m. Quantification of peak amplitude of FS-evoked LHb astrocytic calcium signals in mice expressing Ctrl-mCherry (gray, $n = 12$ mice) or IP₃R2-shRNA (red, $n = 12$ mice) in LHb astrocytes (C).

(D–F) Schematic (D) illustrating the viral expression of astrocyte-specific iβARK or Ctrl-mCherry and GCaMP6f, and fiber photometry recording of astrocytes in LHb in response to FS. Representative image (E) illustrating viral expression of iβARK and GCaMP6f in LHb astrocytes. Scale bar, 100 μ m. Quantification of peak amplitude of FS-evoked LHb astrocytic calcium signals in mice expressing Ctrl-mCherry (gray, $n = 7$ mice) or iβARK (red, $n = 6$ mice) in LHb astrocytes (F).

* $p < 0.05$; ** $p < 0.01$; *** $p < 0.001$; **** $p < 0.0001$; n.s., not significant. Data are represented as mean \pm SEM.

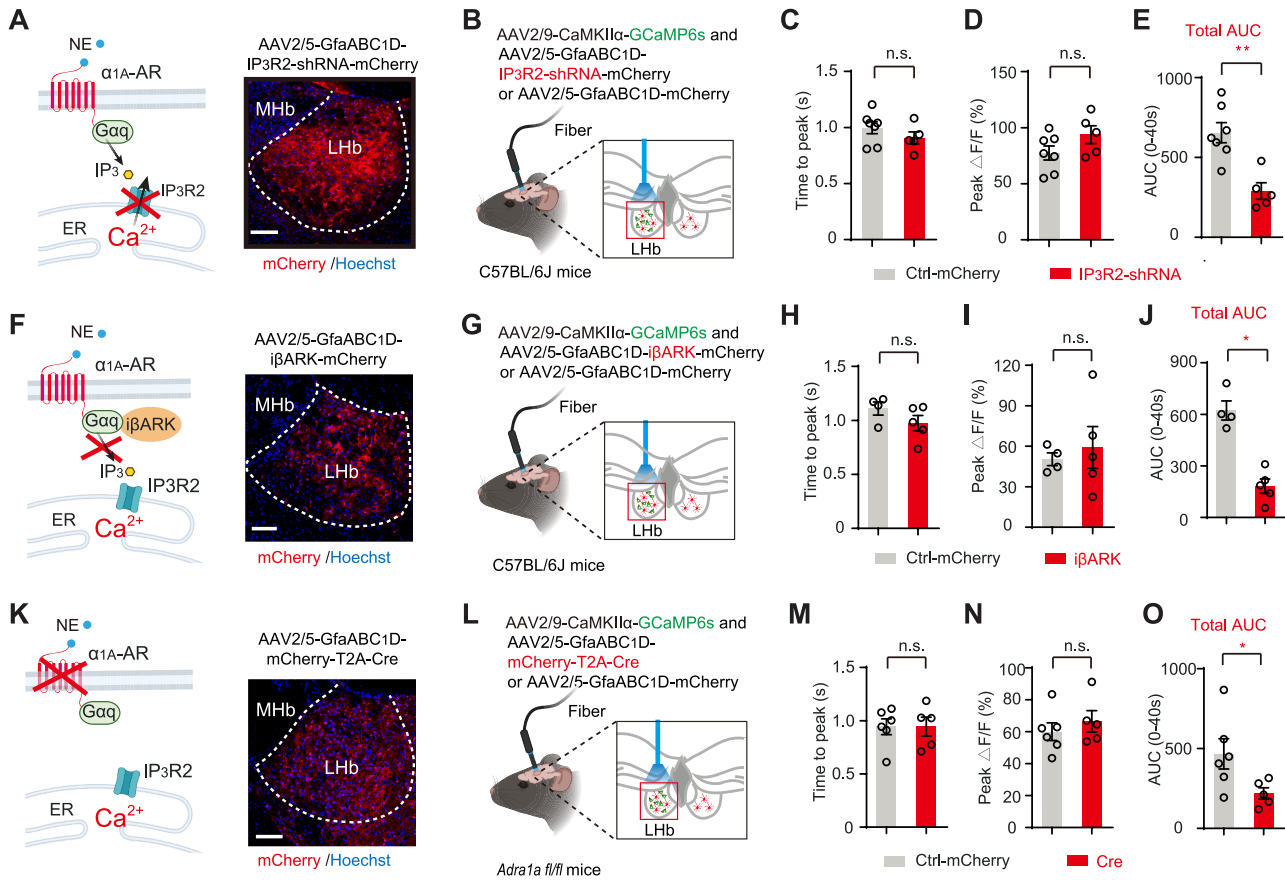


Figure S13. Effects of inhibition of astrocytic calcium signaling on FS-evoked neuronal calcium in LHB, related to Figure 5

(A) Left: illustration of blockade of astrocytic calcium signaling by IP₃R2-shRNA. Right: viral expression of IP₃R2-shRNA in astrocytes. Scale bar, 100 μ m.

(B) Schematic illustrating the viral expression of astrocyte-specific IP₃R2-shRNA or Ctrl-mCherry in bilateral LHB and neuron-GCaMP6s in unilateral LHB, and fiber photometry recording of neurons in LHB.

(C-E) Quantification of time to peak (C), peak amplitude (D), and total AUC in 0–40 s (E) of FS-evoked LHB neuronal calcium signals in mice expressing Ctrl-mCherry or IP₃R2-shRNA in LHB astrocytes. Each circle represents one mouse.

(F) Left: illustration of blockade of astrocytic calcium signaling by iβARK. Right: viral expression of iβARK in astrocytes. Scale bar, 100 μ m.

(G) Schematic illustrating the viral expression of astrocyte-specific iβARK or Ctrl-mCherry in bilateral LHB and neuron-GCaMP6s in unilateral LHB, and fiber photometry recording of neurons in LHB.

(H-J) Quantification of time to peak (H), peak amplitude (I), and total AUC in 0–40 s (J) of FS-evoked LHB neuronal calcium signals in mice expressing Ctrl-mCherry or iβARK in LHB astrocytes. Each circle represents one mouse.

(K) Left: illustration of blockade of astrocytic calcium signaling by conditional knockout of α_{1A} -AR in LHB astrocytes. Right: viral expression of Cre in astrocytes (stained with antibody against mCherry). Scale bar, 100 μ m.

(L) Schematic illustrating the viral expression of astrocyte-specific Cre or Ctrl-mCherry in bilateral LHB and neuron-GCaMP6s in unilateral LHB, and fiber photometry recording of neurons in LHB in *Adra1a* fl/fl mice.

(M-O) Quantification of time to peak (M), peak amplitude (N), and total AUC in 0–40 s (O) of FS-evoked LHB neuronal calcium signals in mice expressing Ctrl-mCherry or Cre in LHB astrocytes. Each circle represents one mouse.

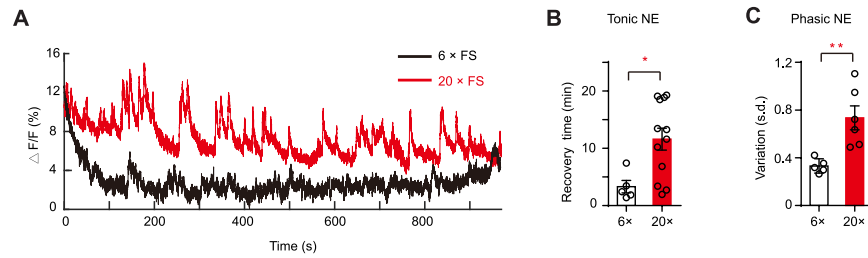


Figure S14. Lhb-NE-sensor signals following 6x and 20x foot shocks, related to Figure 6

(A) Representative traces of NE signal in Lhb following 6x (black) and 20x (red) FS.

(B) Bar graph showing that 20x FS induced more sustained NE responses in the Lhb ($n = 5, 12$ mice for 6x and 20x groups, respectively). After the last FS, the tonic Lhb-NE signals returned to baseline after 3.3 min under the 6x FS protocol and after 11.6 min under the 20x FS protocol. Each circle represents one mouse.

(C) Bar graph showing that 20x FS induced more phasic NE transients in the Lhb, with a 2.3-fold increase compared with the 6x FS protocol ($n = 5, 6$ mice for 6x and 20x groups, respectively).

* $p < 0.05$; ** $p < 0.01$; *** $p < 0.001$; **** $p < 0.0001$; n.s., not significant. Data are represented as mean \pm SEM.

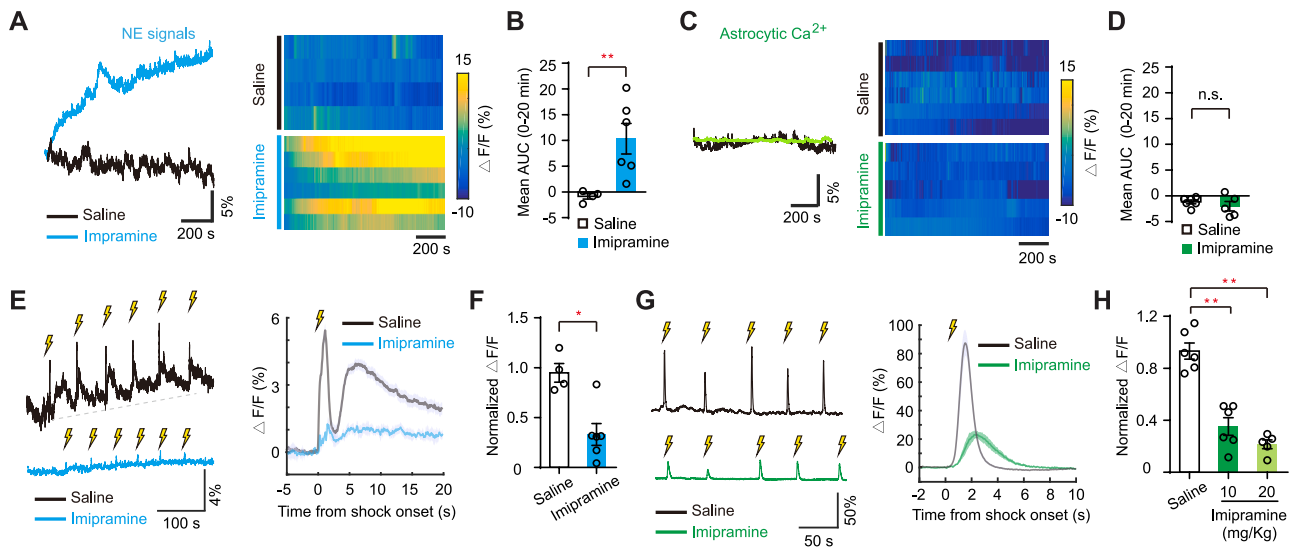


Figure S15. Antidepressant SNRI blocks FS-evoked phasic NE release and astrocytic calcium activities in LHb, related to Figure 7

(A and B) Representative raw traces (A, left), heatmaps (A, right), and bar graph (B) showing responses of LHb NE sensor following an i.p. injection of saline (black, $n = 4$ mice) or imipramine (blue, 20 mg/kg, $n = 6$ mice) in homecage. Scale bars, 5% $\Delta F/F$, 200 s.

(C and D) Representative raw traces (C, left), plots of averaged $\Delta F/F$ ratio (C, right), and bar graph (D) showing responses of LHb NE sensor following an i.p. injection of saline (black, $n = 6$ mice) or imipramine (green, 20 mg/kg, $n = 5$ mice) in homecage. Scale bars, 5% $\Delta F/F$, 200 s.

(E and F) Representative raw traces (E, left), plots of averaged $\Delta F/F$ ratio (E, right), and bar graph (F) showing responses of LHb NE sensor to FS stress following an i.p. injection of saline (black, $n = 4$ mice) or imipramine (blue, 20 mg/kg, $n = 5$ mice). Scale bars, 4% $\Delta F/F$, 100 s.

(G and H) Representative raw traces (G, left) and plots of averaged $\Delta F/F$ ratio (G, right) and bar graph (H) showing responses of LHb astrocytic calcium to FS stress following an i.p. injection of saline (black, $n = 6$, 5 mice for 10 and 20 mg/kg imipramine groups). Scale bars, 50% $\Delta F/F$, 50 s.

* $p < 0.05$; ** $p < 0.01$; *** $p < 0.001$; **** $p < 0.0001$; n.s., not significant. Data are represented as mean \pm SEM.